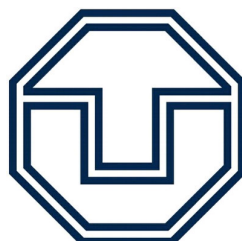Institut für Angewandte Photophysik
Fachrichtung Physik
Fakultät Mathematik und Naturwissenschaften
Technische Universität Dresden

Alternative Electrodes

for Organic Optoelectronic Devices

Dissertation

zur Erlangung des akademischen Grades

Doctor of Philosophy

(Ph. D.)

vorgelegt von

Yong Hyun Kim

geboren am 13.01.1982 in Seoul, Korea

Dresden 2013

Eingereicht am 30.01.2013

1. Gutachter: Prof. Dr. Karl Leo

2. Gutachter: Prof. Dr. Elizabeth von Hauff

Verteidigt am 02.05.2013

Contents

Abstract

This work demonstrates an approach to develop low-cost, semi-transparent, long-term stable, and efficient organic photovoltaic (OPV) cells and organic light-emitting diodes (OLEDs) using various alternative electrodes such as conductive polymers, doped ZnO, and carbon nanotubes. Such electrodes are regarded as good candidates to replace the conventional indium tin oxide (ITO) electrode, which is expensive, brittle, and limiting the manufacturing of low-cost, flexible organic devices.

First, we report long-term stable, efficient ITO-free OPV cells and transparent OLEDs based on poly(3,4-ethylene-dioxythiophene):poly(styrenesulfonate) (PEDOT:PSS) electrodes by using a solvent post-treatment or a structure optimization. In addition, a high performance internal light out-coupling system for white OLEDs based on PEDOT:PSS-coated metal oxide nanostructures is developed. Next, we demonstrate highly efficient ITO-free OPV cells and OLEDs with optimized ZnO electrodes doped with alternative non-metallic elements. The organic devices based on the optimized ZnO electrodes show significantly improved efficiencies compared to devices with standard ITO. Finally, we report semi-transparent OPV cells with free-standing carbon nanotube sheets as transparent top electrodes. The resulting OPV cells exhibit very low leakage currents with good long-term stability. In addition, the combination of various kinds of bottom and top electrodes for semi-transparent and ITO-free OPV cells is investigated.

These results demonstrate that alternative electrodes-based OPV cells and OLEDs have a promising future for practical applications in efficient, low-cost, flexible and semi-transparent device manufacturing.

Kurzfassung

Die vorliegende Arbeit demonstriert einen Ansatz zur Verwirklichung von kostengünstigen, semi-transparenten, langzeitstabilen und effizienten Organischen Photovoltaik Zellen (OPV) und Organischen Leuchtdioden (OLEDs) durch die Nutzung innovativer Elektrodensysteme. Dazu werden leitfähige Polymere, dotiertes ZnO und Kohlenstoff-Nanoröhrchen eingesetzt. Diese alternativen Elektrodensysteme sind vielversprechende Kandidaten, um das konventionell genutzte Indium-Zinn-Oxid (ITO), welches aufgrund seines hohen Preises und spröden Materialverhaltens einen stark begrenz Faktor bei der Herstellung von kostengünstigen, flexiblen, organischen Bauelementen darstellt, zu ersetzten.

Zunächst werden langzeitstabile, effiziente, ITO-freie Solarzellen und transparente OLEDs auf der Basis von Poly(3,4-ethylene-dioxythiophene):Poly(styrenesulfonate) (PEDOT:PSS) Elektroden beschrieben, welche mit Hilfe einer Lösungsmittel-Nachprozessierung und einer Optimierung der Bauelementstruktur hergestellt wurden. Zusätzlich wurde ein leistungsfähiges, internes Lichtauskopplungs-System für weiße OLEDs, basierend auf PEDOT:PSS-beschichteten Metalloxid-Nanostrukturen, entwickelt. Weiterhin werden hoch effiziente, ITO-freie OPV Zellen und OLEDs vorgestellt, bei denen mit verschiedenen nicht-metallischen Elementen dotierte ZnO Elektroden zur Anwendung kamen. Die optimierten ZnO Elektroden bieten im Vergleich zu unserem Laborstandard ITO eine signifikant verbesserte Effizienz. Abschließend werden semi-transparente OPV Zellen mit freistehenden Kohlenstoff-Nanoröhrchen als transparente Top-Elektrode vorgestellt. Die daraus resultierenden Zellen zeigen sehr niedrige Leckströme und eine zufriedenstellende Stabilität. In diesem Zusammenhang wurde auch verschiedene Kombinationen von Elektrodenmaterialen als Top- und Bottom-Elektrode für semi-transparente, ITO-freie OPV Zellen untersucht.

Zusammengefasst bestätigen die Resultate, dass OPV und OLEDs basierend auf alternativen Elektroden vielversprechende Eigenschaften für die praktische Anwendung in der Herstellung von effizienten, kostengünstigen, flexiblen und semi-transparenten Bauelement besitzen.

Publications

Journal articles (first author)

1. **Y. H. Kim**, J. S. Kim, W. M. Kim, T. -Y. Seong, J. Lee, L. Müller-Meskamp, and K. Leo, "Realizing the potential of ZnO with alternative non-metallic co-dopants as electrode material for small molecule optoelectronic devices" (in press, ***Advanced Functional Materials***).

2. **Y. H. Kim**, J. Lee, S. Hofmann, M. C. Gather, L. Müller-Meskamp, and K. Leo, "Achieving high efficiency and improved stability in ITO-free transparent organic light-emitting diodes with conductive polymer electrodes" (in press, ***Advanced Functional Materials***)

3. **Y. H. Kim**, C. Sachse, A. A. Zakhidov, J. Meiss, A. A. Zakhidov, L. Müller-Meskamp, and K. Leo, "Combined alternative electrodes for semi-transparent and ITO-free small molecule organic solar cells", ***Organic Electronics***, 13 (2012) 2422.

4. **Y. H. Kim**, L. Müller-Meskamp, A. A. Zakhidov, C. Sachse, J. Meiss, J. Bikova, A. Cook, A. A. Zakhidov, and K. Leo, "Semi-transparent small molecule organic solar cells with laminated free-standing carbon nanotube top electrodes", ***Solar Energy Materials & Solar Cells***, 96 (2012) 244.

5. **Y. H. Kim**, J. S. Kim, J. Jeong, J. -K. Park, Y. -J. Baik, K. S. Lee, B. Cheong, D. Kim, T. -Y. Seong, and W. M. Kim, "Properties of ZnO Thin Films Co-Doped with Hydrogen and Fluorine", ***Journal of Nanoscience and Nanotechnology***, 12 (2012) 3665.

6. **Y. H. Kim**, C. Sachse, M. L. Machala, C. May, L. Müller-Meskamp, and K. Leo, "Highly Conductive PEDOT:PSS Electrode with Optimized Solvent and Thermal Post-Treatment for ITO-Free Organic Solar Cells", ***Advanced Functional Materials***, 21 (2011) 1076. **(Selected as an inside cover picture article.)**

7. **Y. H. Kim**, C. Sachse, M. Hermenau, K. Fehse, M. Riede, L. Müller-Meskamp, and K. Leo, "Improved Efficiency and Lifetime in Small Molecule Organic Solar Cells with Optimized Conductive Polymer Electrodes", ***Applied Physics Letters***, 99 (2011) 113305.

8. **Y. H. Kim**, S. Zh. Karazhanov, and W. M. Kim, "Influence of hydrogen on electrical and optical properties of ZnO films", ***Physica Status Solidi B***, 248 (2011) 1702.

9. **Y. H. Kim**, J. Jeong, K. S. Lee, B. Cheong, T. -Y. Seong, and W. M. Kim, "Effect of Composition and Deposition Temperature on the Characteristics of Ga doped ZnO Thin Films", ***Applied Surface Science,*** *257* (2010) 109.

10. **Y. H. Kim**, J. Jeong, K. S. Lee, J. K. Park, Y. J. Baik, T. -Y. Seong, and W. M. Kim, "Characteristics of ZnO:Al thin films co-doped with Hydrogen and Fluorine", ***Applied Surface Science,*** *256* (2010) 5102.

11. **Y. H. Kim**, K. S. Lee, T. S. Lee, B. Cheong, T. -Y. Seong, and W. M. Kim, "Electrical, Structural and Etching Characteristics of ZnO:Al films Prepared by RF Magnetron Sputtering", *Current Applied Physics*, *10* (2010) S278.

12. **Y. H. Kim**, K. S. Lee, T. S. Lee, B. Cheong, T. -Y. Seong, and W. M. Kim, "Effects of Substrate Temperature and Zn addition on the Properties of Al-doped ZnO films Prepared by Magnetron Sputtering", *Applied Surface Science*, 255 (2009) 7251.

Journal articles (co-author)

1. C. Sachse, L. Müller-Meskamp, L. Bormann, **Y. H. Kim**, F. Lehnert, A. Philipp, B. Beyer, and K. Leo, "Transparent, dip-coated silver nanowire electrodes for small molecule organic solar cells", *Organic Electronics*, 14 (2013) 143.

2. J. Lee, S. Hofmann, M. Furno, **Y. H. Kim**, J.-I. Lee, H. Y. Chu, B. Lüssem, and K. Leo, "Combined effects of microcavity and dielectric capping layer on bidirectional organic light-emitting diodes", *Optics Letters*, 37 (2012) 2007.

3. L. Müller-Meskamp, **Y. H. Kim**, T. Roch, S. Hofmann, R. Scholz, S. Eckardt, K. Leo, and A. F. Lasagni, "Efficiency Enhancement of Organic Solar Cells by Fabricating Periodic Surface Textures using Direct Laser Interference Patterning", *Advanced Materials*, 24 (2012) 906.

4. J. Lee, S. Hofmann, M. Thomschke, M. Furno, **Y. H. Kim**, B. Lüssem, and K. Leo, "Highly efficient bi-directional organic light-emitting diodes by strong micro-cavity effects", *Applied Physics Letters*, 99 (2011) 073303.

5. J. Lee, S. Hofmann, M. Thomschke, M. Furno, **Y. H. Kim**, B. Lüssem, and K. Leo, "Increased and balanced light emission of transparent organic light-emitting diodes by enhanced microcavity effects", *Optics Letters*, 36 (2011) 2931.

6. B. Yoo, K.-J. Kim, **Y. H. Kim**, K. Kim, M. J. Ko, W. M. Kim, and N. -G. Park, "Titanium Nitride Thin Film as a Novel Charge Collector in TCO-Less Dye-Sensitized Solar Cell", *Journal of Materials Chemistry*, 21 (2011) 3077.

7. J. Lee, S. Hofmann, M. Furno, M. Thomschke, **Y. H. Kim**, B. Lüssem, and K. Leo, "Systematic investigation of transparent organic light-emitting diodes depending on top metal electrode thickness", *Organic Electronics*, 12 (2011) 1383.

8. J. Lee, S. Hofmann, M. Furno, M. Thomschke, **Y. H. Kim**, B. Lüssem, and K. Leo, "Influence of organic capping layers on the performance of transparent organic light-emitting diodes", *Optics Letters*, 36 (2011) 1443.

9. W. M. Kim, **Y. H. Kim**, J. S. Kim, J. Jeong, Y. -J. Baik, J. -K. Park, K. S. Lee, and T. -Y. Seong, "Hydrogen in polycrystalline ZnO thin films ", *Journal of Physics D: Applied Physics*, 43 (2010) 365406.

10. B. Yoo, K.-J. Kim, D. -K. Lee, K. Kim, M. J. Ko, **Y. H. Kim**, W. M. Kim, and N. -G. Park, "Method to Protect Charge Recombination in the Back-Contact Dye-Sensitized Solar Cell", *Optics Express*, 18 (2010) A395.

11. B. Yoo, K. Kim, D. -K. Kim, M. J. Ko, H. Lee, **Y. H. Kim**, W. M. Kim, and N. -G. Park, "Enhanced Charge Collection Efficiency by Thin-TiO_2-film Deposition on FTO-coated ITO Conductive Oxide in Dye-Sensitized Solar Cells", *Journal of Materials Chemistry*, 20 (2010) 4392.

12. D. Y. Ku, **Y. H. Kim**, K. S. Lee, T. S. Lee, B. Cheong, T. -Y. Seong, and W. M. Kim, "Effect of Fluorine Doping on the Properties of ZnO Films Deposited by Radio Frequency Magnetron Sputtering", *Journal of Electroceramics*, 23 (2009) 415.

13. J. -O. Song, K. -K. Kim, H. Kim, **Y. -H. Kim**, H. -G. Kim, H. Na, and T. -Y. Seong, "Formation of Low-resistance and Transparent ITO Ohmic Contact for High-brightness GaN-based LEDs using a Sn-Ag interlayer", *Materials Science in Semiconductor Processing*, 10 (2007) 211.

Journal articles (submitted or in preparation)

1. **Y. H. Kim**, J. Lee, W. M. Kim, S. Hofmann, H. -W. Chang, M. C. Gather, L. Müller-Meskamp, and K. Leo, "We want our photons back: simple nanostructures for white OLED outcoupling" (in preparation)

2. **Y. H. Kim**, S, Schubert, R. Timmreck, L. Müller-Meskamp, and K. Leo, "Collecting the electrons on n-doped fullerene C60 transparent electrodes for low-cost small molecule organic solar cells" (in preparation)

Patents

1. W. M. Kim, B. Cheong, J. Jeong, K. S. Lee, T. S. Lee, **Y. H. Kim**, and J. M. Sohn, "Solar cell and Method for Surface Texturing of Solar Cell", *Korean patent*, 1077547.
2. M. J. Ko, W. M. Kim, K. Kim, N. -G. Park, B. Yoo, and **Y. H. Kim**, "Photo Electrode Comprising Conductive Non-metal Film, and Dye-sensitized Photovoltaic Cell Comprising the Same", *Korean patent*, 10-1061970.
3. M. J. Ko, W. M. Kim, K. Kim, N. -G. Park, B. Yoo, and **Y. H. Kim**, "Photo Electrode Comprising Conductive Non-metal Film, and Dye-sensitized Photovoltaic Cell Comprising the Same", *US patent*, US 2010/0294350 A1.
4. T. -Y. Seong, J. -H. Yoon, H. -G. Hong, J. -W. Jeon, **Y. H. Kim**, and J. S. Kim, "Nitrides Light Emitting Device and Method for Manufacturing the Same", *Korean patent*, 10-2007-0056871, 06/11/2007.
5. **Y. H. Kim**, J. Lee, S. Hofmann, L. Müller-Meskamp, and K. Leo, "Organisches lichtemittierendes Bauelement und Verfahren zum Herstellen", *German patent*, DE 10 2012 112 999.1

Chapter 1. Introduction

Due to the limited supply of fossil fuels and increasing environmental problems associated with the use of fossil fuels, the research on renewable energy has attracted a great deal of attention in last several decades. Photovoltaics are currently attracting much interest as a promising, clean-energy technology. In particular, organic photovoltaic (OPV) cells have been extensively investigated for ages due to their great potentials such as potentially low cost, low material consumption, flexibility, and suitability for roll-to-roll mass production. The performance of OPV cells has recently been greatly improved, opening the path towards an alternative renewable energy source. To realize the main advantages of OPV cells, low cost and flexible devices, the development of electrodes is of great importance. The high cost, brittleness, and high temperature processing of indium tin oxide (ITO), commonly used in photovoltaic applications, drive a search for alternative electrode technologies. To respond to this need, conductive polymers, doped ZnO, silver nanowires, thin metal layers, carbon nanotubes, and graphene have been investigated as alternatives to ITO for OPV cells.

The same holds true for organic light-emitting diodes (OLEDs). As an alternative efficient lighting source and display, OLEDs have attracted a great deal of attention. OLEDs are actively investigated and already employed for flat panel displays, flexible displays, and solid state lighting because of their many benefits such as low-cost, being thin, light weight, flexibility, wide viewing angle, and low power consumption. However, the high cost and the brittleness of ITO limit the advantages of OLEDs as well as OPV cells, and raise demand for an alternative to ITO.

Among numerous advantages of OPV cells and OLEDs such as low-cost and flexibility, an unusual and promising property is the possible semi-transparency of organic optoelectronic devices. Semi-transparent thin film OPV cells allow the installation of solar cells on windows or other architectural building elements, facilitating an efficient energy management of a building or a car by providing artistically colored and tinted light, shadow, and at the same time electricity. Semi-transparent OLEDs also have many interesting features. Semi-

6

transparent OLEDs screen can be integrated into the roof, PC monitor, or window. If one chooses a display content, it turns less transparent. When it is deactivated, it looks like a conventional glass plate. Moreover, double side lighting is possible by bi-directional OLEDs.

The fabrication of novel efficient transparent conductive electrodes for both top and bottom contact is of great importance for ITO-free or semi-transparent organic optoelectronic devices. Especially for sensitive evaporated small molecule OPV cells and OLEDs, the deposition process of the top electrode needs to be very gentle without damaging underlying organic layers, which can be easily shorted due to <100 nm typical thickness, giving rise to many practical difficulties. So far, metal oxides, conducting polymers, silver nanowires, and thin metal layers have been employed as a top electrode for OPV cells and OLEDs. However, avoiding damage to underlying organic layers during the deposition of inorganic materials as well as complex, expensive, slow, and small scale deposition processes of top electrodes are technological issues, which are still challenging.

For realizing low-cost, flexible, efficient, and semi-transparent OPV cells and OLEDs, the development of electrodes is very important. Thus, this thesis focuses on the development of alternative electrodes such as conductive polymers, doped ZnO films, and carbon nanotubes for efficient OPV cells and OLEDs. The thesis is organized as follows: Chapter 2 demonstrates an overview of organic semiconductors and basics of OPV cells and OLEDs. Chapter 3 presents an overview of various transparent electrodes and their applications in OPV cells and OLEDs. Chapter 4 describes the experimental details. In chapter 5, the fabrication of highly conductive polymer electrodes is demonstrated. The applications of the optimized conductive polymer to ITO-free OPV cells are described with the improved photovoltaic performances and lifetime. Results of efficient semi-transparent ITO-free OLEDs based on the conductive polymer are presented. Furthermore, the conductive polymer is combined with a light scattering layer to improve a light extraction of ITO-free OLEDs. Chapter 6 demonstrates optimized ZnO electrodes with non-metallic dopants and their applications in ITO-free OPV cells and OLEDs. Chapter 7 reports semi-transparent OPV cells with laminated carbon nanotubes top electrodes. The combination of various bottom and top electrodes for ITO-free or semi-transparent OPV cells is described.

Chapter 2. Basics of organic semiconductors

2.1. Organic semiconductors

2.1.1. Conjugated π systems

Organic semiconductors have been extensively investigated for ages due to their great potential.[1, 2] Their applications for organic electronic devices are regarded as a promising future technology. The principles of organic based-devices are fundamentally different from conventional inorganic devices. In general, the conductivity occurs in conjugated systems, alternating single and double bonds. The conductivity in organic materials originates from extended π electron systems consisting of p_z orbitals overlapping which provides delocalized π systems. The carbon atoms have six electrons with the configuration of $1s^2 2s^2 2p^2$ in which four electrons of $2s$ and $2p$ orbitals are in the valence band. Due to the small energetic difference between $2s$ and $2p$ orbitals, the four electrons in $2s$ and $2p$ orbitals form three hybrid sp^2 orbitals with bonding angles of 120° in the direction of the x-y plane and one remaining p_z orbital stands out of the plane i.e. perpendicular to the plane (**Fig. 2.1**).
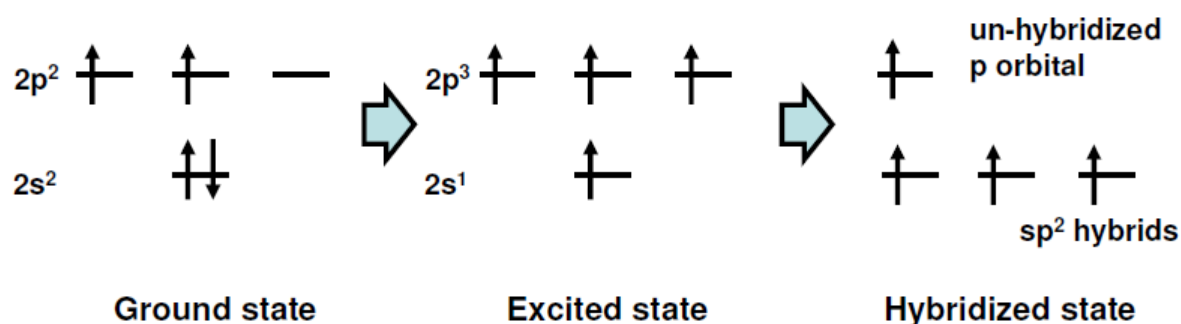

Figure 2.1. *Schematic illustration of the process of hybridized orbital; reproduced from [3].*

The p_z orbitals are overlapped over whole molecular systems, forming extended π systems. Consequently, the electrons can move in the delocalized π systems, providing conductivity in organic semiconductors.

In benzene molecules (**Fig. 2.2**), which have a conjugated system, six carbon atoms are connected by strong carbon-carbon bonds, so-called σ bonds, which form a basic geometry of the molecules.[4] The p_z orbitals are delocalized and perpendicular to the plane. The overlapped p_z orbitals form π bonds. The overlap of p_z orbitals have very close gap between bonding π and anti-bonding π* orbitals. The energy gap of π-π* orbitals are typically in the order of a few electron volts, which are much smaller than that of σ orbitals. The small energetic difference between π-π* orbitals allows easy π-π* transitions by photon absorption.[5] A highest π orbital is so-called a highest occupied molecular orbital (HOMO) and an anti-bonding π* orbital is a lowest unoccupied molecular orbital (LUMO).
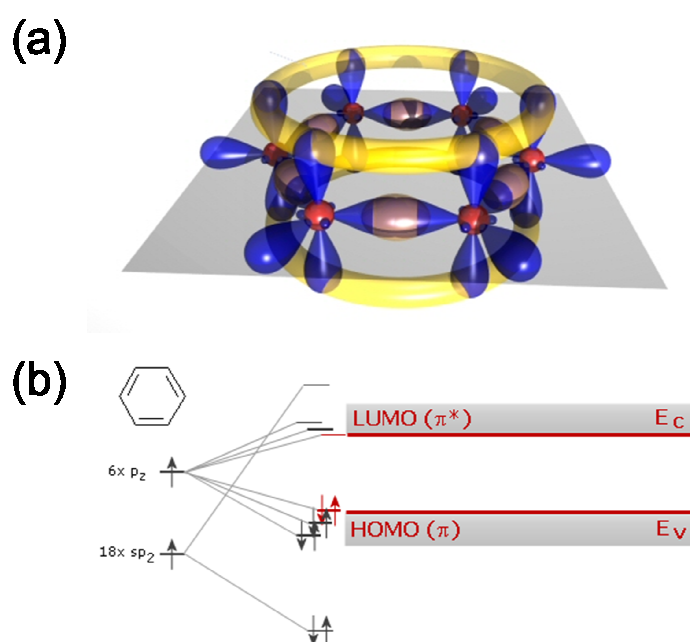
Figure 2.2. (a) Schematic illustration of the orbital structure of the benzene C_6H_6. Red orbital: 1s orbitals, blue orbitals: hybridized sp^2 orbitals. Yellow orbitals: extended π orbitals originated from the p_z orbitals perpendicular to the plane. (b) The formation of a delocalized conjugated π system of benzene; taken from [6].

In general, the size of conjugated system strongly influences the energetic gap between HOMO and LUMO, i.e. the energy gap decreases with increasing the number of aromatic rings (larger π electron systems). Typical values for HOMO-LUMO gaps of aromatic molecules are 1.5 - 3 eV.[7] The energy gap can be tuned by controlling molecular structures, which enables the modulation of light absorption and emission properties of organic materials. These semi-conducting and light absorption properties of organic solids are interesting and beneficial for applications in organic optoelectronic devices.

2.1.2. Excitons

The origin of charge carrier generation in organic semiconductors is fundamentally different from that of inorganic semiconductors. When photons are absorbed into organic semiconductors, strongly bound electron-hole pairs, so-called excitons, are created. The opposite electrical case is also possible. Electrically injected electrons and holes meet in an organic solid and form excitons. The electron-hole pair is strongly bound. The binding force of excitons originates from the Coulomb interaction, which is an attractive force between electrons and holes bound. The Coulomb force is given by

$$F = \frac{1}{4\pi\varepsilon\varepsilon_0}\frac{e^2}{r^2}$$

where ε and ε_0 are the permittivity of the organic medium and vacuum, respectively. e is the elementary charge. r is the distance between the two charges. In general, organic semiconductors have much lower dielectric constants, $\varepsilon = 3.5 \sim 5.5$, than inorganic materials (ex. ε of silicon $\sim$ 12). Valence electrons of atoms in organic semiconductors are more tightly bound to the nucleus than those in inorganic semiconductors.[7]

Weakly bound excitons, so-called Wannier-Mott excitons, in inorganic semiconductors can be found at a very low temperature. Due to a large dielectric constant of inorganic semiconductors, screening of electric field tends to reduce Coulomb interaction between electrons and holes. The binding energy of such excitons is generally much lower than that of a hydrogen atom, typically on the order of 0.01 eV.[7] In such an exciton, the distance between bound electrons and holes is wide enough to dissociate excitons easily into free charge carriers.

In contrast, the excitons in organic semiconductors, so-called Frenkel excitons, are located on a single molecule in organic solids with a low dielectric constant and their radius is typically in the order of < 1 nm, exhibiting a strong binding energy (0.5 $\sim$ 1 eV) and large Coulomb interaction.[4, 7] Their localized carrier wave functions are small enough to fit in the Coulomb well. A pair of polarons, separated onto two neighboring molecules and still bound by Coulomb field, called charge-transfer (CT) excitons, which can be seen in organic semiconductors. A schematic illustration of types of excitons is described in **Fig. 2.3**.
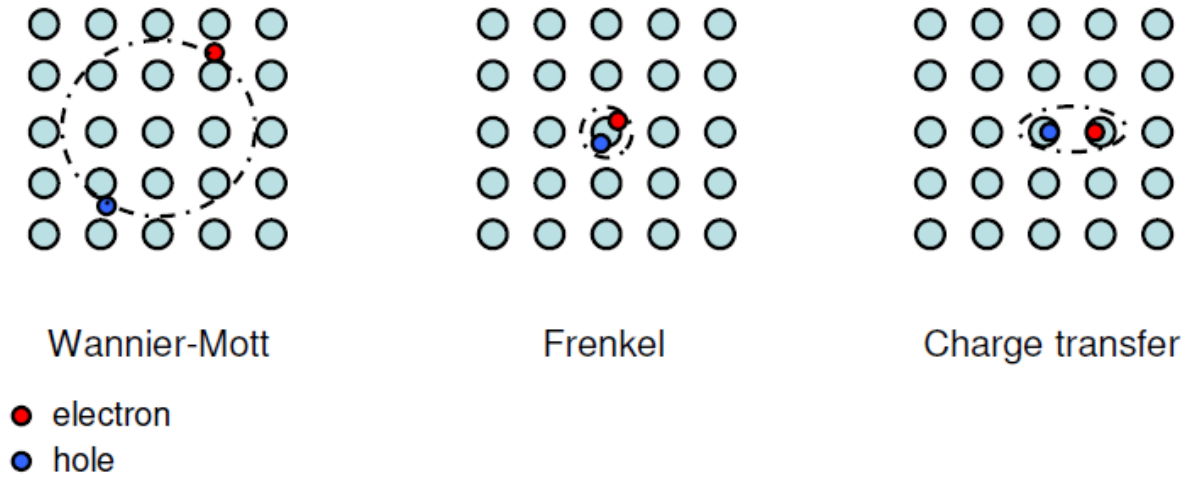
10

Figure 2.3. *The types of excitons. Wannier-Mott excitons, Frenkel exciton, and Charge-transfer excitons; reproduced from [8].*

2.1.3. Exciton diffusion

Excitons travel inside of organic solids via hopping process and have a certain lifetime before recombination. Typically a lifetime of singlet excitons is in the order of only a few nanoseconds. Whereas, triplet excitons exhibit a longer lifetime of up to milliseconds.[4, 7] The driving force of exciton diffusion is a gradient of exciton concentration which can be described by Fick's second law. The exciton diffusion equation is defined by

$$\frac{\partial n}{\partial t} = G(z,t) - \frac{n}{\tau} - Q(n,z,t) + D\frac{\partial^2 n}{\partial z^2}$$

where G is the exciton generation rate. $n\tau^{-1}$ is the exciton decay rate. Q is the exciton quenching rate. D is the diffusion coefficient. τ is the effective exciton lifetime considering radiative and non-radiative decay.

The exciton diffusion length is given by

$$L_D = \sqrt{D\tau}$$

where D is the diffusion coefficient. τ is the lifetime of the exciton. Typically, organic materials have an exciton diffusion length in the range of a few and tens of nanometers.[4, 7] It is known that at high currents, the exciton diffusion length is significantly reduced by triplet-triplet annihilation. In contrast to typical disordered organic materials, the exciton diffusion length of organic single crystals can be more than 100 nm.

2.1.4. Excited state and energy transfer

- Photon absorption

In the ground state, all electrons are paired and have opposite spins according to Pauli's exclusion principle that no two electrons in an atom can have identical quantum numbers. For the excitation in organic molecules, optical or electrical driving energies such as absorption of photons or recombination of charge carriers are needed. By photon absorption in organic solids, an electron, which is originally placed on the singlet ground state (S_0), is vertically excited to a higher singlet state ($S_{1...n}$), according to the Franck-Condon principle.[4, 7] The Franck-Condon principle describes the intensities of vibronic transitions. Because the electronic transitions are very fast processes compared to massive nuclear motions, there are no significant changes in a nuclear configuration during electronic transitions. These electron transitions are "vertical".

- Spin states

Figure 2.4 shows spin configurations of excited molecular systems. According to quantum mechanics, there are four possible spin configurations with one anti-symmetric state and three symmetric states.[4] The former has the total spin quantum number of $S = 0$, which is the so-called singlet state where two spin vectors are completely anti-parallel.

$$\chi_S = \frac{1}{\sqrt{2}}\left[\uparrow(e_1)\downarrow(e_2) - \downarrow(e_1)\uparrow(e_2)\right]$$

The latter has $S = 1$ which are triplet states.

$$\chi_T^1 = \uparrow(e_1)\uparrow(e_2)$$

$$\chi_T^{-1} = \downarrow(e_1)\downarrow(e_2)$$

$$\chi_T^0 = \frac{1}{\sqrt{2}}\left[\uparrow(e_1)\downarrow(e_2) + \downarrow(e_1)\uparrow(e_2)\right]$$

where, the symbols of $\uparrow$ and $\downarrow$ indicate the possible spin states of each electron. The electrons are represented by e_1 and e_2, respectively.

In general, the triplet state has a lower energy than the corresponding singlet state because of lower Coulomb repulsion energy between two triplet electrons, resulting from their symmetric spins which forbid a same position in space (Pauli principle). The optical excitation from the

ground to the triplet state is forbidden because of different spin states, meaning that the total spin states should be conserved during the transition process.[9]
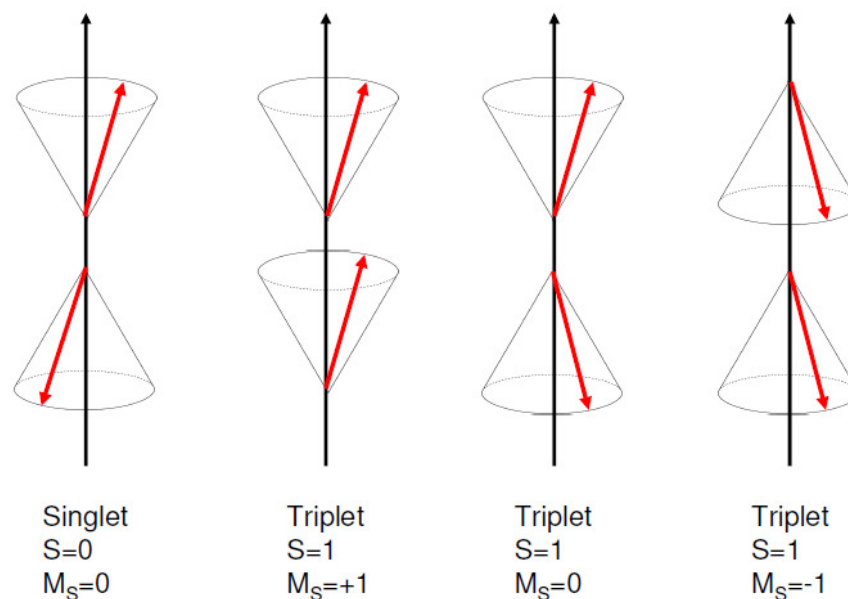

Figure 2.4. Possible spin states, which are singlet and triplet states. S and M_S are the total and magnetic spin quantum numbers, respectively; reproduced from [10].

- Jablonski diagram

The Jablonski diagram in **Fig. 2.5** describes possible energy states as well as various electron and energy transition processes. Vibronic excited states cause rapid non-radiative transitions to the lower excited state, so-called internal conversion, obeying Kasha's rule. This process is very fast, typically in the range of $\sim 10^{-13}$ s, much faster than radiative processes.[11] Accordingly, an emissive recombination only occurs from the decay of lowest excited states, for example S_1 ground to S_0. By photon absorption, electrons can be excited to the vibrational state of S_1 and non-radiatively decay to the excited ground state of S_1. Subsequently it decays to the one of vibrational states of S_0. This process is called fluorescence, radiative decay, resulting in photon emission. The fluorescence is a very rapid radiative process which takes typically in the range of $10^{-9} \sim 10^{-6}$ s.[11] These processes explain the red-shifted absorption spectrum in comparison with emission spectrum in organic solids, so-called Stokes shift.[12]

A phosphorescence emission originates from the excited triplet state T_1. This process has a much longer decay time with a rate constant of $10^{-3} \sim 10^3$ s and is red-shifted compared to fluorescence. By the spin selection rule, the $T_1 \rightarrow S_0$ or $S_0 \rightarrow T_1$ transition is forbidden. However, a strong spin-orbit coupling by an incorporation of heavy metal atoms weakens the

selection rule and reduces time constants for radiative triplet relaxation by several orders of magnitude. The incorporation of heavy metal atoms such as bromine, platinum, or iridium causes metal to ligand charge transfer, which significantly enhances the transitions into triplet states. This causes non-radiative intersystem crossing (ISC), transition from the S_1 state to the T_1 state, involving a spin flip of the excited electron and partially allows $T_1 \rightarrow S_0$ or $S_0 \rightarrow T_1$ transitions.
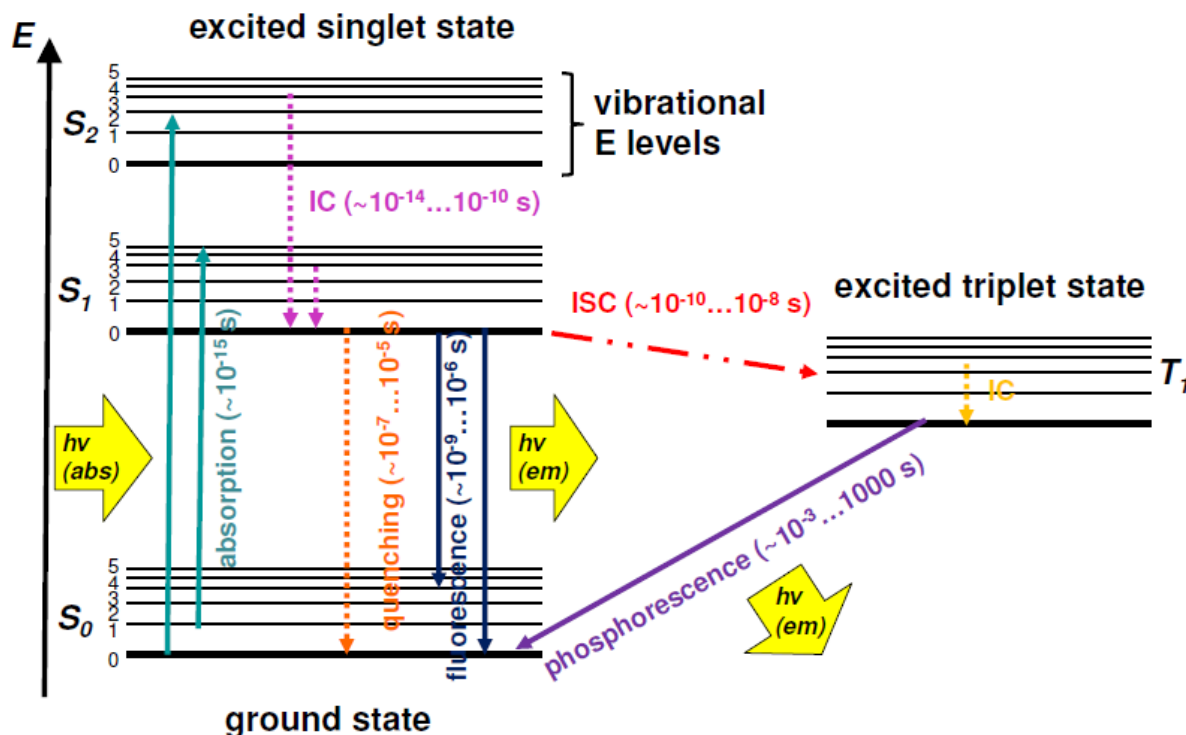
Figure 2.5. *Jablonski diagram showing the processes of the various transitions; reproduced from [13].*

In organic light-emitting diodes (OLEDs), when electrons and holes meet and form excited states, the singlet and tripled states are formed with a ratio of 1:3. It means that the maximum internal quantum efficiency (IQE) of a fluorescence emitter is limited to 25%. However, by using phosphorescent, achieving IQE of 100 % is ideally possible. A spin-orbit coupling induced by heavy metal elements makes the intersystem crossing very efficient, being able to harvest generated singlet excitons. This enables IQE close to 100% by harvesting both singlet and triplet excitons.[14, 15]

- Förster transfer

The Förster transfer model demonstrates that a ground state in an acceptor material can be excited by the energy released from an excited state in a donor material, simultaneously. This process is based on the resonance driven by Coulomb interaction between two adjacent organic donor and acceptor materials. Typically, this transfer process takes place when the separating distance of donor and acceptor is smaller than 10 nm.[16] By absorption of a photon, an electron in donor is excited and then relaxes to the S_1 according to Kasha's rule. If the donor and acceptor are close enough, the released energy, when the electron returns to the ground state S_0, simultaneously excites an electron in acceptor. The basic transfers are as follows.

$D_S^* + A_S \rightarrow D_S + A_S^*$

$D_S^* + A_T \rightarrow D_S + A_T^*$
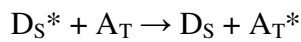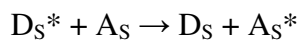
When a phosphorescent donor is introduced, the following transfers are possible due to spin-orbit coupling.
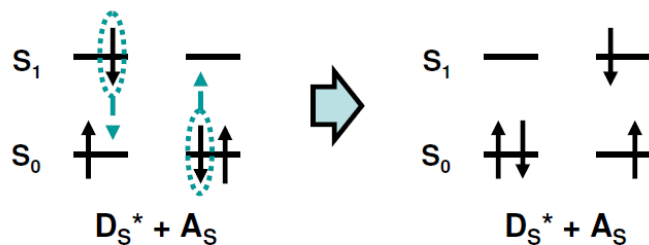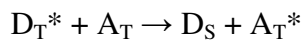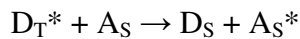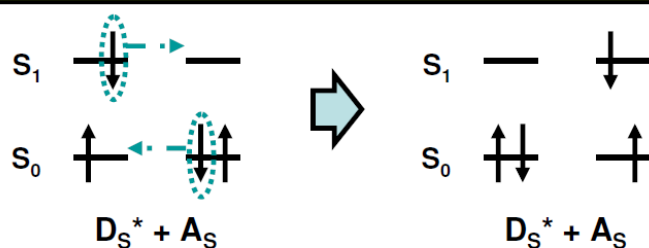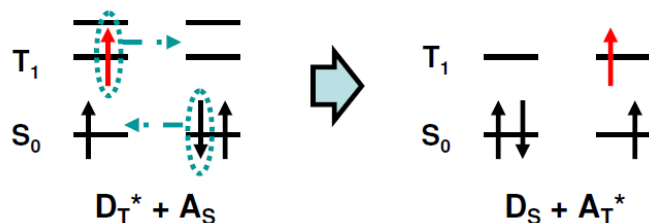
$D_T^* + A_S \rightarrow D_S + A_S^*$

$D_T^* + A_T \rightarrow D_S + A_T^*$

- Dexter transfer

Dexter energy transfer is a process where the donor and the acceptor exchange their electrons. Therefore, besides the overlap of emission and absorption spectra of donor and acceptor, the overlap of wave functions is required for the energy transfer. The exchange process typically takes place within around 1 nm. So it is called a short-range energy transfer.[16, 18] The energy transfer processes can be expressed as

$D_S* + A_S \rightarrow D_S + A_S*$

$D_T* + A_S \rightarrow D_S + A_T*$
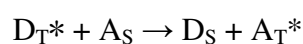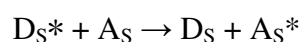
2.1.5. Charge transport

In general, charge transport depends on the ability of the charge carriers to travel from one molecule to another. Charge transport, i.e. current flow, within an electrical field is defined by Ohm's law

$$\vec{J} = \sigma \vec{E}$$

where $\vec{J}$ is the current density, σ the conductivity, and $\vec{E}$ the magnitude of applied electric field. Assuming current flow is carried out by only one carrier, it can be described as

$$\vec{J} = \sigma \vec{E} = -n_e e \vec{v_D}$$

where n_e is the electron density and $\vec{v_D}$ the drift velocity of an electron. And the conductivity of materials can be expressed as

$$\sigma = n_e \mu e$$

where μ is the charge mobility. Therefore, it is shown that drift velocity of electrons depends on mobility of materials. Therefore, the charge mobility, μ, is defined by

$$\vec{v_D} = \mu \vec{E}$$

The mobility in organic solids is much lower than that in inorganic solids and the mobility strongly depends on the numbers of defects, impurities, temperature, and applied electric field. Charge transport in typical organic semiconductors is mainly determined by hopping transport. In contrast, band transport is observed in highly ordered inorganic semiconductors, which show delocalized electrons in periodic potentials, Bloch waves, resulting from strongly

overlapped wave functions of the atoms. However, due to large disorder in most organic semiconductors, the Bloch wave functions are not applied due to weak overlap of wave functions of neighboring atoms, resulting in hopping processes which have significantly lower mobility of carriers.

The mobility in disordered systems is typically several orders of magnitude lower than that in crystalline materials.[19] Typical mobilities in disordered organic semiconductors are in the range of $10^{-5} \sim 1$ cm^2/Vs.[4, 7] In addition, a large HOMO and LUMO energy gap (typically 2 $\sim$ 3 eV) of organic semiconductors leads to a low electrical conductivity (σ of ZnPc: $\sim 10^{-10}$ S/cm).[20] This indicates that the number of thermally activated charge carriers, which can contribute to the conductivity, is very small.

The Gaussian disorder model presented by Bässler describes charge transport in organic semiconductors as Gaussian distribution density of states.[21] Since polaron hopping transport is a thermally activated process, the mobility increases with increasing temperature.

$$\mu(T) = \exp(-\frac{E_a}{k_B T})$$

where E_a is the activation energy, typically in the range of 0.3 $\sim$ 0.5 eV, and k_B is the Boltzmann constant. Thermally activated charge carriers, which overcome activation energy, can contribute to the conductivity. In contrast, charge carriers below the activation energy cannot contribute to the conductivity. The total carrier density in organic solids is a sum of mobile charges activated by thermal energy and immobile charges trapped in localized states mostly in the tails of the Gaussian density of states.

2.2. Organic photovoltaics

2.2.1. Characteristics of conventional solar cells

Solar cells convert photon energy to electricity energy. By illumination of light onto solar cells, electric power is produced. Various types of solar cells have been developed and can be categorized by main light absorbing materials such as crystalline Si, amorphous Si, GaAs, CdTe, CuIn$_x$Ga$_{(1-x)}$Se$_2$ (CIGS), and organic semiconductors, etc, which are semiconductor materials for pn junction which enables photovoltaic energy conversion.

The basic working steps for photovoltaic cells are as below.

→ light absorption: photons, which have a larger energy than the bandgap of the absorber material, are absorbed into the absorber material.

→ generation of photo-carriers: electron and hole pairs are generated.

→ transport of photo-carriers: carriers move on by an electric field or a concentration gradient (drift-diffusion).

→ collection of photo-carriers: arrived carriers at electrodes are collected.

→ generation of electric power

- Spectral response and quantum efficiency

The spectral response is the ratio of the current generated by the solar cell to the power incident on the solar cell.

At long wavelengths, the typical spectral response is strongly limited because semiconductors cannot absorb photons with energies lower than the bandgap. The spectral response also decreases at short wavelengths, because the large energy of photons in the short wavelengths leads to a large input power but a small output current, i.e. the ratio of the output power to photon energy decreases.

Based on the spectral response of solar cells, the external quantum efficiency (EQE) can be derived. The EQE is the ratio of the number of collected charge carriers to the number of photons illuminated on the solar cells. Measurement of EQE allows for quantifying the efficiency of the conversion of light to electrons with respect to the wavelength of the incoming photons. The EQE indicates how good the solar cell converts photons to electrons. The EQE is calculated from the spectral response measured in solar cells as below.

$$EQE = SR\frac{hc}{q\lambda}$$

where SR is the spectral response, q the elementary charge, λ the wavelength, h Planck's constant, and c the speed of light. The EQE of typical organic solar cells is also defined as

$$EQE = \eta_A \eta_{ED} \eta_{CT} \eta_{CC}$$

where η_A is the absorption efficiency, η_{ED} the exciton diffusion efficiency to the donor-acceptor interface, η_{CT} the charge transfer efficiency, and η_{CC} the carrier collection efficiency.[22]

- Carrier concentration

Current characteristics in semiconductors can be described by carrier motion in the band structure. The excitation of charge carriers from the valence band (VB) to the conduction band (CB) creates free charge carriers in both bands, holes in the VB and electrons in the CB. The electron density at given energy, E, is given by

$$n(E) = f(E)g(E)$$

where $f(E)$ is the Fermi-Dirac distribution, which is the occupation probability for a quantum state of certain E, and $g(E)$ the density of states (DOS).

$$g(E) = \frac{dN}{dE}$$

The Fermi-Dirac distribution function is given by

$$f(E) = \frac{1}{1 + \exp\left(\dfrac{E - E_f}{kT}\right)}$$

where E_f is the Fermi energy. At $T = 0$ K, the VB is all occupied but the CB is free of carriers. With increasing temperature, $f(E)$ spreads over E_f, getting toward the CB. Then the total number of electrons in the CB can be derived by integrating $g(E)$ and $f(E)$

$$n = \int_{Ec}^{Etop} f(E)g(E)dE$$

where E_C is the bottom of the CB. The electron density is also expressed as

$$n = N_C f(E_C)$$

where N_C is the effective density of states. $f(E_C)$, the Fermi-Dirac distribution function at the CB, can be approximated as

$$f(E_C) = \frac{1}{1 + \exp\left(\dfrac{E_C - E_f}{kT}\right)} \approx e^{\frac{-(E_C - E_f)}{kT}}$$

Therefore, the number of electrons in the CB is given by

$$n = N_C \exp\left(-\frac{E_C - E_f}{kT}\right)$$

Similarly, a hole concentration is expressed by

$$p = g_V(E)[1 - f(E_V)]$$

The probability of unoccupied state when $E_V \ll E_f$,

$$1-f(E_V)=1-\frac{1}{1+\exp\left(\dfrac{E_V-E_f}{kT}\right)} \approx e^{\frac{(E_f-E_V)}{kT}}$$

Therefore, the hole concentration is

$$p = N_V \exp\left(\frac{E_V - E_f}{kT}\right)$$

In the intrinsic semiconductor without impurities, the number of electrons and holes is same.

$$n = p = n_i$$

n_i is the intrinsic carrier concentration.

$$np = n_i^2 = N_C N_V \exp\left(\frac{E_V - E_C}{kT}\right) = N_C N_V \exp\left(-\frac{E_g}{kT}\right)$$

The number of electrons and holes can be described by

$$n = n_i \exp\left(-\frac{E_f - E_i}{kT}\right), \quad p = n_i \exp\left(-\frac{E_i - E_f}{kT}\right)$$

where E_i is the intrinsic Fermi level which takes place at the middle of E_g.

E band diagram   **Density of states**   **Fermi-Dirac function**   **Carrier density g(E) X f(E)**
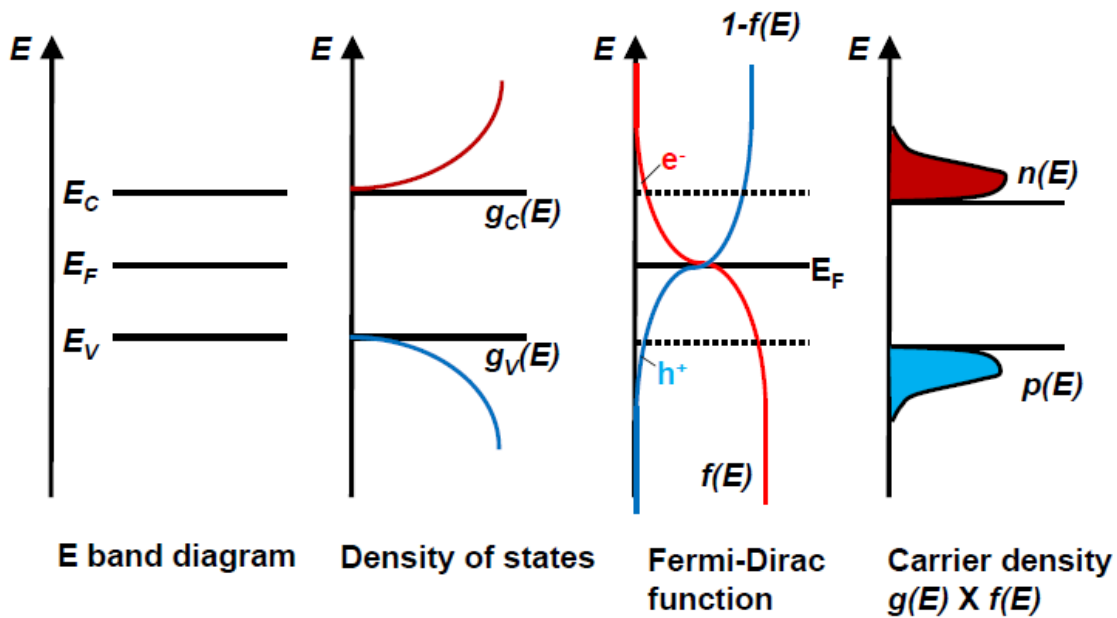
Figure 2.7. *Schematic illustration of energy band diagram, density of states, Fermi-Dirac distribution function, and carrier density profiles; reproduced from [23].*

20

- pn junction diode

The ideal diode equation is the most basic equation for semiconductor pn junctions. The modified basic ideal diode equation can be applied to the operation of solar cells as well. The diode equation, which describes a current through a diode as a function of voltage, is expressed as

$$I = I_0(e^{\frac{qV}{kT}} - 1)$$

where I is the net current flowing through a diode, I_0 the dark saturation current (a diode leakage current density in dark), V the applied voltage, q the electron charge, k the Boltzmann constant, and T the temperature (K). Ideally I_0 should be as low as possible. I_0 is increased when T is high and the semiconductor quality is low, along with increasing trap-assisted recombination.

Solar cells are based on diodes. *IV* curves of solar cells in dark are shifted down into the fourth quadrant as much as photo-generated current. The diode equation is defined as

$$I = I_D - I_L = I_0(e^{\frac{qV}{nkT}} - 1) - I_L$$

where I_D is the current in the dark condition, I_L is the photo-generated current.[24] Non-ideal diodes include an "*n*" term, so-called ideality factor which is a fitting parameter, typically 1 ~ 2, that indicates how good the diode behavior is.

A short circuit current, J_{SC}, is the current at zero voltage. For the ideal diode, J_{SC} and photo-generated current are identical, independent of cell voltage, meaning that J_{SC} is the maximum current which can be extracted from a diode. However, a maximum current in organic photovoltaic (OPV) cells is observed at negative voltage with high internal field due to the disordered system in which the photo-current is strongly field-dependent. V_{OC} is the open circuit voltage at zero current.

$$V_{OC} = \frac{nkT}{q} \ln\left[\frac{I_L}{I_0} + 1\right]$$

At short circuit and open circuit conditions, power generated from the solar cell is zero. A fill factor (FF) is the parameter to determine a maximum power from a solar cell. The FF is determined by the ratio of the maximum power output of the solar cell to the product of its V_{OC} and J_{SC}. This indicates how close the *IV* characteristics under the illumination are to an ideal squareness.

$$FF = \frac{V_{MP}I_{MP}}{V_{OC}J_{SC}}$$

where V_{MP} and I_{MP} are the voltage and current, respectively, at the maximum power point. The FF is greatly affected by parasitic resistive losses such as series and parallel resistances which will be discussed later.

An efficiency of solar cells are determined as the ratio of output energy of the solar cell to the input energy from the sun.

$$\eta = \frac{P_{max}}{P_{in}} = \frac{V_{OC}J_{SC}FF}{P_{in}}$$

where P_{max} is the maximum power and P_{in} is the incident photon power on solar cells. The efficiency needs to be carefully measured since it largely depends on spectrum, intensity of the incident sunlight, and the temperature of devices. A typical condition to measure solar cells is AM1.5G and a temperature of 25°C.

- Current voltage characteristics of solar cells

OPV cells exhibit different features compared to inorganic solar cells. The main differences originate from disordered material systems of organic semiconductors with low mobilities, different light absorption profiles, and the existence of exciton binding energy. Therefore, the conventional Shockley model cannot be directly applied to the case of OPV cells. However, it is known that the traditional model is still useful to understand basic photovoltaic characteristics in OPV cells.

The basic working principle of photovoltaic cells is to convert light energy into electrical energy. The Shockley equation describes the generated current density through the solar cell which is modeled as an equivalent circuit.[25, 26]

$$J(V) = J_0 \left[\exp\left(\frac{e(V - JR_S)}{nK_BT} \right) - 1 \right] + \frac{V - JR_S}{R_p} - J_{ph}$$

where J_0 is the reverse saturation current, e the elementary charge, R_S the series (serial) resistance, n the diode ideality factor, k_B the Boltzmann constant, T the temperature, R_p the parallel (shunt) resistance. This model has widely been used to demonstrate the *IV* behavior of solar cells. It consists of a series and a shunt resistor, a diode, and a photocurrent source as shown in **Fig. 2.8**. The photocurrent source indicates resulting charge carriers converted from absorbed photons. The diode demonstrates the result of recombined electrons and holes at the

pn junction. The series resistor indicates the internal resistance of the cell such as contact resistances and sheet resistances. The shunt resistor describes the local shunts, i.e. leakage currents, between two electrodes in the cell.
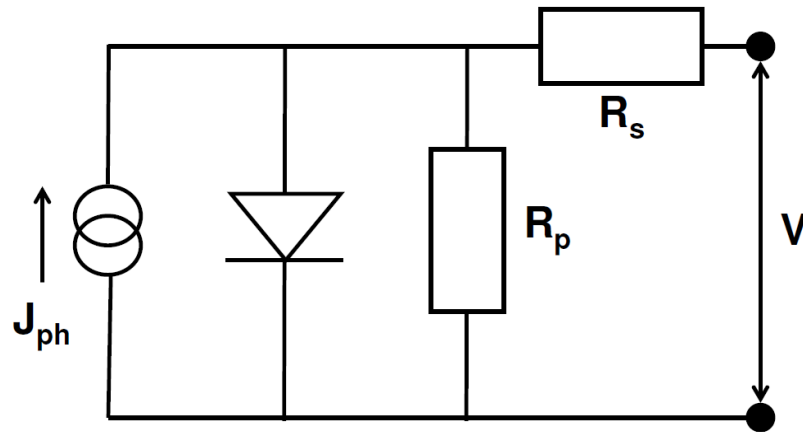

Figure 2.8. *Typical equivalent circuit of typical solar cells.*

In the Shockley equation, the term of the recombination photocurrent source indicates a diode behavior in a dark condition. The J_0 is the saturation current density at reverse bias for an ideal diode, $n = 1$. However, real devices present $n > 1$ due to defect states in the device. The value of n is typically around 2 for common OPV devices. The series and shunt resistance in the diode greatly influence the *IV* behavior of cells. The series resistance $R_S > 0$ Ω mainly results from a voltage drop over charge transport layers and contacts and decreases the slope of the *IV* curve in forward direction. The shunt currents typically originate from defects, pinholes, and spikes of electrodes in the device. The resulting shunt currents flow from one to the other electrode, causing electrical leakages. In general, the high R_S decreases J_{SC} and FF but does not affect V_{OC}. The low parallel resistance R_p leads to shunt currents which decrease the slope at the short circuit condition and reduces V_{OC} and FF but not affecting J_{SC}.

When positive voltages are applied, the current increases exponentially by injection of charge carriers, showing a rectifying behavior in an ideal case. **Figure 2.9** shows the *IV* response of solar cells as a function of voltage. In the low voltage regime (Region I), the *IV* characteristic is strongly dependent on the R_p. The photocurrent is largely field dependent in the case of OPV cells. The maximum photocurrent is not attained at short circuit conditions but increases with negative voltages introducing high internal field. In the intermediate voltage regime (Region II), *IV* characteristics are determined by the diode parameters J_0 and n. In the high voltage regime (Region III), the R_S is the dominant factor to determine the *IV* characteristics.

Due to the low conductivity of organic semiconductors, the space charge builds up at high voltages which results in space-charge-limited currents. The sheet resistance of electrodes and the contact resistance of interfaces strongly increase R_S of devices, which reduces FF and J_{SC} of solar cells.
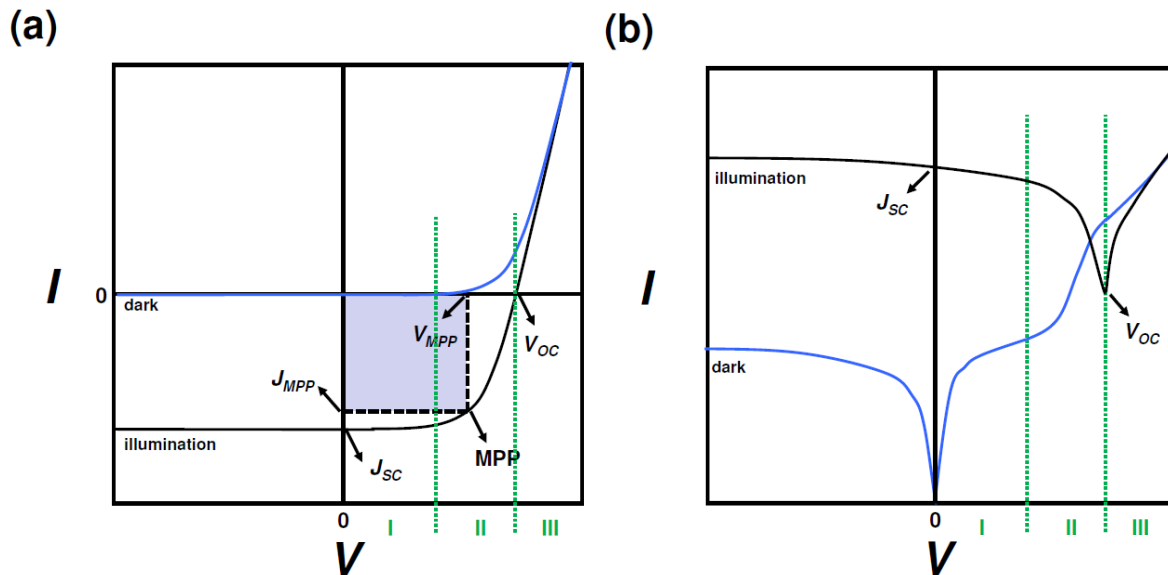
Figure 2.9. *(a) Typical IV curve of solar cells. (blue: dark, black: illumination condition) (b) IV curve presented on a semi-log plot. Region I (low V) is governed by a parallel resistance. Region II (intermediate V) is determined by diode parameters J_0 and n. Region III is governed by a series resistance.*

2.2.2. Basics of organic solar cells

As mentioned above, there are remarkable differences of *IV* characteristics between OPV cells and conventional inorganic solar cells. Organic semiconductors have much different features in comparison with inorganic semiconductors, such as high exciton binding energies, low mobilities, low diffusion coefficients, and high absorption coefficients, exceeding 10^5 cm^{-1}.[27] The absorber layer thickness of OPV cells is much thinner than that of inorganic solar cells. It is in the range of tens or hundreds nanometers which is sufficient to absorb nearly all incoming light. Furthermore, organic semiconductors need an applied field of more than 10^6 V/cm to overcome the exciton binding energy and to separate electron-hole pairs bound by Coulomb interactions.[28] Despite of these differences, the traditional solar cell characterization based on Shockley pn junction model is still useful for OPV characterization.

- Development

The first OPV cells consisted of a single organic material sandwiched between two metal contacts and showed a low device efficiency. The advanced concept of donor and acceptor flat heterojunction was introduced by Tang in 1986, with a much improved efficiency of 0.95 %.[29] The flat donor-acceptor heterojunction concept allows for efficient exciton dissociation and efficient charge carrier transport after dissociation of excitons. A further progress is the development of the bulk heterojunction concept.[30] The mixed structure of donor and acceptor materials leads to a great improvement of efficiency in OPV cells mainly due to efficient exciton dissociation.

- Device architecture

→ Single layer: The first OPV concept is based on a simple structure consisting of an organic material sandwiched between two metal contacts where one of them presents ohmic contact and the other one gives a rectifying contact.[31, 32] The electrodes are typically indium tin oxide (ITO) having a high work function, and low work function metals such as Al, Ca, or Mg. By this concept, an electric field is built up in the organic layer caused by the difference of work function between two electrodes. Upon light absorption in the organic layer, electron-hole pairs, excitons, are created. However, the recombination losses are very high because both photo-generated electrons and holes travel through the same material, limiting photovoltaic performance with a high recombination rate. The device thickness is much higher than the exciton diffusion length so not all excitons are dissociated. Their efficiencies (< 0.1%) and external quantum efficiencies (< 1%) are very low.[33, 34]

→ Flat heterojunction: The bi-layer OPV cells, proposed by Tang, consist of two different organic layers in between bottom and top electrodes.[29] One of organic layers is a donor and the other one is an acceptor material. This structure is also called a planar donor-acceptor heterojunction. Adequate alignment of energy levels between the donor and acceptor materials allows for efficient exciton dissociation at the interface of the donor and the acceptor. This concept improves photon absorption in organic layers when absorption spectrum of donor and acceptor complement each other. The main benefit is efficient charge transport, i.e. holes and electrons travel through donor and acceptor layers, respectively, which reduces a recombination probability of photo-generated charge carriers. The organic layer thickness needs to be thick enough (typically around 100 nm) to absorb incident light. Because the exciton diffusion length in organic materials of typically a few nanometers is

much shorter than the donor and acceptor thickness, generated excitons are strongly recombined before dissociation at the interfaces. Thus, the tradeoff between a thin layer for efficient exciton dissociation and a thick layer for absorbing more light should be carefully considered for designing efficient flat heterojunction OPV cells. For efficient charge separation, it has been reported that the energy offset of LUMO energy level between donor and acceptor should be at least 0.3 ~ 0.4 eV.[35, 36]

→ Bulk heterojunction: The bulk heterojunction (BHJ) concept, reported by the Heeger group, has a mixed structure of donor and acceptor materials, forming interpenetrated networks.[30] The spatially distributed interface, which maximizes the surface area, can dissociate excitons very efficiently. The typical planar donor-acceptor heterojunction requires an active layer thickness of > 100 nm for nearly full light absorption. Since the exciton diffusion length of organic layers is much smaller than the required thickness for light absorption, the BHJ concept is very suitable to achieve high efficiency OPV cells. However, the highly disordered system increases recombination losses of charge carriers, which reduces the FF of OPV cells. Therefore, morphology control is important to balance efficient charge dissociation and recombination losses. For efficient charge transport, phase separation between donor and acceptor materials has to form well-continued percolation pathways. Solvent or thermal treatments of BHJ are widely investigated to reach a favorable morphology with high crystallinity, which improve photovoltaic performance.[36]
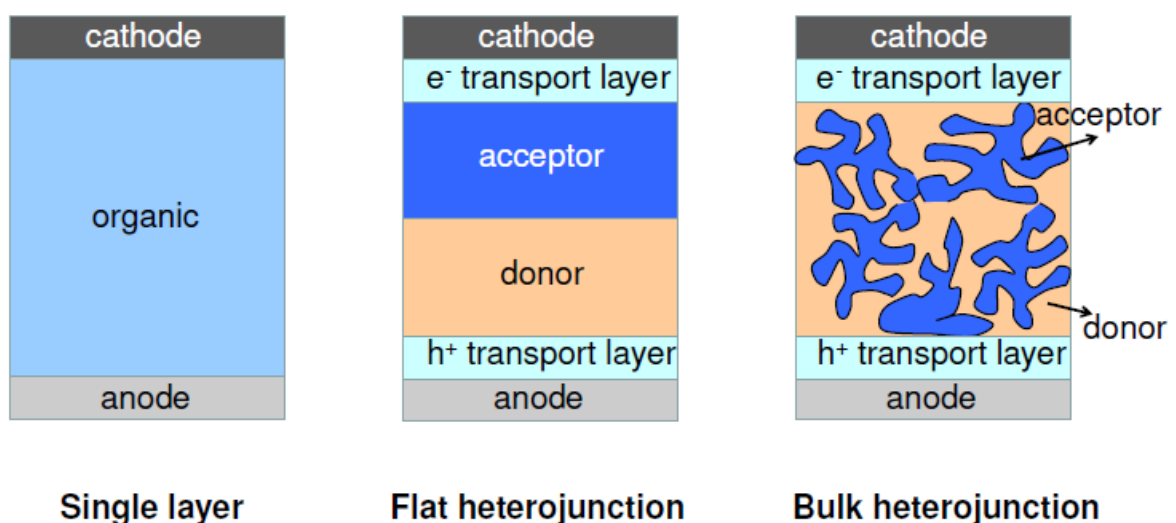

Figure 2.10. *Schematic illustration of the architectures of OPV cells.*

- Working principles of donor-acceptor heterojunction OPV

When illuminating OPV cells, photons are absorbed into absorber layers and excitons are created. Due to the strong exciton binding energy (~0.5 eV) which is much larger than thermal energy, excitons cannot be dissociated within the pristine material itself. Therefore, another driving force is necessary to dissociate excitons. The excitons travel to the donor-acceptor interface by diffusion. At the donor-acceptor interface, the electrons are transferred to the acceptor material, so-called charge transfer process. This charge transfer process is very fast in the range of tens of femtoseconds, which is much faster than photoluminescence or intersystem crossing.[36] For efficient charge transfer, the offset in the electron affinity of donor and acceptor should be larger than the exciton binding energy. Dissociated electrons and holes in the donor and acceptor materials, respectively, are still Coulomb bound, forming charge transfer complexes (polaron pair: Coulomb-bound pair of positive and negative polaron). The polaron pairs, which are not dissociated yet, can recombine geminately before dissociation. Complete dissociation of polaron pairs into free charge carriers can be temperature or field assisted. Excess energy after exciton dissociation (the LUMO energy offsets) provides kinetic energy for overcoming the Coulomb attraction.[35, 36] After the polaron pairs are dissociated, the free charge carriers escaped from Coulomb attraction travel to electrodes via organic materials. The transport process takes place by hopping in the disordered organic medium. For efficient charge transport, high carrier mobility and crystallinity of organic transport materials are desirable to reduce recombination losses between electrons and holes, so-called bimolecular or non-geminate recombination. In the flat heterojunction, the bimolecular recombination is quite low because of well separated carrier paths at the respective donor and acceptor phases. However, in the BHJ concept, electrons and holes can easily recombine non-geminately during charge transport. Finally, charge is collected at the respective electrodes. The electrodes and organic interfaces are important for efficient charge collection. It is desirable to form ohmic contacts, well-aligned energy level, and good film quality without trap states at the interface.

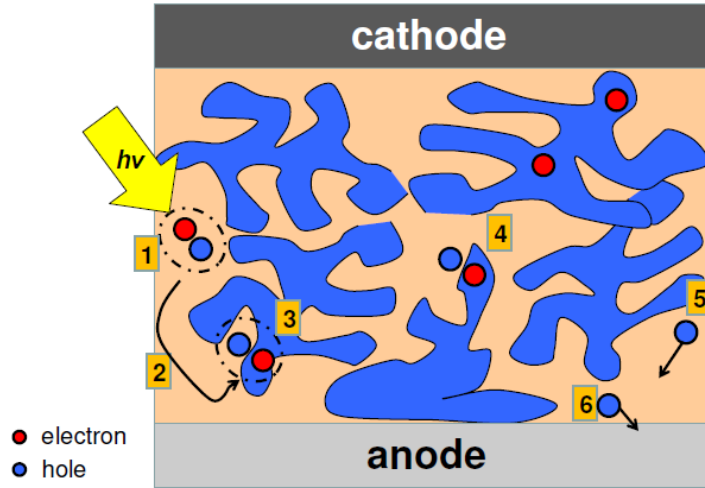**Figure 2.11.** *Illustration of the photon to electron conversion process in OPV cells. (1) photon absorption and exciton generation, (2) exciton diffusion, (3) exciton dissociation, (4) separation of electron and hole pair, (5) charge transport, (6) charge collection at the electrode.*
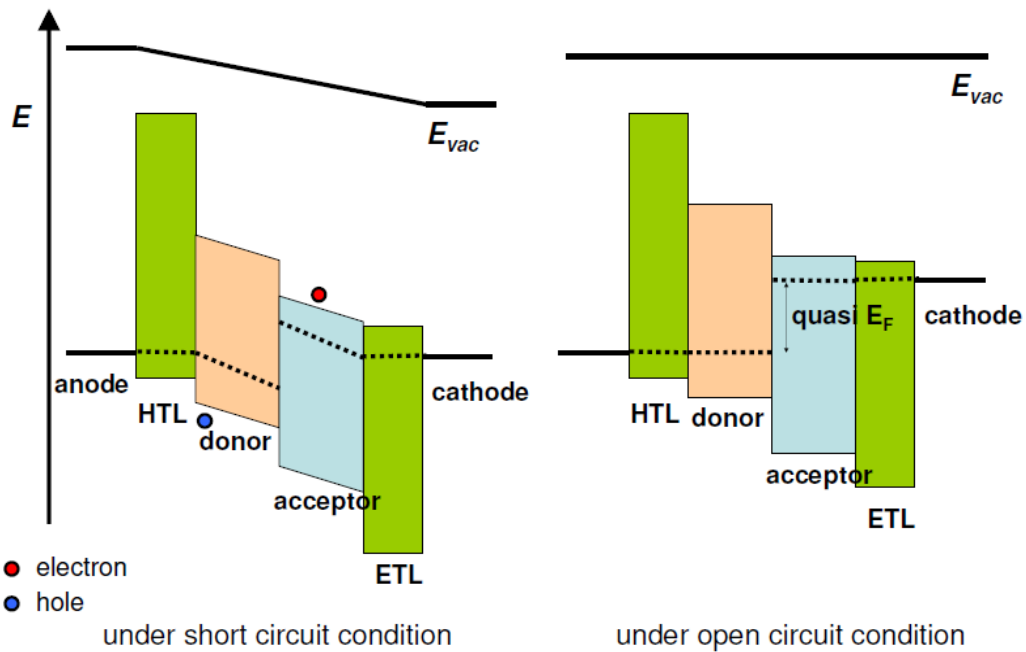

Figure 2.12. *Schematic energy diagram of a simple donor-acceptor heterojunction OPV cells under short circuit and open circuit conditions.*

2.3. Organic light-emitting diodes

2.3.1. Principles of organic light-emitting diodes

In principle, organic light-emitting diodes (OLED) and OPV cells work similar, but in opposite ways. A simple bi-layer structure OLED consists of two thin organic layers sandwiched between two electrodes.[37] One organic layer is specified to transport holes and the other layer is to transport electrons. By applying an electrical field, a gradient of energy levels is generated. Charges are injected from anode and cathode into the organic layers. The electrons and holes meet mostly near the interface of two organic layers, the so-called recombination zone, and form excitons. Excitons can be either in a singlet state or a triplet state. In general, three triplet excitons are formed for each singlet exciton in the electrically excited case. The excitons would relax to the ground state and the relaxation energy is converted to photon. Since the transition from triplet states to ground state is spin forbidden, 75 % of excitons decays non-radiatively, which limits the efficiency of fluorescent devices. However, phosphorescent materials can use both singlet and triplet excitons to generate light. The spin-orbit coupling weakens the selection rule and reduces the lifetime of triplet states, which leads to efficient intersystem crossing (ISC) and radiative $T_1 \rightarrow S_0$ transition.

The simple bi-layer structure is limited to low efficiency due to a large amount of non-radiative recombination. Therefore, most efficient OLEDs have multi-layered stacks having a hole injection layer (HIL), an electron blocking layer (EBL), an emission layer, a hole blocking layer (HBL), and an electron injection layer (EIL) sandwiched in the anode and the cathode.[38, 39] In this structure, the individual organic layers can play a role independently and therefore can be optimized independently as well. For example, the emission layer can be optimized for a desirable electroluminescence (EL) color as well as an efficiency. Also, the transport layers can be engineered for optimum charge balance, charge injection, and energy level matching.

- Quantum efficiency

The external quantum efficiency (EQE) of OLEDs is defined as the ratio of the number of photons emitted from the device to the number of carriers injected into organic layers. It can be expressed as

$$\eta_{EQE} = \eta_{IQE} \cdot \eta_{out} = \eta_{CB}\eta_{spin}\eta_r\eta_{out}$$

where η_{CB} is the charge balance factor, η_{spin} the exciton spin factor, η_r the efficiency of radiative decay of emitter, and η_{out} the light outcoupling factor, respectively. Internal quantum efficiency (IQE) is defined by a combination of the factors of $\eta_{CB}\,\eta_{spin}\,\eta_r$.[14]

By the injection of charge carriers, electrons and holes meet and form excitons. The charge balance factor, η_{CB}, is described as the ratio of injected electron and hole pairs which form excitons. It strongly depends on electrical transport properties of the device. Unbalanced charge transport for electrons and holes due to large differences of mobility or energy barriers leads to the low efficiency of OLEDs. Therefore, lowering injection barriers at contacts by using doped transport layers or efficient charge confinement in the emission zone by using carrier blocking layers are efficient ways for achieving good charge balance. These approaches can improve the charge balance factor to nearly unity, which means that all injected carriers form excitons.

The exciton spin factor, η_{spin}, is defined as the ratio of excitons which can contribute to a radiative recombination. As mentioned above, electrically excited singlets and triplets are formed with a ratio of 1:3. Due to spin-forbidden triplet relaxation to the ground state, fluorescent emitters lose 75% excitons in the triplet state although their quantum yield reaches 100%.[40-43] In contrast, phosphorescent emitters can use triplet excitons without loss due to relaxed spin selection rules by strong spin-orbit coupling, which results from the introduction of heavy metal atoms. In addition, efficient ISC makes the phosphorescent emitter harvest singlet to triplet states.[14, 15] Therefore, exciton spin factors of fluorescent and phosphorescent emitters can reach 0.25 and unity, respectively.

The intrinsic radiative efficiency, η_r, is defined as the ratio of radiative recombination rate k_r to the total recombination rate (radiative and non-radiative processes). It can be expressed as

$$\eta_r = \frac{k_r}{k_r + k_{nr}}$$

where k_r and k_{nr} are the rate of radiative and non-radiative decay of excitons, respectively. The radiative efficiency η_r corresponds to the photoluminescence (PL) quantum yield, η_r = PL = # of emitted photons / # of absorbed photons. The use of phosphorescent emitter is a good example to increase radiative recombination while decreasing non-radiative recombination.

The out-coupling efficiency is defined as the number of photons emitted into air to the number of photons generated in OLEDs. Due to the total internal reflection at the interfaces of layers originating from different refractive indices, a large amount of light cannot be out-coupled, i.e. photons are trapped in devices. Conventional bottom emitting OLEDs have an out-coupling efficiency of only 20 ~ 30 %, indicating that improving out-coupling efficiency is the most important factor to attain high performance OLEDs. In classical ray optics,[44, 45] the out-coupling efficiency of bottom emitting OLEDs can be estimated by

$$\eta_{out} = \frac{1}{2} \frac{n_{air}^2}{n_{glass}^2}$$

Differences of refractive indices and absorptions of layers as well as interference effects are not considered in this model. The resulting out-coupling efficiency is around 20 %. Therefore, the EQE of phosphorescent and fluorescent OLED are limited to 20 and 5 %, respectively, due to the poor out-coupling efficiency of conventional bottom-emitting OLED structures.

Figure 2.13 presents light modes in the OLED. The refractive index mismatch between ITO (n~2.0) and glass (1.5) greatly increases the total internal reflection at the interface, so-called organic wave-guided mode. The trapped photon in the glass substrate is so-called substrate wave-guided mode.[46] Therefore, light generated in the emitter layer is first trapped by the organic mode and followed by the substrate mode. These processes strongly reduce out-coupled light. To improve the out-coupling efficiency, many techniques are extensively investigated. The half-sphere and microlens array approaches successfully reduce the substrate mode, which are performed outside of the glass substrate, not affecting the structural or electrical properties of device.[47, 48] In contrast, reducing the organic mode is more complicated than the substrate mode because of the fact that artificial structures should be prepared between a substrate and soft organic layers, which may causes a significant roughness problem. Scattering layers,[49-51] low index grids,[52] high index glass[53, 54] approaches are widely investigated to decrease light trapped in the organic mode.
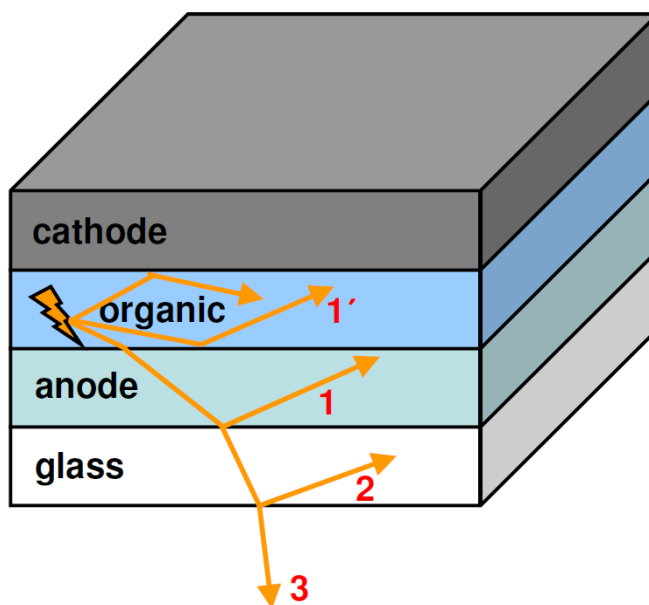
Figure 2.13. *Schematic diagram of guided light in the OLED. (1&1´: trapped light in organic mode, 2: trapped light in substrate mode, 3: out-coupled light)*

- Device structure

The multilayer structure with respective roles of each layer is of necessity to obtain high OLED performance. In general, the multilayer OLED consists of transport layers, an emission layer, blocking layers, and electrodes.

Transport layer: For efficient charge injection and transport, properties of transport layer are of importance. Thus, doping in transport layers is regarded as a very effective method, resulting in many benefits such as lowering injection barrier, increasing carrier mobility, lowering operating voltage, and enhancing charge balance, etc.[38, 55] The doping is carried out by mixing the organic semiconductor with strong acceptor or donor materials. The doping of reactive metals such as Cs and Li is widely used but the diffusion problem within device, caused by small size of dopant atoms, is undesirable. Therefore, organic dopants such as 2,3,5,6-Tetrafluoro-7,7,8,8-tetracyanoquinodimethane (F4-TCNQ) and 2,2´-(perfluoronaphthalene-2,6-diylidene)dimalononitrile (F6-TCNNQ) are regarded as a better choice for stable devices.[6, 38, 55]

Blocking layer: Within the p-i-n device, two thin functional layers are sandwiching the emission layer, which are carrier blocking layers.[38, 39] They confine injected charges within the emission layer, improving the radiative decay efficiency. The LUMO of EBL should be much higher than that of emission layer for preventing current leakage as an energy barrier.

32

At the same time, holes should move freely through similar level of HOMO for EBL and emission layer, which should have a high hole mobility for efficient hole transport.

Emission layer: For high performance of OLEDs, an efficient emission layer is required. It should have an excellent radiative decay efficiency with high exciton spin factor. The phosphorescent emitters can reach IQE of 100% with a high PL yield.[14, 15] In phosphorescent, however, triplet-triplet annihilation is observed at high luminance due to long lifetime of triplets. To overcome this, host-guest systems with the phosphorescent emitter incorporated in a matrix material, is widely used.

2.4. Doping concept in small molecule organic devices

The multilayer structure, referred to as p-i-n structure, for OLEDs as well as OPV cells can greatly improve the device performance compared to simple structure. The p-i-n concept refers to device structure where an intrinsic absorber layer (for OPV cells) or an emission layer (for OLEDs) is sandwiched between the p-doped hole transport layer and the n-doped electron transport layer.[38, 55] Doping in transport layers is a key parameter to realize the efficient p-i-n structures. The matrix layer is doped with strong acceptor or donor materials for p- or n- type molecular doping, respectively.[56, 57] The schematic doping process is presented in **Fig. 2.14**. For example, ZnPc or N,N,N´,N´-Tetrakis (4-methoxy-phenyl)-benzidine (MeO-TPD) doped with F4TCNQ shows the effective p-doping effect.[6, 58] The n-doping process is more challenging than the p-doping because n-dopants have very high HOMO and LUMO level, which makes them unstable against oxygen. For preventing migration of dopant atoms, organic dopants are preferred to reactive metal dopants. The advantages of doping in transport layers are as follows.

→ Efficient charge transport

The conductivity of organic layers can be increased by doping which enhances charge transport of devices. Doping results in increased charge carrier density which raises the conductivity of transport layers by several orders of magnitude. For example, the F4TCNQ doped MeO-TPD reaches the conductivity of 10^{-5} S/cm.[58] Therefore, efficient charge transport achieved by doping can improve charge balance and fill factor of OLED and OPV cells, respectively.
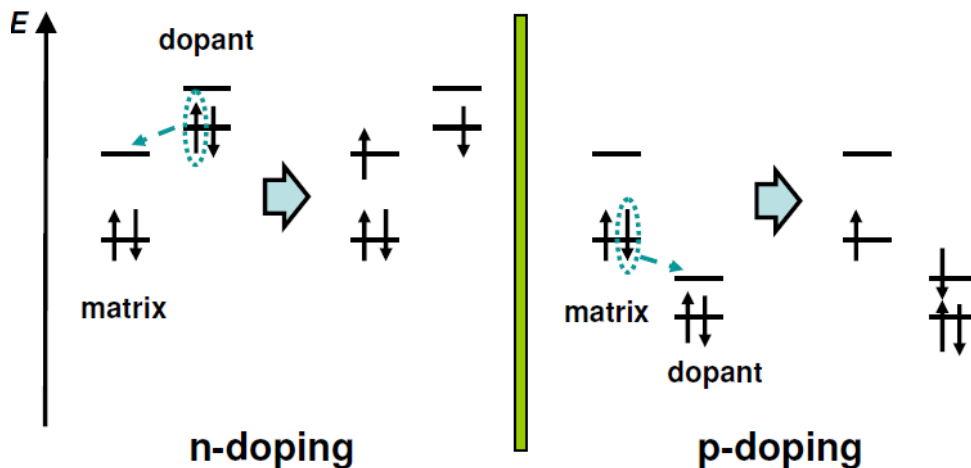
Figure 2.14. *Molecular doping mechanism for n-doping and p-doping. The energetic favored charge transfer from dopant to matrix (n-doping) or matrix to dopant (p-doping) leads to an increase in carrier density in the matrix.*

→ Charge blocking

For OPV cells, an exciton blocking layer such as bathocuproine (BCP) or 4,7-diphenyl-1,10-phenanthroline (BPhen), wide bandgap materials, is deposited between the transport layer and the top electrode. Due to the large offset in energy levels, excitons are reflected at the interface between the acceptor and the exciton blocking layer. The doped transport layer such as n-C_{60} also acts as the exciton blocking layer. Diffused excitons from the absorber layer can be reflected at the interface of the exciton blocking layer, which prevents quenching of excitons. The HOMO of the exciton blocking layer should be very low enough to reflect excitons while LUMO matches to the n-layer and the cathode for efficient electron transport. Since the exciton blocking layer has a wide bandgap, it is highly transparent with negligible absorption loss. The exciton blocking layer typically has a low conductivity than the doped transport layer so the thickness needs to be less than 10 nm for efficient charge tunneling.

→ Charge injection

Molecular doping significantly reduces the energy barrier between the electrode and the transport layer, which can improve charge injection and extraction behavior of OLEDs and OPV cells. The doping causes a shift of the Fermi level toward the HOMO (p-doping) or LUMO (n-doping) of the transport layers.[6, 38, 55] This leads to large band bending and a very thin depletion zone at the interface of the transport layer, which increases the probability of charge tunneling through the interface between the electrode and the transport layer with ohmic contact. In addition, the reduced energy barrier due to the shifted Fermi level of the

transport layer minimizes the effect of work function of electrodes as shown in **Fig. 2.15**. This is a great advantage of the doped transport layers for the application in devices. Furthermore, the operating voltage of OLEDs can be decreased by several volts by doping in the transport layers.[38]
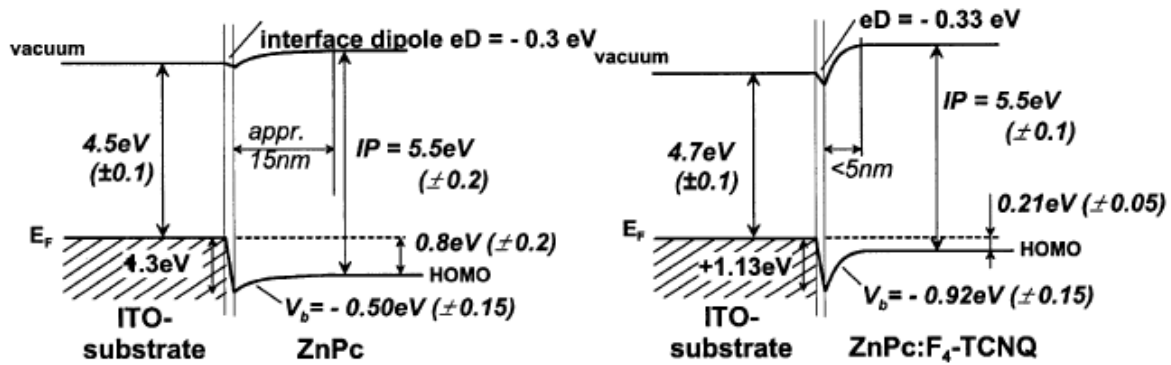

Figure 2.15. Schematic illustration of energy level alignment for the interface of ITO and ZnPc (left: undoped ZnPc, right: doped ZnPc); taken from [6].

→ Out-coupling

In addition to electrical improvements, OLEDs and OPV cells can be optically optimized by tuning the thickness of the doped transport layers. Since the thickness of OLEDs and OPV cells is in the sub-wavelength range, interference and microcavity effects greatly affect the performance of the devices. Therefore, the optimum device structure can be determined by an optical spacer thickness. Since doped transport layers exhibit negligible light absorption losses, the light emission zone can be shifted by controlling the thickness of the doped transport layers, which can be even extended to hundreds of nanometers without any optical loss, to find an optimum geometry showing a maximum emission from constructive interference combination in OLEDs. For OPV cells, the maximum optical field can be placed in the light absorber layer by controlling the optical spacer thickness for maximum light absorption. In chapter 5, optimization of poly(3,4-ethylenedioxythiophene):poly(styrene-sulfonate) (PEDOT:PSS)-based OLEDs with respect to the thickness of the hole transport layer is described in detail. Furthermore, the optimization of the optical field distribution in OPV cells with free-standing carbon nanotube top electrodes is reported in chapter 7.

→ Long-term stability

Interestingly, the long-term stability of devices can be improved by the use of doped transport layers. Fehse et al. reported the improved lifetime of OLEDs with conductive polymer

electrodes by introducing the doped transport layers.[59] The transport layer prevents diffusion of water into the organic layers, resulting in the improved stability. Furthermore, the stability of OLEDs based on conductive polymer electrodes is improved by increasing the transport layer thickness.

→ Prevent damage

The transport layer or the exciton blocking layer directly below the top electrode for OLEDs and OPV cells can prevent damage of the active layer from top electrode deposition.

Chapter 3. Transparent conductive materials

3.1. Transparent conductive oxides

3.1.1. Introduction

Various kinds of transparent conductive oxides (TCO) have been extensively studied for a century and some of TCOs are used in practical use such as flat panel displays, light-emitting diode (LED), and organic and inorganic solar cells as essential electrodes. In general, most of TCO thin films are polycrystalline or amorphous materials and n-type degenerated semiconductors. Although p-type TCO films have also been investigated since 1993, they have difficulties in achieving high performance and processability. The requirements of TCOs for practical use are as follows: a resistivity of the order of 10^{-3} Ωcm and an average transmittance above 80 % in the visible range.[60] There are various deposition methods to fabricate TCOs such as magnetron sputtering, pulsed laser deposition (PLD), metal organic chemical vapor deposition (MOCVD), vacuum arc plasma evaporation, solution deposition, spray pyrolysis, and e-beam evaporation.[61]

Of many TCOs, tin doped indium oxide (ITO) is the most common material due to its high conductivity and high transparency. However, the high cost of ITO due to limited indium supply raises the demand to seek alternative electrodes. As alternatives to ITO, impurity doped zinc oxide (ZnO), fluorine doped tin oxide (FTO), and multi-component oxide films are widely investigated. **Figure 3.1** shows candidates of binary or multi-component TCOs for practical use based on three metal oxides thin films of ZnO, In_2O_3, and SnO_2.[60] Besides these materials, many other TCOs as well as dopants have been studied as shown in **Table 3.1**.[62] However, some TCOs suffer from fabrication or environmental problems. CdO and TiO_2 based TCOs are not suitable for low temperature process because of their high deposition or sintering temperature. In addition, the strong toxicity of Cd leads to environmental pollution. SnO_2-based TCOs are also unsuitable for low temperature processing.[62] Therefore, ZnO-based TCOs are regarded as one of most promising materials for practical use so we mainly focus on ZnO-based TCOs in this study.
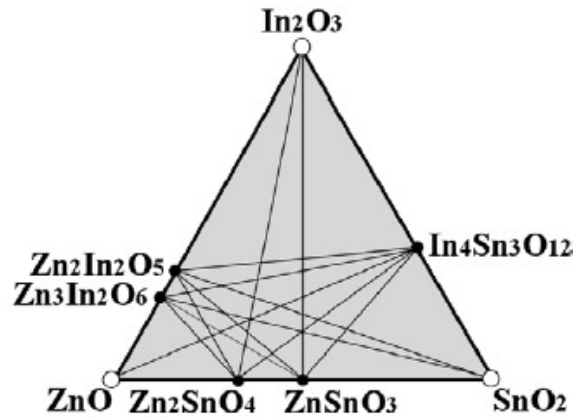
Figure 3.1. *Combination of TCOs for practical use; taken from [60].*

Table 1
Host and associated dopant materials in typical TCO thin films

Binary	Dopant	Resistivity	Toxicity
ZnO	Al, Ga, B, In, Y, Sc,V, Si, Ge, Ti, Zr, Hf, // F	◎	
CdO	In, Sn	◎	××
In_2O_3	Sn, Ge, Mo, Ti, Zr, Hf, Nb, Ta, W, Te // F	◎	×
Ga_2O_3	Sn	Δ	
SnO_2	Sb, As, Nb, Ta // F	○	
TiO_2	Nb, Ta	Δ	
Ternary			
$MgIn_2O_4$		Δ	
$GaInO_3$, $(Ga, In)_2O_3$	Sn, Ge	Δ	
$CdSb_2O_6$	Y	Δ	×
$SrTiO_3$	Nb, La	×	

Ternary	Multi-component	Resistivity	Toxicity
$Zn_2In_2O_5$, $Zn_3In_2O_6$	$ZnO-In_2O_3$ system	○	
$In_4Sn_3O_{12}$	$In_2O_3-SnO_2$ system	○	
$CdIn_2O_4$	$CdO-In_2O_3$ system	○	×
Cd_2SnO_4, $CdSnO_3$	$CdO-SnO_2$ system	○	×
Zn_2SnO_4, $ZnSnO_3$	$ZnO-SnO_2$ system	Δ	
	$ZnO-In_2O_3-SnO_2$ system	○	
	$CdO-In_2O_3-SnO_2$ system	○	×
	$ZnO-CdO-In_2O_3-SnO_2$ system	○	×

: ◎Very good, ○: Good, Δ: Average, ×: Bad, ××: Very bad.

Table 3.1. *Various TCOs and associated dopant materials; taken from [62].*

3.1.2. Properties of ZnO

To replace ITO, ZnO is regarded as an excellent material due to its low cost, wide bandgap, ease of doping, durability under hydrogen atmosphere, low-temperature processability, and non-toxicity. ZnO is generally an n-type degenerated semiconductor with a wide bandgap (Eg~3.2 eV) based on a hexagonal wurtzite structure with a = 3.25 Å and c = 5.12 Å. Increasing the conductivity of ZnO films can be obtained by impurity doping. ZnO films doped with Al or Ga, which are the most common metallic dopants, show a resistivity of the order of 10^{-4} Ωcm.[60, 63] Dopants in ZnO are categorized into two types: native and extrinsic donors. The native donors of Zn interstitials and O vacancies, and extrinsic donors such as Al, Ga, and H significantly increase the conductivity of ZnO films. The intrinsic defect levels, resulting in n-type doping, are typically positioned 0.01 ~ 0.05 eV below the conduction band.[64] Upon extrinsic impurity doping, shallow donor levels close to the conduction band increase. The Fermi level may reach the conduction band by the addition of sufficient dopants. The doping of ZnO supplies plenty of free electrons into the conduction band, which makes ZnO behave like a metal. For photovoltaic applications, conductive ZnO films are particularly employed as transparent electrodes for amorphous Si and $CuIn_xGa_{(1-x)}Se_2$ (CIGS) solar cells.

3.1.3. Conductivity of ZnO

In the 1980s, the resistivities of ZnO reached the order of 10^{-4} Ωcm by impurity doping of Group III elements such as Al, Ga, In, and B.[60, 63] The metallic dopants substitute Zn atom sites whereas anionic dopants are positioned in O atom sites. **Table 3.2** shows various dopants for ZnO thin films, being able to achieve low resistivities with high carrier concentrations by optimal doping concentrations.[60] Among many kinds of dopants, Al and Ga particularly result in very low resistivities so studies on those dopants have been relatively active than the others. Indeed, Al doped ZnO is generally adopted for electrodes for solar cells based on amorphous Si and CIGS solar cells as a window electrode due to its high conductivity and low temperature processability. A resistivity of Al doped ZnO films on the order of 10^{-5} Ωcm has been achieved by the PLD process.[60] In general, the oxygen content in ZnO is a critical parameter to obtain highly conductive films and its control is rather difficult compared to other TCOs based on SnO_2 and In_2O_3 due to chemically active Zn atoms in oxidizing atmosphere. This indicates that the optimization of oxygen contents during the deposition process needs to be carefully performed. Otherwise, ZnO suffers from low conductivity caused by non-optimized stoichiometry with excess oxygen species, i.e. lack of oxygen vacancies.[65]

Dopant	Dopant content (wt%)	Resistivity $\times 10^{-4}$ (Ω cm)	Carrier concentration $\times 10^{20}$ (cm^{-3})
Al_2O_3	1–2	0.85	15.0
Ga_2O_3	2–7	1.2	14.5
B_2O_3	2	2.0	5.4
Sc_2O_3	2	3.1	6.7
SiO_2	6	4.8	8.8
V_2O_5	0.5–3	5.0	4.9
F	0.5 (at%)	4.0	5.0
None	0	4.5	2.0

Table 3.2. *The types of dopants in ZnO with corresponding dopant content, resistivity, and carrier concentration; taken from [60].*

Optimization of the doping concentration is also a critical factor to obtain conductive thin films. To obtain a high carrier concentration in ZnO, the optimization of the extrinsic dopant content is of importance to supply enough free electrons. However, excess dopants deteriorate the structural, electrical, and optical properties of ZnO films due to the high ionized impurity scattering. Although the carrier concentration of ZnO has reached the order of $1 \sim 3 \times 10^{21}$ cm^{-3}, higher carrier concentration is limited to a solubility of the donor content in ZnO.[66] As shown in **Fig. 3.2**, the mobilities of ZnO films are strongly governed by the ionized impurity scattering in the high carrier concentration regime ($10^{20} \sim 10^{21}$ cm^{-3}).[67] A large amount of point defects such as O vacancies, excess Zn atoms, and external dopants become ionized impurities in ZnO.

In contrast, in the low carrier concentration regime, the grain boundary scattering is dominant. Grain boundaries have a lot of lattice defects-induced trapping states such as chemisorbed oxygen atoms. These states can be compensated by charge carriers, which make the grain boundaries negatively charged, creating potential barriers across depletion regions. The resulting potential barriers strongly scatter and hinder the transport of electrons. With increasing carrier concentrations, the potential barrier decreases due to the saturation of trapping states, resulting in increasing mobilities. At carrier concentrations above about $1 \sim 3 \times 10^{20}$ cm^{-3}, the potential barrier becomes narrow enough so electrons can tunnel through the barriers. Thus, the carrier scattering is no longer limited by the potential barrier at the grain boundary. Above a certain point, carrier transport is governed by the ionized impurity scattering. The mobility decreases again with increasing the carrier concentration. The

detailed mechanism is well described by Ellmer et al.[65-67] The behavior of the mobility and the carrier concentration of ZnO films is presented in **Fig. 3.2**.[67]
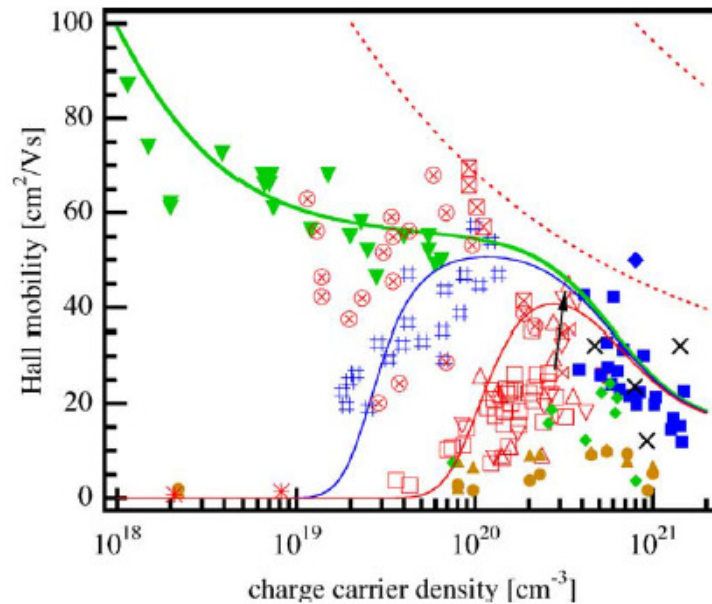

Figure 3.2. Hall mobilities versus carrier concentrations of ZnO single crystals (green ▼) and undoped (#) and doped (the others) ZnO films on glass (full symbols) and single crystalline substrates (open symbols); taken from [67].

3.1.4. Applications in OPV cells and OLEDs

Doped ZnO films have been extensively studied and have the longest history among alternative electrode materials. Their low material cost, non-toxicity, high transmittance and conductivity are great advantages. The electrical and optical properties of doped ZnO films have long reached those of ITO.[60, 63] However, the chemical instability under acidic PEDOT:PSS typically used as a hole transport layer in polymer solar cells is still a critical issue, which significantly deteriorates the OPV and OLED performance.[60, 68, 69] Moreover, the low work function of the ZnO films causes unfavorable energy level alignment, resulting in a hole injection problem.[70-72] Because of these reasons, the efficiency of ZnO-based OPV cells still lags behind that of ITO-based OPV cells.

In 2000, Kim et al. investigated Al doped ZnO electrodes grown by a PLD process for the OLED application. Although OLEDs on doped ZnO electrodes revealed lower efficiencies compared to the ITO reference device due to the lower work function of ZnO, they showed the potential of ZnO electrodes for organic electronic devices.[73] Tomita et al. demonstrated vacuum deposited green and white p-i-n OLEDs based on Al doped ZnO films, showing low

operating voltages and high efficiencies.[74] In 2007, Bhosle et al. reported Ga doped ZnO electrodes for organic photovoltaic (OPV) cells. The efficiency of OPV cell based on the Ga doped ZnO was 1.25 %.[71] Owen et al. also presented the OPV cell with Ga doped ZnO electrode with an efficiency of 1.4 %.[75] In chapter 6, we demonstrate high efficiency OPV cells and OLEDs based on ZnO electrodes doped with non-metallic dopants. The optimized ZnO electrodes show outstanding optical properties of low absorption loss, high transmittance, and low refractive indicies.

3.2. PEDOT:PSS

3.2.1. Introduction

Since Alan J. Heeger, Alan MacDiarmid, and Hideki Shirakawa, who were awarded the 2000 Nobel Prize in Chemistry, discovered highly conductive oxidized iodine-doped polyacetylene in 1977,[76, 77] intrinsic conductive polymers have been extensively studied due to the enormous potential as an alternative conductor. Doped polyacetylene reaches a conductivity of more than 10^5 S/cm, showing a metallic behavior. However, polyacetylene suffers from a strong degradation behavior in ambient and poor processability. In addition to polyacetylene, polyanilines, polythiophenes, and polypyrroles have also been investigated as conductive polymers. However, polyanilines, which are toxic, suffer from poor stability, polythiophenes and polypyrroles are insoluble in most of solvents.[78, 79] Achieving conductivity, processability, and stability together in conductive polymers is a key issue for practical applications.

Since a new polythiophene derivative, poly(3,4-ethylenedioxythiophene) (PEDOT), was developed by Bayer AG in 1988,[80, 81] PEDOT is regarded as one of the most promising conducting polymers for practical applications because of its high conductivity and transparency as well as good thermal and chemical stability.[82, 83] The PEDOT derivative thin films, built from solution dispersed in water, can be deposited by spin coating, dip coating, doctor blade, inkjet printing, and screen printing techniques.[82, 83]

3.2.2. Chemical and structural properties

PEDOT, built from ethylenedioxythiophene (EDOT) monomers, shows a high conductivity and transparency in oxidized states. However, it is insoluble in most solvents and unstable in its neutral state. The poor solubility can be improved by introducing water-soluble

polyelectrolyte, poly(styrenesulfonate) (PSS).[82, 83] The acidic SO₃H (sulfonate) group is attached to respective phenyl rings of the PSS monomers (**Fig. 3.3**). PSS plays an important role as a charge-balancing dopant, i.e. the oxidizing agent and acts as a template polymer based on its high molecular weight. The positively charged PEDOT is positioned on the negatively charged PSS matrix by an oxidizing process.
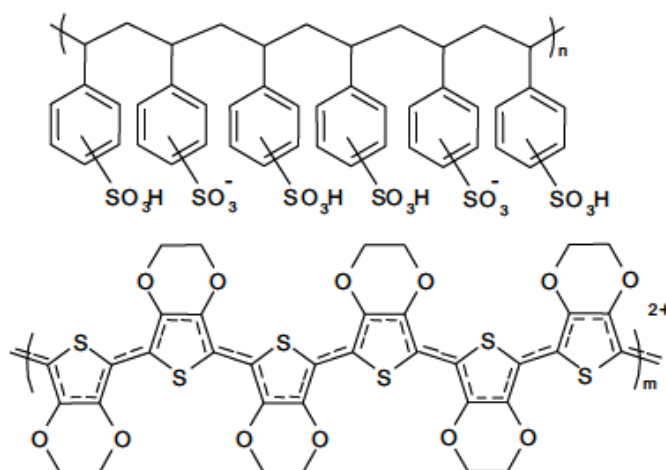
Figure 3.3. Molecular structure of PEDOT:PSS.

The resulting PEDOT:PSS films possess a high conductivity (up to ~1 S/cm) and a high transparency with a low optical bandgap.[82, 83] However, excess PSS makes the PEDOT:PSS films hygroscopic, leading to significant water uptake into films. In addition, insulating PSS acts as a barrier between PEDOT-rich grains, hindering the hopping process of charge, and limits the conductivity of films. Furthermore, it is reported that flattened PEDOT-rich grains surrounded by PSS strongly limit the conductivity in vertical direction of films. Nardes et al. showed PEDOT-rich grains surrounded by thin PSS shells as shown in **Fig. 3.4**.[84]

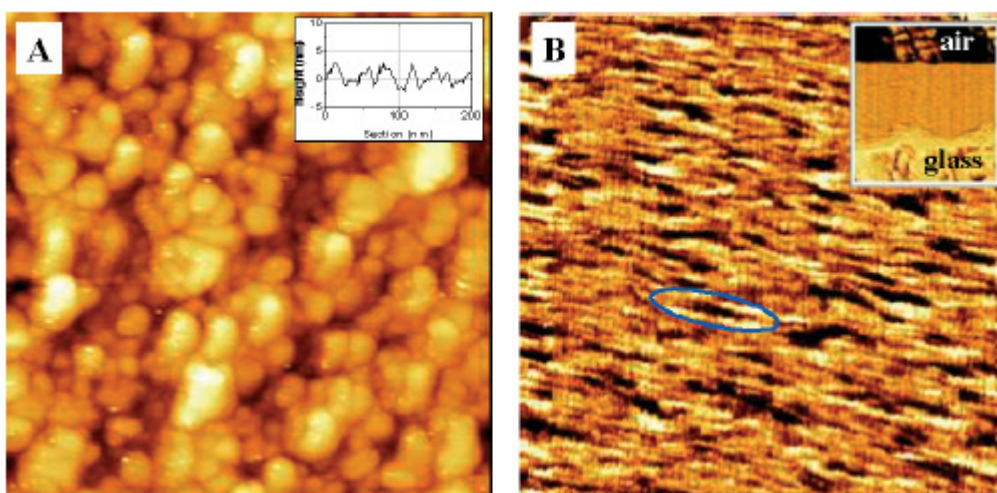*Figure 3.4.* (a) Topographic scanning tunneling microscope (STM) image of PEDOT:PSS on ITO. (200 nm × 200 nm) (b) Cross-sectional atomic force microscopy (AFM) phase image of cleaved PEDOT:PSS on glass substrate, vertical scale is 8°.(200 nm × 200 nm); taken from [84].

3.2.3. Solvent addition in PEDOT:PSS

It is well known that addition of high-boiling point solvents, such as ethylene glycol (EG), glycerol, dimethyl sulfoxide (DMSO), N,N-dimethylformamide, and sorbitol significantly improves the conductivity of PEDOT:PSS up to 2 or 3 orders of magnitude.[85-87] Besides using solvents, many approaches to increase the conductivity of PEDOT have been studied. Conductivities higher than 1100 S/cm have been reported from vapor phase polymerized PEDOT.[88] The polymerization of EDOT by using the derivative monomer (EDOT-CH_2OH) with the oxidant (iron(III)-tosylate) and weak base (imidazole) yielded conductivities as high as 900 S/cm.[89] On the other hand, solvent added PEDOT:PSS shows somewhat lower conductivities (470 S/cm using PH500 from Heraeus, Germany with DMSO,[90] 570 S/cm using PH750 with DMSO[91]) compared to the alternative processes, because excess PSS, necessary for dispersion in water, is present in the formulations and disturbs the conduction path inside the polymer film. Recently, a solvent post-treatment proposed by us significantly improved the conductivity of PEDOT:PSS (PH1000) to ~1400 S/cm.[92] The detailed information will be discussed in chapter 5. Xia et al. reported that ~3000 S/cm of conductivity by acidic treatment on PEDOT:PSS (PH1000).[93]

The mechanism of the improved conductivity in PEDOT:PSS by solvent addition is still not clear. There have been several proposals for the conductivity enhancement mechanisms. Kim

et al. reported that high dielectric constant solvents produce a screening effect, resulting in improvement of conductivity by disrupting interaction between carriers and ions.[94] Crispin et al. investigated morphological changes of the solvent added PEDOT:PSS and enhanced conductivities by solvents, which were attributed to the better contact of conducting PEDOT-rich grains caused by segregation of insulating PSS layer.[86] Ouyang et al. observed a conformational change of PEDOT:PSS films by adding solvent.[85, 95] They claimed that the modified chain in solvent added PEDOT:PSS films from coil to linear structures caused the high conductivity due to an improvement of carrier movement. Especially, the morphological as well as chemical changes of PEDOT:PSS by a solvent treatment were observed in our experiment. When spun PEDOT:PSS is dried, high-boiling solvents and water evaporate, which greatly transform the morphology of films and phase separation between PEDOT-rich and PSS-rich grains occurs. The observed solvent treatment effects and improved conductivity in PEDOT:PSS will be discussed in chapter 5.

3.2.4. Applications in OPV cells and OLEDs

Due to the high conductivity and high transparency, ease of processing, high flexibility, high work function, and good stability, PEDOT:PSS thin films are widely used as a buffer layer or an electrode for OPV cells and OLEDs. For a buffer layer, PEDOT:PSS is coated between an electrode and organic layers, showing several benefits. PEDOT:PSS can flatten the surface of ITO, reducing the roughness and spikes on the ITO surface which prevents possible electrical short paths. In addition, PEDOT:PSS allows excellent energy level matching between the electrode and organic layers. Typical work functions of PEDOT:PSS and ITO are around 5.0 ~ 5.2 and 4.5 ~ 4.8 eV, respectively. The lower work function of ITO typically leads to the formation of a charge injection barrier which deteriorates the performance of organic devices. When PEDOT:PSS is introduced in between the ITO and the hole transport layer of organic devices, ohmic contact occurs at the interfaces, which results in the excellent hole transport property. However, the strong acidity (pH = 1 ~ 2) and hygroscopic nature of PEDOT:PSS sometimes cause indium and water diffusion into organic layers, which frequently deteriorates the stability of organic devices.[59, 68]

Besides the applications in buffer layers, the high conductivity and high transparency of PEDOT:PSS allow the use as an electrode for organic devices. In 2002, Zhang et al. successfully employed PEDOT:PSS with glycerol or sorbitol for OPV cells and showed an efficiency of 0.36 % under AM1.5 with a sun intensity of 78 mW/cm^2.[96] Fehse et al.

achieved a comparable efficiency of PEDOT:PSS (PH500 with DMSO)-based OLEDs to that of ITO-based OLEDs.[97] They attributed the improvement to good optical properties (low refractive index) of PEDOT:PSS and a lower energy barrier formed at the interface of the electrode and the transport layer. Do et al. reported 3.5 % efficiency OPV cells based on PEDOT:PSS electrodes (PH750 with DMSO).[91] Xia et al. reported a conductivity of PEDOT:PSS as high as ~3000 S/cm, which was successfully adopted as an electrode for OPV cells.[93] Lipomi et al. demonstrated stretchable OPV cells with PEDOT:PSS electrodes on buckled PDMS substrates.[98] We investigated optimized PEDOT:PSS electrodes by a solvent post-treatment, showing greatly improved conductivity (~1400 S/cm) and a comparable efficiency of PEDOT:PSS-based OPV cell to the ITO reference device.[92] In addition, it was observed that these post-treated PEDOT:PSS films significantly improves the lifetime of OPV cells.[99] This will be further discussed in chapter 5.

3.3. Carbon nanotubes

3.3.1. Introduction

Carbon nanotubes (CNT) are a promising material as a transparent conductive electrode for optoelectronic devices because of their excellent electrical and optical performance as well as good mechanical flexibility, chemical stability, and low-cost roll-to-roll compatible manufacturing process. CNTs are cylindrical nanostructures of carbon as a rolled up graphene sheet. The CNTs extraordinarily exhibit a high electron mobility on the order of 10000 cm^2/Vs.[100-102] Their unique properties originate from their structures. The honeycomb-like graphene lattices in the CNTs are sp^2 hybridized with delocalized π bonds. The diameter of the CNT is in the nanometer range (typically 0.7 ~ 3 nm), showing quasi one dimensional structure but its length can be scaled up to even centimeters, reaching a length to diameter ratio of 10^7. CNTs have single-walled (SWNT) or multi-walled (MWNT) structures, and are able to be functionalized with carboxyl groups or fullerenes. CNTs were first discovered by Iijima et al. in 1991 in the form of MWNT.[103] In 1993, the first SWNT was developed.[104, 105] CNTs are synthesized by several techniques such as the arc-discharge, laser ablation, chemical vapor deposition (CVD), and high pressure carbon monoxide (HiPCO) methods. The resulting CNTs are dispersed in a solvent, typically water with the use of surfactants, which is so-called CNT ink. The transparent conductive CNT films are subsequently prepared by spraycoating, spincoating, ink-jet printing, or vacuum filtration from CNT ink.
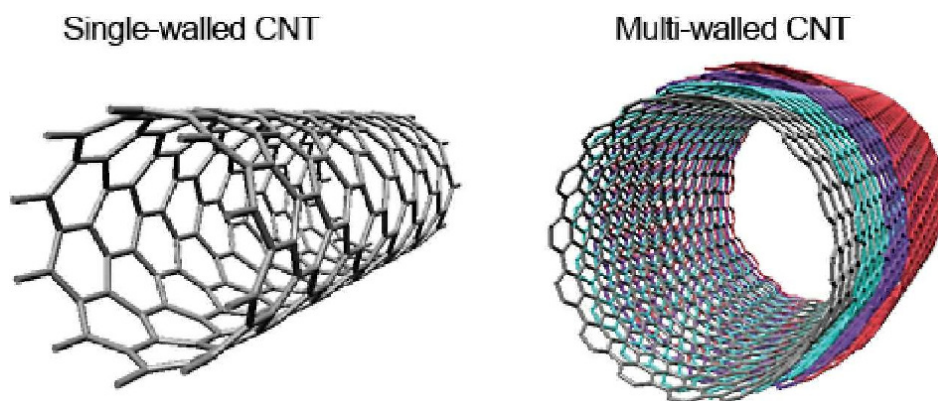
Figure 3.5. *Single-walled (left) and multi-walled (right) CNT structures; taken from [106].*
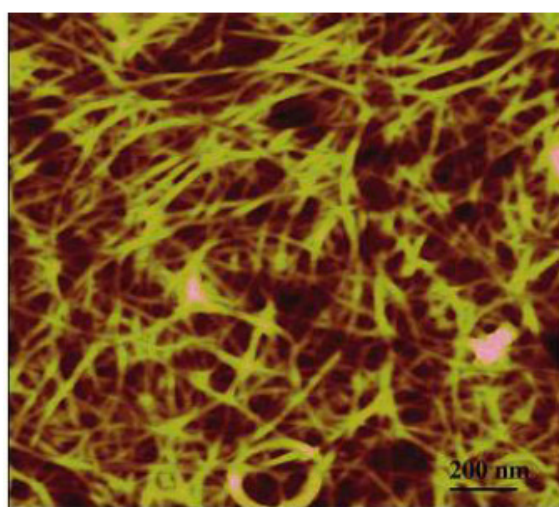

Figure 3.6. *AFM image of a transferred SWNT film on a PET substrate (RMS roughness of 6 ~ 10 nm); taken from [107].*

3.3.2. Applications in OPV cells and OLEDs

In 2005, Wu et al. investigated high purity SWNT as a transparent conducting material.[108] Zhang et al. also reported free-standing conductive MWNT sheet and successfully made OLEDs on the CNT electrodes.[109] Based on the excellent electrical, optical, and mechanical properties of CNT electrodes, applications of the transparent electrode to OPV cells and OLEDs have been extensively investigated. The application has focused on the use of SWNT via the solution based processes and as bottom electrodes for opaque devices.[110-114] However, it is noted that the inherent roughness of CNTs easily provokes the electrical shorts in devices. Thus, in general, application of CNT electrodes requires smoothing buffer layers such as PEDOT:PSS to prevent short of delicate organic devices. In 2005, Pasquier et al. reported OPV cells with SWNT with an efficiency of 1 %.[111] Rowell et al. demonstrated a printed SWNT film (T = 85 %, R_S = 200 Ω/sq) as an electrode for OPV cells, showing an efficiency

of 2.5 %.[113] Zhang et al. successfully fabricated ITO-free OLEDs with optimized CNT sheets by SOCl$_2$ doping (T = 87 %, R_S = 160 Ω/sq).[115]

The roll-to-roll compatible free-standing MWNT (f-CNT) sheets reported by Zhang et al., which are highly conductive, transparent and show high mechanical strength, are a promising top electrode material.[109] One of the great advantages of the dry spun f-CNT sheets is the scalable fabrication of meter-long sheets with uniform electrical and optical properties. Those f-CNT sheets offer unique applications and were successfully adopted as a bottom electrode for OPV cells and OLEDs, showing reasonable performances.[116, 117] Moreover it has been demonstrated that f-CNT sheets, which have inherently high porosity, can provide three-dimensional (3-D) charge collection from the volume of the bulk heterojunction OPV cells, with twice increased photo-current.[116] Additionally, Tanaka et al. have first reported a parallel tandem architecture of OPV cells with f-CNT as an intermediate electrode, showing increased total photo-current although at yet small efficiency of 0.31 %.[118] Parallel tandem architectures requires the bottom cell to be semi-transparent, and one of subcells to be inverted in such a way that the common intermediate CNT electrode collects charges of same sign, adding to total current, contrary to the conventional series tandem structure, in which opposite charge carriers recombine at the interlayer.[119, 120] In chapter 7, we show semi-transparent OPV cells with laminated free-standing CNT top electrodes.
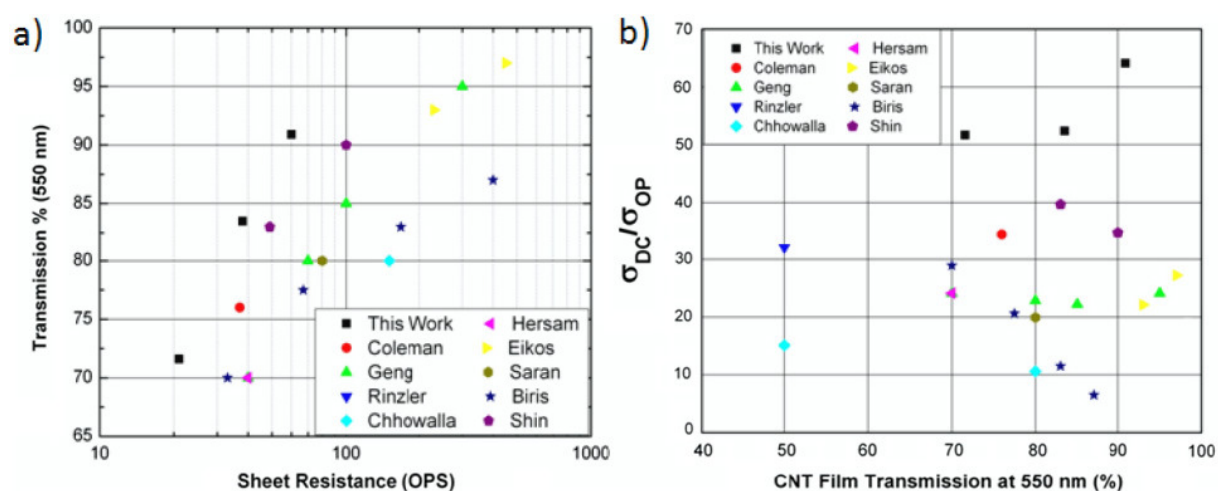

Figure 3.7. *a) Sheet resistance versus transparency values for transparent conductive CNT films b) Ratio of DC and optical conductivity of various CNT films; taken from [121].*

3.4. Other transparent electrodes

3.4.1. Silver nanowires

Ag nanowire (AgNW) films have been widely investigated in recent years and have already shown electrical and optical properties comparable to the conventional ITO electrodes. AgNWs have the advantage of low temperature and solution processability. Lee et al. reported solution processed AgNWs ($T = 86\%$, $R_S = 16$ Ω/sq) and showed its first application to OPV cells with an efficiency of 0.38 %.[122] They also demonstrated a semitransparent OPV cell with a laminated AgNW top electrode and an ITO bottom electrode, exhibiting an efficiency of 0.63 %.[123] Due to a high surface roughness of the nanowires, a fabrication of thin film organic devices frequently suffers from high leakage currents or electrical short. Thus, transferring methods of AgNWs have been developed in recent years for obtaining a smooth electrode surface. Buried AgNW networks below a polymer matrix were developed and the root mean square (RMS) roughness of the AgNW film was greatly reduced from 75 nm to 1 nm by using the buried AgNW composite methods.[124] Li et al. demonstrated high efficiency phosphorescent OLEDs based on a smooth AgNW-polymer composite electrode by a peeling-off process, which greatly suppressed the roughness induced problems.[125] AgNWs transferred onto PEDOT:PSS films were also investigated and a low RMS roughness of ~ 12 nm was obtained. The resulting OPV cell with AgNW composites showed a comparable efficiency to the ITO reference cell with an efficiency of 4.2 %.[126]
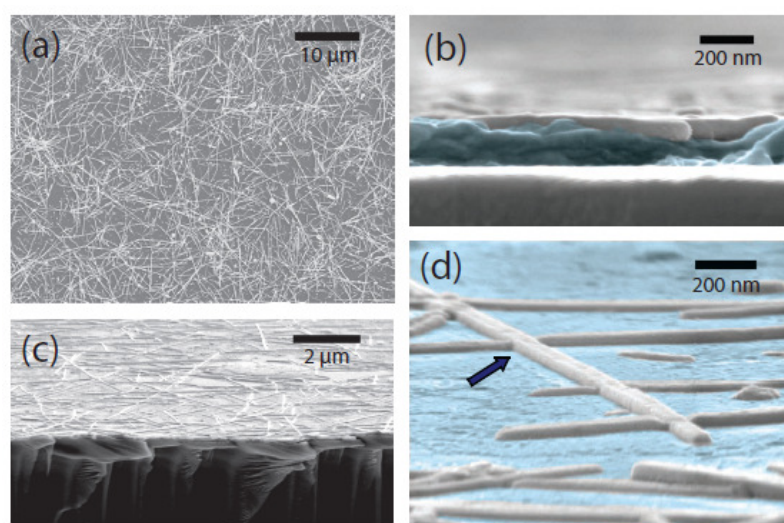

Figure 3.8. SEM images of AgNW/PEDOT:PSS composite a) Top view. b) Cross-section view. c) Tilted view. d) Nanowires embedded into the polymer; taken from [126].
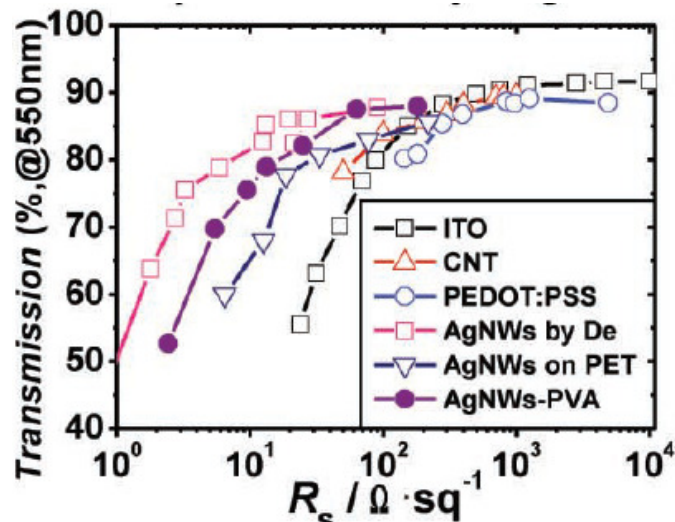
Figure 3.9. *Transparency (at 550 nm) versus sheet resistance values of AgNW/polymer composite and typical transparent electrodes; taken from [124].*

3.4.2. Thin metal films and dielectric/metal/dielectric films

If metal films are sufficiently thin, usually less than 20 nm, it can be used as a transparent electrode. The major challenge for thin metal electrodes is to make the metal films thin enough for the sufficient transparency while retaining continuous films with connected electrical percolation paths for the high conductivity. In addition, the deposition of the metal film for a top electrode needs to be carried out without damaging underlying organic layers, which is a critical issue for the top electrode application in OPV cells and OLEDs. For example, ITO deposition by sputter processing on organic devices induces serious damage to underlying organic layers, causing undesirable leakage currents in devices.[127, 128]

Thin metal layers prepared by thermal evaporation have been widely investigated as a top electrode of OPV cells and OLEDs.[129-133] A high efficiency of 4.9 % was achieved by a tandem structure with thin metal top electrodes,[132] indicating a promising future of semi-transparent OPV cells. Meiss et al. extensively investigated thin Ag films for top electrode of small molecule OPV cells. The optimization of morphology of Ag films for OPV cells was systemically investigated by using the thin Al seed layer.[134] Furthermore, it is known that additional organic capping layers on the thin metal contacts remarkably improve the performance of OPV cells by enhanced light in-coupling.[135] The ITO-free OPV cells with thin metal films optimized by thicknesses of Al seed layers and Ag layers showed an efficiency of 2.2 %.[133] Lin et al. reported high-performance ITO-free OPV cells with microcavity structures consisting of thin Ag top/capping layer and thick Ag bottom/spacer

layer, achieving an efficiency of 5.5 % by controlling of the top in-cell spacer layer and the out-of-cell capping layer.[136]

Figure 3.10. *A photograph of the semi-transparent OPV cell with an efficiency of 4.9 % and transparency of 24 %; taken from [132].*

Dielectric/metal/dielectric (DMD) multilayer structures are also widely investigated for OPV cells and OLEDs. The ultrathin metal layer sandwiched by two dielectric layers plays a role to provide the conductivity and the two dielectric layers allow for the high optical transparency by a combined light interference effect. For the metal layer, Ag thin films are typically used. MoO_3 and WO_3 are generally investigated for inner and outer dielectric layers. A high efficiency flexible green OLED achieving an EQE of 40 % was fabricated with Ta_2O_5/Au/MoO_3 structure as a bottom electrode, which significantly enhanced light out-coupling of devices.[137] Schubert et al. investigated thermally evaporated MoO_3, WO_3, and V_2O_5 layers with thin Ag film as top electrodes and showed strongly improved lifetime of standard ZnPc:C_{60} cell compared to pure Ag top contacts.[138] The lifetime enhancement was attributed to the passivation effect of the metal surface by dielectric layers. The MoO_3/Ag/MoO_3 bottom electrode structure for ITO-free OPV cells with an efficiency of 4.4 % was reported recently.[139]

3.4.3. Graphene

Graphene, a single molecular sheet with sp^2 hybridized carbon, is regarded as a promising two-dimensional material with excellent electrical, optical, thermal, and mechanical properties. Since 2005, randomly distributed graphene networks or graphene based composite electrodes are extensively studied. Due to outstanding electrical properties such as high

conductivity, high mobility, functionality with dopants, and chemical stability of graphene, it has attracted much attention as an electrode or a transport layer for OPV cells and OLEDs.[140-142] Wu et al. reported small molecules OPV cells with reduced graphene oxide electrodes (thickness: 4-7 nm, T = 85-95 %, R_S = 100-500 kΩ/sq), showing an efficiency of 0.4 %.[143] Flexible OPV cells with reduced graphene oxide electrodes (T = 55 %, R_S = 1.6 kΩ/sq) showed an efficiency was 0.78 %.[144] The poor efficiencies of graphene-based OPV cells were attributed to the very high sheet resistance of graphene electrodes. A CVD process is a successful method to prepare high quality graphene films with a high conductivity. Conductive graphene films (T = 72 %, R_S = 230 Ω/sq) produced by the CVD process showed a decent performance (efficiency ~1.2 %) comparable with the ITO-based device.[145] A direct layer-by-layer transfer method of graphene films produced by the CVD process was investigated for the highly conductive graphene sheets. Four layer acid-doped graphene (T = 90 %, R_S = 80 Ω/sq) was used as a bottom electrode of OPV cells and it showed an efficiency of 2.5 %.[146] Choe et al. reported a 2.6 % efficiency OPV cells with multilayer graphene electrodes (T = 87 %, R_S = 606 Ω/sq) grown by the CVD process.[147] Graphene-based OLEDs (T = 82 %, R_S = 800 Ω/sq) reported by Wu et al. showed a comparable EQE and power luminance to those of ITO reference device.[148]
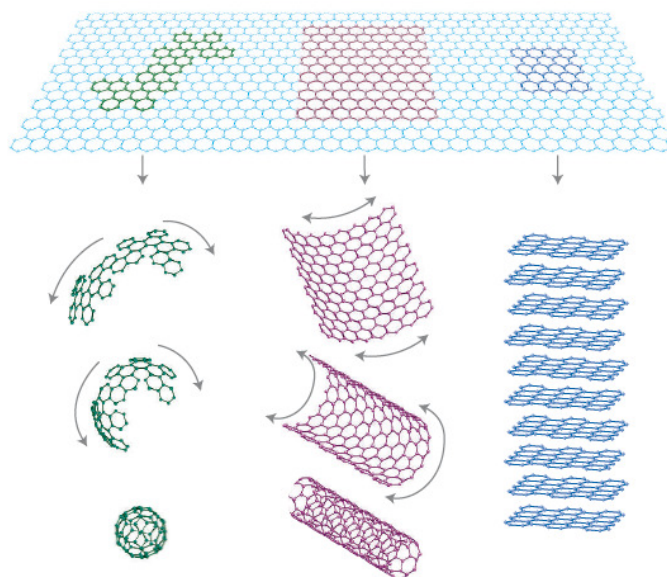

Figure 3.11. *A schematic illustration of possible carbon nanomaterials. "It can be wrapped up into 0D buckyballs, rolled into 1D nanotubes or stacked into 3D graphite."; taken from [149].*

Chapter 4. Experimental

This chapter presents the organic and electrode materials used in this work, electrode and device fabrication methods, and material and device characterization.

4.1. Materials

4.1.1. Absorber materials for OPV cells

- **C_{60}**

Fullerene (C_{60}) is the most widely used acceptor material for small molecule OPV cells. It is entirely composed of carbon atoms with a very high symmetry so it is called buckyballs. The main absorption peaks of C_{60} are observed at 350 nm and 450 nm. The electron affinity (EA) and ionization potential (IP) of C_{60} are around 4.0 and 6.4 eV, respectively. C_{60} is also used as an electron transport material in small molecule-based devices. The reported mobilities of C_{60} are as high as 11 cm^2/Vs.[150] When it is doped with an n-dopant, such as $Cr_2(hpp)_4$ or $W_2(hpp)_4$, its conductivity reaches up to 4 S/cm.[151] The material is supplied by Bucky USA.

- **ZnPc**

Zinc phthalocyanine (ZnPc) is a common donor material for small molecule OPV cells. The main absorption peaks are observed at the wavelength of 350 nm, 630 nm, and 710 nm, and its absorption coefficient is higher than 10^{-5} cm^{-1}. The IP and EA of ZnPc are around 5.1 and 3.3 eV, respectively, with a bandgap of around 1.54 eV.[152] The material is supplied by TCI Europe, ABCR GmbH, and CreaPhys GmbH.

- **F4**-**ZnPc**

The fluorinated zinc phthalocyanine (F4-ZnPc) is modified by fluorination, resulting in higher open circuit voltage compared to pure ZnPc as reported recently.[153] The blend layer of F4-ZnPc:C_{60} can be heated at around 100 ^{o}C for better crystallinity and nanomorphology, leading to improved fill factors and short circuit current densities of OPV cells. The material is supplied by BASF.
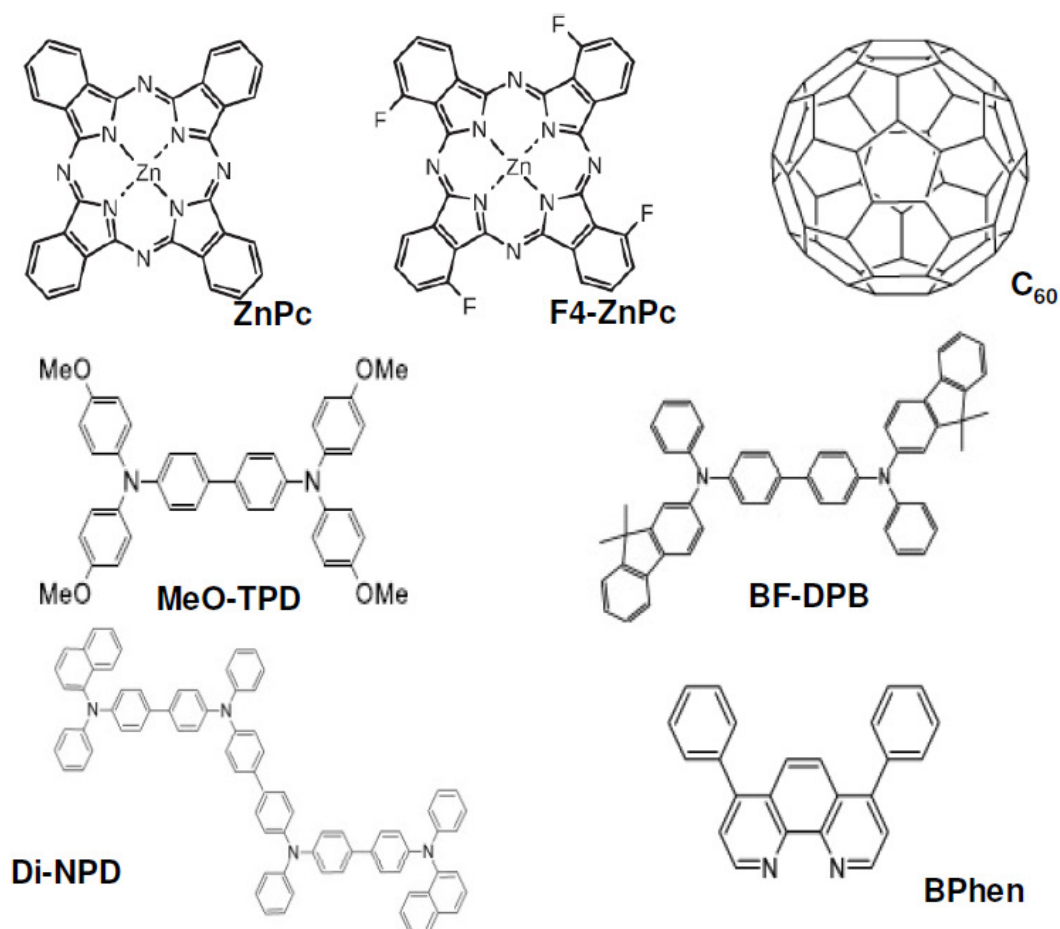
Figure 4.1. *Organic materials for OPV cells.*

4.1.2. Emission materials for OLEDs

Phosphor materials are diluted in a host material such as 4,4',4''-tris(N-carbazolyl)-triphenylamine (TCTA), 2,2'2''-(1,3,5-benzenetriyl)-tris[1-phenyl-1H-benzimidazole] (TPBi), N,N'-di-1-naphthalenyl-N,N'-diphenyl-[1,1':4',1'':4'',1'''-Quaterpheny]l-4,4'''-diamine (4P-NPD), or N,N'-di(naphthalene-1-yl)N,N'-diphenyl-benzidine (NPB) for highly efficient phosphorescence.

- **Ir(ppy)₃**

Tris(2-phenylpyridine)-iridium (Ir(ppy)$_3$) is incorporated in TCTA or TPBi for efficient and stable green emission (peak: 511 nm). The material is supplied by Lumtec.

- **Ir(MDQ)₂(acac)**

Iridium(III)bis(2-methyldibenzo-[f,h]chinoxalin)(acetylacetonat) (Ir(MDQ)$_2$(acac)) is used in NPB or 4P-NPD for efficient and stable orange-red emission (peak: 614 nm). The material is supplied by Lumtec.

54

- Ir(dhfpy)₂(acac)

Bis(2-(9,9-dihexylfluorenyl)-1-pyridine) (acetylacetonate) iridium(III) (Ir(dhfpy)₂(acac)) is used in TCTA or TPBi for efficient and stable yellow emission (peak: 557 nm).
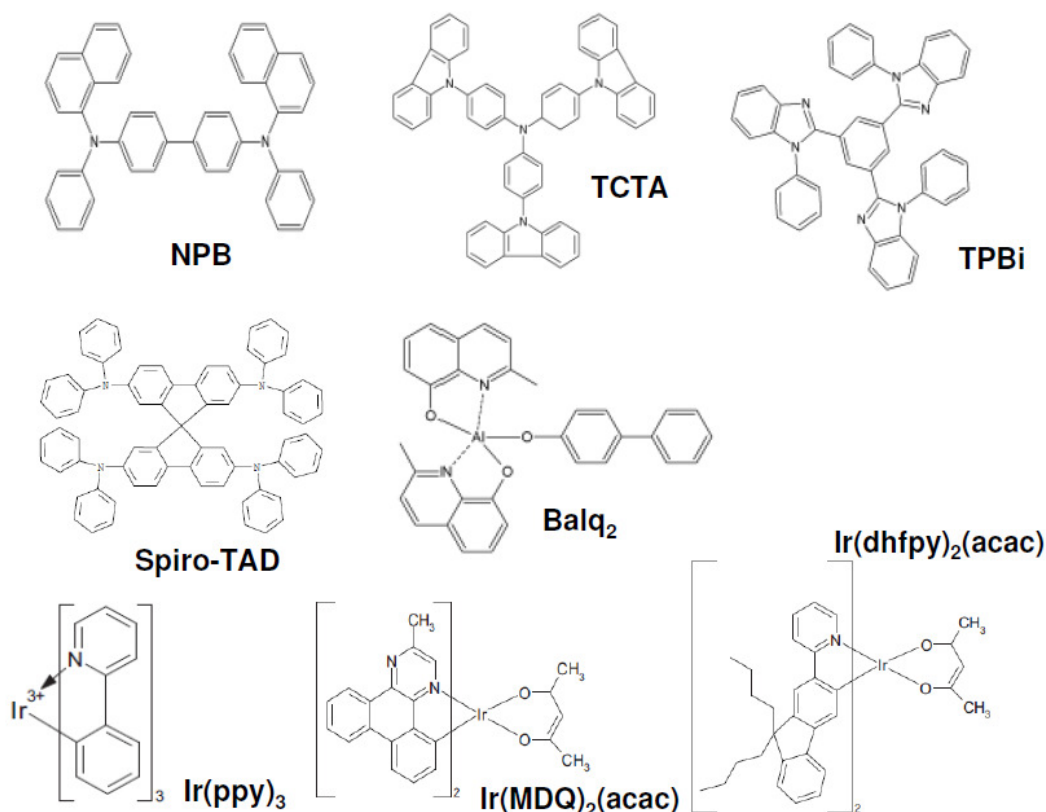
Figure 4.2. Organic materials for OLEDs.

4.1.3. Charge transport/blocking materials and dopants

- MeO-TPD

N,N,N',N'-tetrakis(4-methoxyphenyl)benzidine (MeO-TPD) is a commonly used hole transport material for OPV cells and OLEDs. It has an IP of around 5.1 eV and a wide bandgap of around 2.9 eV.[154] The material is supplied by Sensient.

- BF-DPB

N4,N4'-bis(9,9-dimethyl-9H-fluoren-2-yl)-N4,N4'-diphenylbiphenyl-4,4'-diamine (BF-DPB) is a wide bandgap (~ 3.0 eV) hole transport material with an IP of around 5.2 eV. The material is supplied by Sensient.

- Di-NPD

N,N'-Diphenyl-N,N'-bis(4'-(N,N-bis(naphth-1-yl)-amino)-biphenyl-4-yl)-benzidine (Di-NPD) is used as a hole transport layer with a deep IP of 5.35 eV. The bandgap of Di-NPD is around 2.9 eV. It is known to have a better thermal stability than other hole transport materials. The material is supplied by Sensient.

- BPhen and BPhen:Cs

4,7-diphenyl-1,10-phenanthroline (BPhen) is an electron transport material with a wide bandgap of about 3.52 eV. It has an IP of 6.5 eV and an EA of 3.0 eV. It is used as an exciton blocking layer for OPV cells due to its wide bandgap. It can be doped by the co-evaporation of Cs (BPhen:Cs = 1:1) and be used as an electron transport layer (hole blocking layer) for OLEDs. The material is supplied by ABCR GmbH.

- Balq$_2$

Bis(2-methyl-8-chinolinolato)-4-(phenyl-phenolato)-Aluminum-(III) (Balq$_2$) is a hole blocking layer for OLEDs with an IP of around 6.1 eV and a band gap of around 3.44 eV. The material is supplied by Sensient.

- Spiro-TAD

2,2',7,7'-tetrakis-(N,N'-diphenylamino)-9,9'-spirobifluorene (Spiro-TAD) is used as an electron blocking layer for OLEDs with an EA of around 2.2 eV having a wide bandgap. The material is supplied by Lumtec.

- 4P-NPD and TPBi

4P-NPD and TPBi are also used as an electron and hole blocking layer for OLEDs, respectively. The materials are supplied by Lumtec and Sensient, respectively.

- Organic dopants

2,2'-(perfluoronaphthalene-2,6-diylidene)dimalononitrile (F6TCNNQ) and NDP9 are strong acceptor molecules for p-type doping in hole transport materials, provided by Novaled AG (Dresden, Germany). Their electrical properties behave similarly to other common p-dopants but they have easy processiblity and better thermal stability. W$_2$(hpp)$_4$, supplied by Novaled AG, is an n-dopant for electron transport materials. It is very reactive due to its low IP.

4.1.4. Electrodes

- ITO

Indium tin oxide (ITO) substrates (Thin Film Devices Inc.) with a sheet resistance of around 30 ohm/sq and a transmittance of around 84 % in the visible range are used for reference OPV cells and OLEDs. The work function of ITO is around 4.8 eV.

- PEDOT:PSS

Poly(3,4-ethylenedioxythiophene):poly(styrenesulfonate) (PEDOT:PSS) (Clevios PH1000 from Heraeus, Germany) solutions are mixed with ethylene glycol (EG) for high conductivity. The formulations are filtered with 0.45 μm syringe filters and spin-coated on substrates, pre-treated in oxygen plasma for 15 min. All films are subsequently annealed on a hot plate at 120 °C for 15 min in ambient atmosphere. Some of the films are post-treated in the EG bath for further increasing conductivity, which will be described in detail in chapter 5. For device applications, PEDOT:PSS electrodes are heated for at least 30 min in the vacuum chamber above 110 °C, just before evaporation of organic layers to remove residual water from the hygroscopic film. The work function of PEDOT:PSS is around 5.0 eV.

- ZnO

Doped ZnO films are deposited on glass substrates by radio frequency magnetron sputtering from a ceramic target (ZnO with Al_2O_3 1 wt.% or 2 wt.%, ZnO with ZnF_2 10 wt.%), which are fabricated at Korea Institute of Science and Technology. The non-metallic doping of ZnO films is carried out by introducing H_2 or CF_4 gas into Ar base gas. The base pressure in the chamber is kept below 7×10^{-7} mbar. The sputtering deposition is carried out at a pressure of 1.3 mbar and a substrate temperature of 150 ^{o}C with an rf power of 50 W. The distance between the target and the substrate is 60 mm, and the substrate is rotated at a constant speed of 12 rpm during sputtering. The doping processes are described in detail in chapter 6.

- Carbon nanotubes

The free-standing carbon nanotube (CNT) forests are prepared from a multiwalled CNT forest produced by a chemical vapor deposition (CVD) process at the Alan G. MacDiarmid NanoTech Institute as described elsewhere.[109] The lamination process of CNT sheet on top of OPV cells is described in detail in chapter 7.

- **Structuring of electrodes**

The electrode of thin films for use as bottom electrodes are laterally structured using laser ablation with a Nd:YAG layer (ACI Laser).

4.2. Fabrication methods and characterization

4.2.1. Device simulation & fabrication

- **Optical simulation**

The simulation is based on a transfer matrix approach to obtain the photo-generated current and the electromagnetic field for planar OPV cells and OLED structures, respectively.[155, 156]

- **Thermal evaporation**

Small molecule organic layers are prepared by thermal evaporation in a high vacuum system (K.J. Lesker, U.K.). The base pressure of the chamber is kept around 10^{-8} mbar. After evaporation of organic layers and top contact, some of devices are encapsulated with cover glass using epoxy glue, and getter material is placed in the cover glass cavity additionally.

4.2.2. Device characterization

- **Electrodes**

Sheet resistances of thin films are measured by using a four point probe setup with a source measurement unit (Keithley 2400). On each sample, 10 points are measured and averaged. The thicknesses of the films are measured by a surface profilometer (Veeco Dektak 150). Transmittance and absorption of films are obtained using a spectrophotometer (Shimadzu MPC3100, Perkin Elmer Lambda 900, or Perkin Elmer Lambda 35). The values of transmittance in this work include the optical loss of glass substrate (~ 8 %). The atomic force microscopy (AFM) images are taken in tapping mode (AIST-NT Combiscope).

- **OPV cells**

The current-voltage characteristics are measured with a source measurement unit (Keithley Instruments) under an AM 1.5G sun simulator (Steuernagel SC1200 or 16S-003-300-AM1.5 from Solar Light Co., USA). Some OPV cells without encapsulation are examined in a nitrogen filled glove box attached directly to the evaporation chamber. The values of short circuit current density are normalized to 100 mW/cm^2 with respect to a silicon photodiode, calibrated by Fraunhofer ISE (Freiburg, Germany). External quantum efficiency and spectral

mismatch factor are determined by a custom-made setup with a monochromatic beam and the current response of the device is measured via a lock-in amplifier.

- OLEDs

Current-voltage-luminance characteristics and electroluminescence spectra are measured by an automated measuring system with a Keithley SM2400 source measurement unit and a calibrated CAS140CT-153 spectrometer (Instrument Systems GmbH). External quantum efficiency and luminous efficacy are calculated with the spatial emission of the devices, carried out by a spectrogoniometer. The emission characteristics of the devices are obtained at angles from 0° to 90°. The integrated power efficacy and external quantum efficiency are determined by a spectrometer measurement in the integrating sphere on standard low index glass. A hemisphere lens with a diameter of 1.6 cm is used to out-couple the light, trapped in the glass mode, and mounted on the substrate with index-matching immersion oil (Zeiss, 518F n=1.518).

Chapter 5. Highly conductive PEDOT:PSS electrodes[*]

5.1. Introduction

Poly(3,4-ethylenedioxythiophene):poly(styrenesulfonate) (PEDOT:PSS), a conducting polymer showing fairly high conductivity and transparency, is regarded as a promising material for optoelectronic organic devices because it enables cost-effective and flexible devices as well as roll to roll mass production. In this work, we obtain highly conductive PEDOT:PSS films by using a solvent post-treatment method which remarkably increases the conductivity (**Fig. 5.1**). The electrical, optical, structural, and compositional changes of PEDOT:PSS films induced by the solvent post-treatment are investigated. We adopt optimized solvent post-treated PEDOT:PSS films as an electrode for ITO-free small molecule OPV cells. To improve the efficiency of solar cells, a pre-heating treatment of the PEDOT:PSS electrode is performed additionally. In addition, the effect of the post-treatment on the efficiency and the lifetime of PEDOT:PSS-based OPV cells is investigated.

Next, high performance ITO-free transparent OLEDs based on PEDOT:PSS electrodes are demonstrated. The device performance is carefully optimized by tuning the thickness of the optical spacer layer and the PEDOT:PSS electrode. We find optimum device structures for different types of electrodes and thus demonstrate the great importance of electrode-specific stack engineering.

Finally, we report on a novel concept to highly improve the performance of white OLEDs based on a combination of simply fabricated internal light extraction system composed of the metal oxide nanostructure and the highly conductive low refractive index PEDOT:PSS electrode. The OLEDs with the light scattering system show highly improved efficiency and color stability.
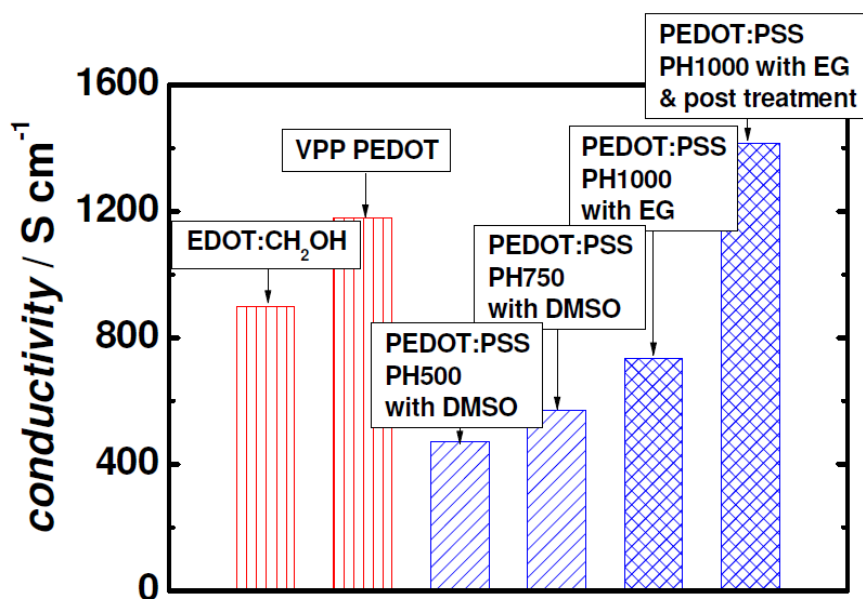
Figure 5.1. *Comparison of conductivities of various PEDOT thin films from literature and own results. Red columns with vertical lines denote PEDOT from literature*[88, 89] *with different anions, blue columns with diagonal lines denote PEDOT:PSS from literature,*[62, 91] *and blue columns with x-lines mark PEDOT:PSS from own results.*

5.2. Effects of post-treatment on PEDOT:PSS

- Preparation of PEDOT:PSS films

PEDOT:PSS solutions (PH1000) are mixed with ethylene glycol (EG). The formulations are spin-coated on glass and PET (Melinex ST504 from DuPont Teijin) substrates, pre-treated in oxygen plasma for 15 min. The spin speed and spin time are fixed at 5000 rpm and 30 s. All films are subsequently annealed on a hot plate at 120 °C for 15 min in ambient. Solvent post-treated films are prepared from PEDOT:PSS solution containing 6 vol.% of EG spin-coated and annealed as described above. Directly after annealing, the samples are immediately immersed and cooled in the EG bath for 0 ~ 30 min. Subsequently, the samples are annealed at 120 °C for 15 min. For multilayer coatings of PEDOT:PSS, spin speeds are varied between 2500 and 5000 rpm to control the film thickness. Each layer is deposited and heated at 120 °C for 15 min and solvent post-treatment is performed once, after deposition of the last layer.

- Results

Figure 5.2 (a) shows the dependence of the conductivity of PEDOT:PSS films on glass with respect to the concentration of EG added to the liquid PEDOT:PSS solution. The pristine

PEDOT:PSS films reveal poor conductivities around 1 S/cm. In general, pristine PEDOT:PSS yields conductivities in the range of 0.1 ~ 10 S/cm,[82] whereas solvent added films show a large increase in conductivities.[85, 96, 157] In our experiment, the conductivities remarkably increase to around 700 S/cm by the addition of EG. The highest conductivity of 735 S/cm is obtained for the films with EG concentration of 6 vol.%. For films with an EG concentration higher than 4 vol.%, the conductivities remain nearly constant above 700 S/cm. It is observed that with increasing concentration of EG from 0 to 10 vol.%, the surface root-mean-square roughness of films increased gradually from 1.37 to 2.02 nm (1×1 μm^2). The observed effects of solvents on PEDOT:PSS films, i. e. drastic improvement of conductivities, saturation of conductivities at a certain concentration, and increasing roughness with the addition of more solvent, are well consistent with results from literature.[87, 157]

Having optimized the conductivities of films with respect to the solvent addition to the liquid formulation, the influence of solvent post-treatment on dry layers is investigated. Spin-coated and annealed thin films from 6 vol.% EG solutions are immersed into an EG bath for several minutes and dried afterwards. As a result, the conductivities significantly increase, as shown in **Fig. 5.2 (b)**. Without solvent post-treatment, such films show a conductivity of 731 S/cm, which increase gradually with increasing post-treatment time. The highest conductivity of 1418 S/cm is obtained at a solvent post-treatment time of 30 min. However, extended post-treatment time of more than two hours yield somewhat reduced conductivities. The PEDOT:PSS films with solvent post-treatment times of 0, 1, 5, 10, 15, and 30 minutes show sheet resistances of 412, 285, 335, 349, 448, and 470 ohm/sq, respectively. It is interesting to note that the film thickness decreases from 33 to 15 nm with increasing solvent post-treatment time, whereas the transmittance remains at almost the same level of around 89.5 % even in the thinner films. The optical absorption of PEDOT:PSS in the visible range is mainly determined by the amount of PEDOT since PSS is almost colorless. The combined results of improved conductivity, reduced thickness, and constant transmittance, therefore, indicate that insulating PSS is removed from PEDOT:PSS films during solvent post-treatment. Together with the well-known reordering and conformational changes of the PEDOT:PSS polymer chains upon exposure to high boiling point solvents, mixed with the solvent or treated in the solvent bath, as reported by Ouyang et al.,[95] the removal of PSS is the prime reason for the improved conductivity observed in our experiments. To further clarify these mechanisms, more experiments have been conducted.
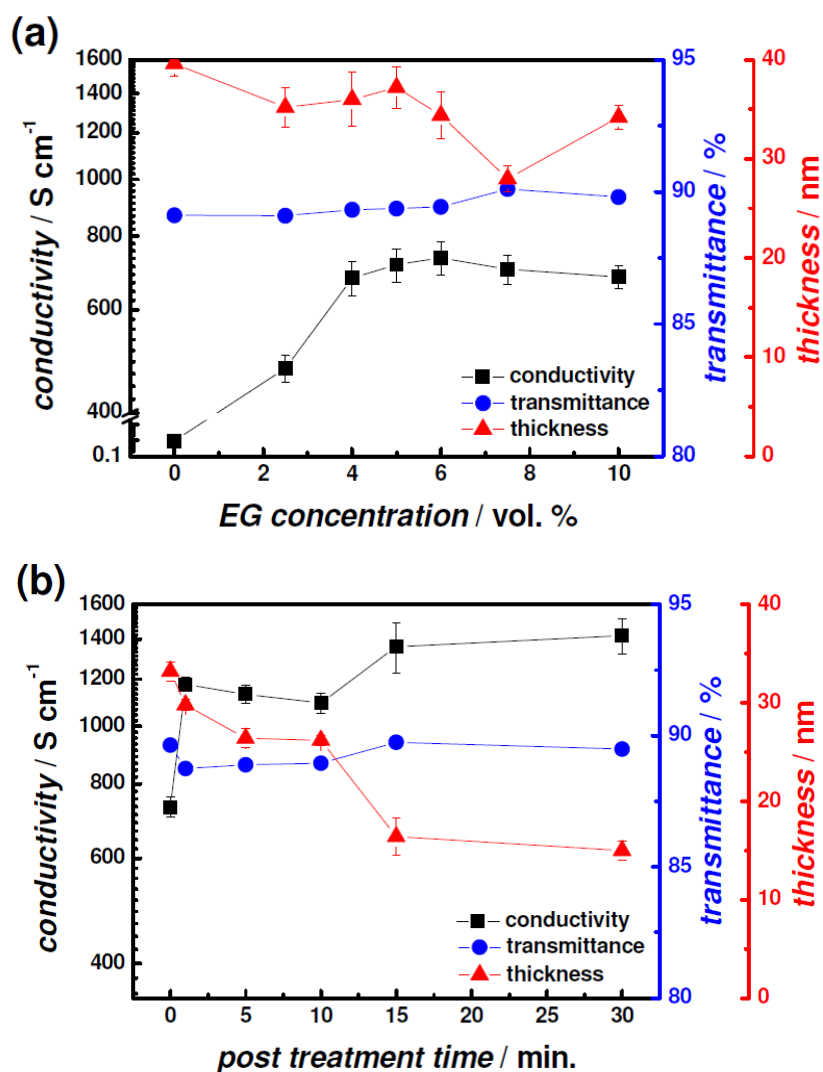
62

Figure 5.2. *Variations of the conductivity, transmittance and film thickness of PEDOT:PSS films with respect to (a) EG concentration and (b) solvent post-treatment time (for EG 6 vol.% doped PEDOT:PSS). The error bars represent the standard deviation from several measurements.*

To support our results from thin PEDOT:PSS films, we study thicker films, which behave similar, as shown in **Fig. 5.3**. The observations for thicker films agree with those for thinner films. A loss in thickness, together with a gain in conductivity is observed with increasing solvent post-treatment time. For the thicker films the transmission does not stay constant, as for thinner films, probably indicating some removal or rearrangement of PEDOT together with the PSS.
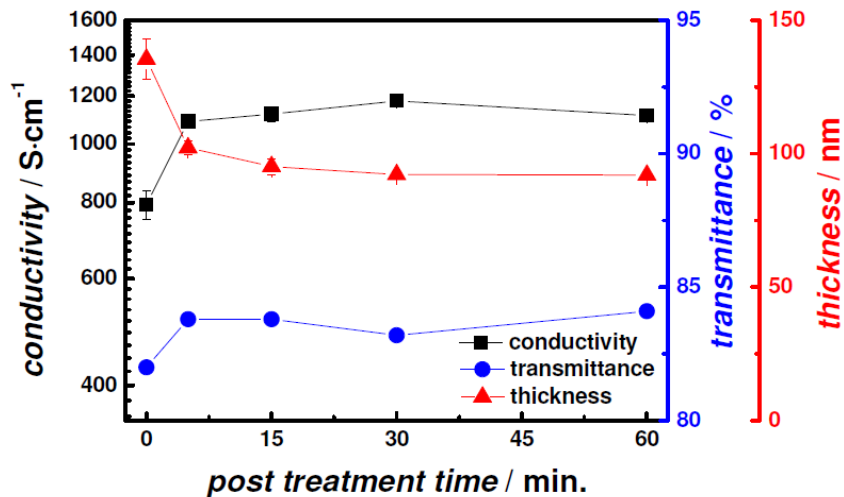
Figure 5.3. The conductivities, transmittances, and thicknesses of a thicker PEDOT:PSS film, initial thickness 135 nm, as a function of solvent post-treatment time.

The topography and current AFM images of the pristine and 6 vol.% EG added PEDOT:PSS film with solvent post-treatment are shown in **Fig. 5.4**. It is shown that the current distribution in EG added post-treated conductive film is more uniform and larger than the pristine film, indicating the highly enhanced conductivity of PEDOT:PSS film by the solvent treatment.
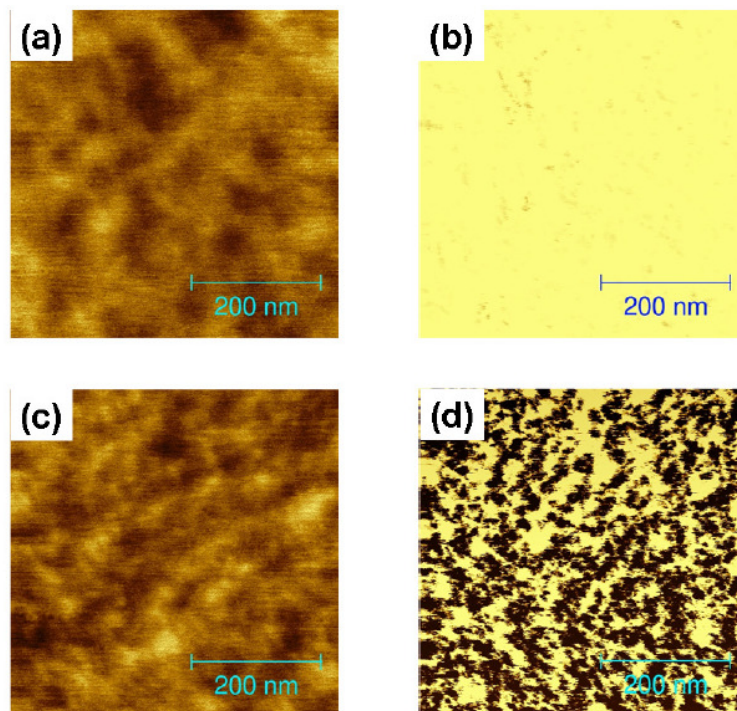

Figure 5.4. AFM images of topography (left) and current (right) for PEDOT:PSS films. (a, b) pristine PEDOT:PSS and (c, d) post-treated PEDOT:PSS with EG 6 vol.%.

Figure 5.5 shows AFM phase images of PEDOT:PSS films with different solvent treatments. Clear structural changes are observed in phase images with improved conductance. In **Fig. 5.5 (a)**, the pristine PEDOT:PSS film which has low conductivity shows a typical phase image of PEDOT:PSS films, meaning that the bright (positive) and dark (negative) phase shifts correspond to PEDOT-rich grains and PSS-rich grains, respectively.[158-160] We observe that pristine films consist of disconnected, conducting PEDOT-rich grains with weak phase separation, whereas solvent added PEDOT:PSS films, PH510 with 5 vol.% DMSO (**Fig. 5.5 (b)**, σ = 389 S/cm), and PH1000 with 6 vol.% EG (**Figure 5.5 (c)**, σ = 634 S/cm) having moderate conductivities, reveal better connection of PEDOT-rich grains and fairly well defined phase separation. On the other hand, the solvent post-treated PEDOT:PSS film which has the highest conductivity (1330 S/cm) in the series shows different structural properties compared to other films of lower conductivity. It is shown that the solvent post-treatment transforms the shape of PEDOT-rich grains from short curved domains to a long stretched network. These results suggest that the depletion of insulating PSS develops the compact thin film structure as well as the conducting PEDOT-rich granular networks, which cause larger contact areas between better oriented PEDOT-rich grains, resulting in the improvement of conductivity by enhanced conducting pathways for carriers.

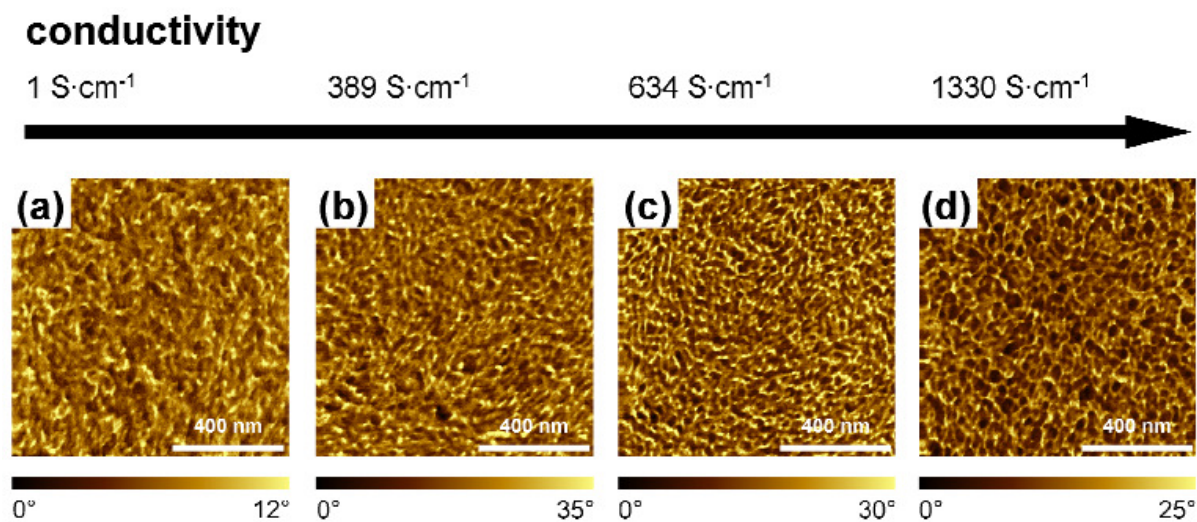*Figure 5.5. AFM phase images of PEDOT:PSS films with various solvent treatments. (a) pristine PEDOT:PSS (PH1000) (σ < 1 S/cm), (b) PEDOT:PSS (PH510) doped with DMSO 5 vol.% (σ = 389 S/cm), (c) PEDOT:PSS (PH1000) doped with EG 6 vol.% (σ = 634 S/cm) (d) solvent post-treated PEDOT:PSS (PH1000) doped with EG 6 vol.% (σ = 1330 S/cm).*

The assumption of PSS depletion by solvent post-treatment is supported by the following experiments. It is well known that the strongly acidic PSS is very hygroscopic and takes up water easily, leading to severe deterioration of conductivity as well as stability of organic devices with PEDOT:PSS electrodes.[59, 161] To investigate the effect on removal of PSS in PEDOT:PSS films, the stability of the conductivity is examined in ambient atmosphere. In **Fig. 5.6 (a)**, the evolution of sheet resistances for 6 vol.% EG added PEDOT:PSS films with solvent post-treatment times of 0, 1, 5, and 30 minutes is measured as a function of air exposure time. The air exposure causes a gradual increase in sheet resistance for all the films due to water absorption from atmosphere. The film without solvent post-treatment shows the fastest increase in sheet resistance as compared to the other post-treated films. The film with the longest solvent post-treatment time of 30 min shows the best stability against air exposure, indicating that the depletion of PSS in the layer causes minimization of water absorption. In addition, a more compact structure of PEDOT:PSS induced by the depletion of PSS as well as the rearrangement of the polymer further enhances the conductivity and the humidity stability.[162] **Figure 5.6 (b)** shows XPS spectra for PEDOT:PSS films containing 6 vol.% EG with and without the solvent post-treatment. Typical S(2p) peaks are observed in both films at the binding energy of 167.6 and 163.9 eV, which correspond to the sulfur signals from the sulfonate and thiophene of PSS and PEDOT, respectively.[157] The calculated surface ratio of PSS to PEDOT for the film with and without solvent post-treatment is 1.37 : 1 and 2.15 : 1, respectively, showing remarkably reduced PSS by 36 % as a result of the post-treatment.
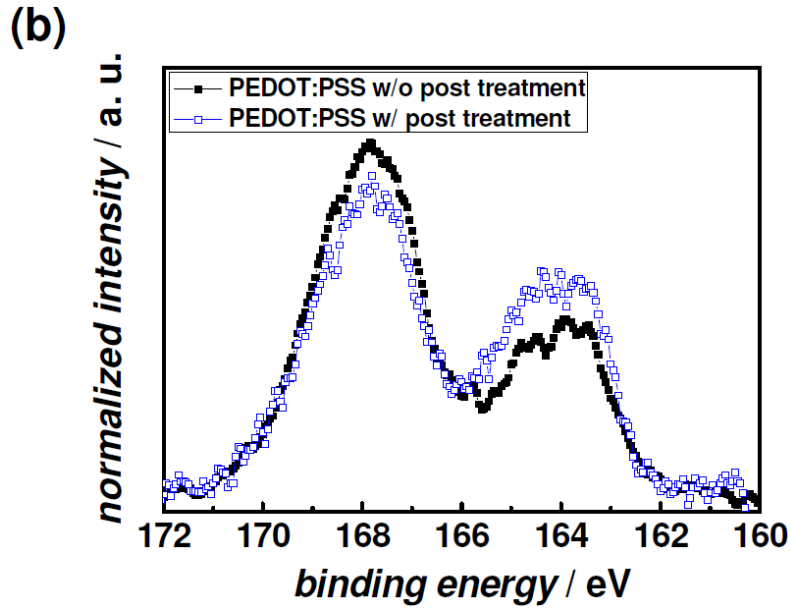
(b)
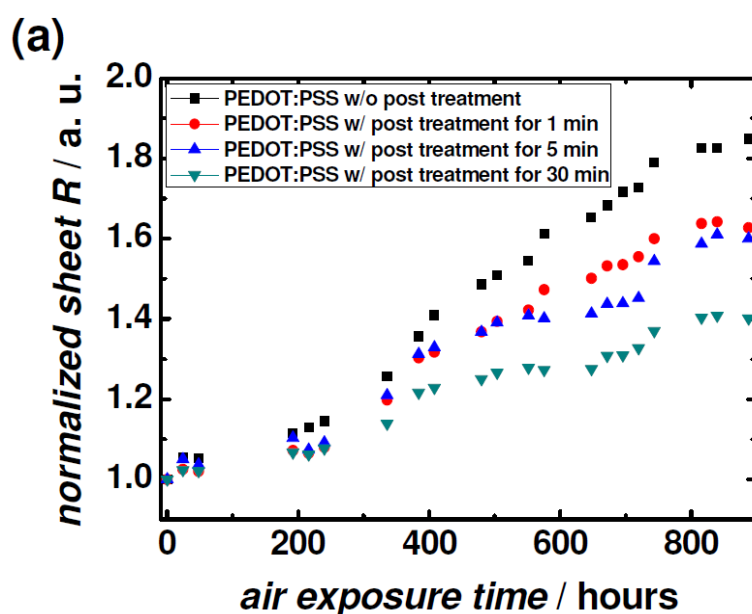
Figure 5.6. (a) Variations of the sheet resistance (sheet R) of PEDOT:PSS films with different solvent post-treatment times as a function of air exposure time. (b) The XPS S(2p) spectra of PEDOT:PSS films with and without the solvent post-treatment.

In **Fig. 5.7**, the effect of solvent post-treatment on the absorption spectra of PEDOT:PSS is shown. An almost constant absorption is observed in the visible region regardless of solvent post-treatment, denoting that the post-treatment hardly leads to removal of PEDOT. In the ultraviolet region, a large change in the strong absorption peaks at the wavelength of 225 nm, attributed the substituted phenyl groups in the PSS is observed.[163-166] In both the thinner and thicker PEDOT:PSS films, the solvent post-treated films show reduced PSS ratio compared to the film without post-treatment, indicating the depletion of PSS in a bulk region.

DeLongchamp et al. reported the removal of PSS from PEDOT:PSS films by post water rinse treatment and calculated the relative amount of washed PSS by using the Beer-Lambert law with the absorption spectra of films in the infrared region.[167] The PEDOT composition was extracted by following Beer-Lambert equation with linear dependence of PEDOT absorption with respect to film thickness.

$$A(\lambda) = \varepsilon(\lambda)tc \tag{1}$$

where A is the absorption, ε the molar absorptivity, t the film thickness, and C is the concentration, respectively. They showed that the water-rinsing removed PSS by 40 ~ 50 % with negligible PEDOT loss. We calculate the relative amount of depleted PSS ratio in the same way, showing that the 47 % of PSS is depleted as a result of solvent post-treatment. The

depleted PSS ratio in bulk region is higher than surface region, observed by XPS results (36 %).
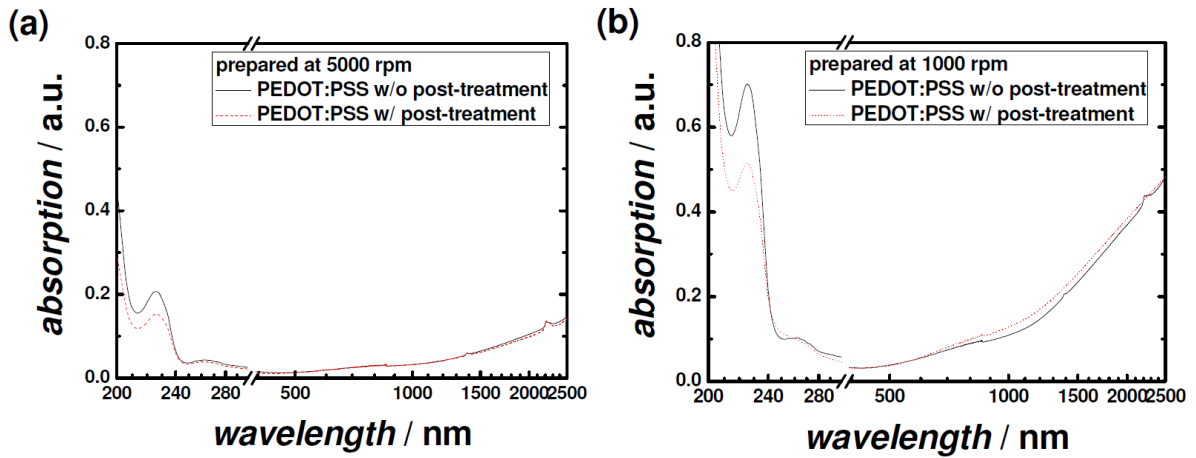

Figure 5.7. *The absorption spectra of (a) thinner and (b) thicker EG 6 vol.% doped PEDOT:PSS films with and without post-treatment.*

To optimize the solvent post-treated PEDOT:PSS for application in solar cells, a multilayer coating is investigated to further lower the sheet resistance of the films. **Figure 5.8** shows the behavior of transmittance and sheet resistance for solvent post-treated PEDOT:PSS films controlled by different spin-coating speed, number of layers, and solvent post-treatment time. The electrical and optical properties of post-treated PEDOT:PSS films distinctly depend on the film thickness regardless of various deposition parameters. The relationship between transmittance and sheet resistance for transparent electrodes is represented by the following equation:[168]

$$T = \left(1 + \frac{Z_0}{2R_S} \frac{\sigma_{Op}}{\sigma_{dc}} \right)^{-2} \tag{2}$$

where T is the transmittance, R_S the sheet resistance, Z_0 (377 ohm) the impedance of free space, and σ_{Op} and σ_{dc} indicate the optical and dc conductivities, respectively. The experimental data from all solvent post-treated PEDOT:PSS films are fitted quite well, giving a value of σ_{dc}/σ_{Op} = 36.3, being considered sufficient for transparent electrode applications.[168] This fit has the advantage of being independent of the error-prone thickness measurement, and is quite accurate for a large thickness range (**Fig. 5.9**). Thereby, it shows that the solvent post-treatment affects the whole thin-film and is not entirely focused on the surface. The solvent post-treated PEDOT:PSS films exhibit promising sheet resistance and transmittance values in the range of 65 ~ 176 ohm/sq and 80 ~ 88 %, respectively, showing

68

that with ever increasing performance, conductive polymers are an alternative to ITO as an electrode for organic solar cells.
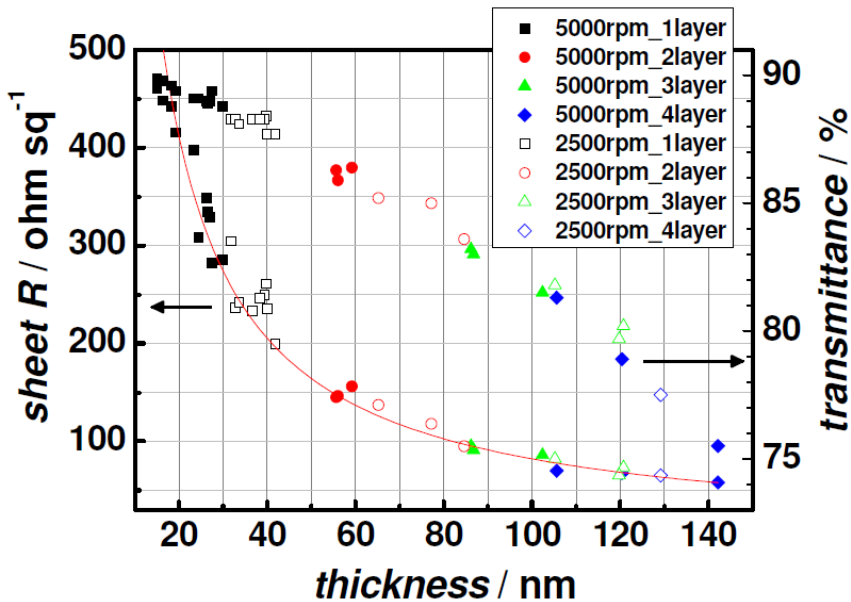
Figure 5.8. *Transmittance and sheet resistance for solvent post-treated PEDOT:PSS films as a function of the film thickness, controlled by different spin-coating speed, number of layers and solvent post-treatment time. The red line is fitted to sheet $R = R_0/thickness$, giving a value of $R_0 = 8214$, showing a good fit over the whole thickness range.*
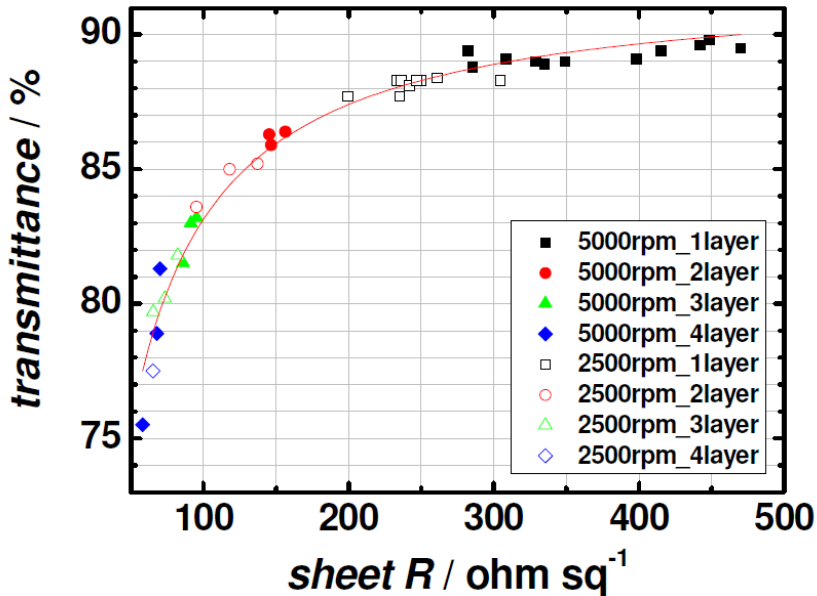
Figure 5.9. *The transmittance and sheet resistance behavior of PEDOT:PSS films, replotted from Fig. 5.8, fitting formula (2) and showing a good fit over the whole observed thickness range.*

In summary, we have prepared highly conductive, transparent PEDOT:PSS films for use as an electrode in organic solar cells. By the addition of solvent, the conductivity of the thin-films increases, and by the additional solvent post-treatment method, the conductivity increases further attributed to the removal of PSS from the PEDOT:PSS layer. The highest conductivity of 1418 S/cm has been obtained for a single layer PEDOT:PSS film. For thicker multi-layered PEDOT:PSS films, low sheet resistances (< 65 ohm/sq) with high transparencies (> 80 %) have been achieved.

5.3. Application in OPV cells

Optimized solvent post-treated PEDOT:PSS films are adopted as an electrode for ITO-free organic solar cells. A pre-heating treatment of the PEDOT:PSS electrode is performed to improve the efficiency of solar cells.

5.3.1. Thermal treatment of PEDOT:PSS

- Fabrication of OPV cells

To remove residual water from the PEDOT:PSS electrode, solar cells on glass and PET substrates are heated for 120 min in the vacuum chamber at 145 °C and 125 °C, respectively, just before evaporation of organic layers. The layer sequence used for the solar cells is as follows (bottom to top) : ITO or PEDOT anode / 1 nm, 2,2'-(perfluoronaphthalene-2,6-diylidene)dimalononitrile (F6TCNNQ) as a hole injection layer / 50 nm, 10 wt.% F6TCNNQ doped N,N'-((Diphenyl-N,N'-bis)9,9,-dimethyl-fluoren-2-yl)-benzidine (BF-DPB) as a hole transport layer / 30 nm, mixed zinc phthalocyanine (ZnPc) : fullerene C_{60} (ratio of 1 : 2) as an absorber layer / 30 nm, C_{60} as an additional absorber and electron transport layer / 6 nm, 4,7-diphenyl-1,10-phenanthroline (BPhen) as an exciton blocking layer / 100 nm, Al as a cathode. The device areas of solar cells are 5.2 ~ 6.4 mm^2 (differences are attributed to different electrode patterning methods used) measured using an optical microscope. The values of short circuit current are normalized to 100 mW/cm^2 and are not corrected for spectral mismatch. The ageing experiments are carried out by a self-made setup. Devices are heated to ~ 50 °C and illuminated by white LEDs (Philipps Lumileds, LUXEON LXK2-PWC4-0220, with a continuous emission spectrum from 400 to 700 nm).

- Results

Having investigated highly conductive PEDOT:PSS films obtained by solvent post-treatment, small molecule organic solar cells are built on these electrode films. The cell utilized a p-i-n structure with a bulk heterojunction absorber layer composed of ZnPc : C_{60}, commonly used in small molecule organic solar cells, as shown in **Fig. 5.10 (a)**. The photo current density (J_{SC}) and applied voltage (V_{OC}) characteristics for solar cells with ITO as a reference cell and PEDOT:PSS electrodes are shown in **Fig. 5.10 (b)**. The characteristics of the solar cells are summarized in **Table 5.1**. The solar cell with ITO on glass produces a power conversion efficiency (PCE) of 2.55 %, a comparably high value to efficiencies reported for ZnPc : C_{60} bulk heterojunction organic solar cells in literature,[169] denoting that it represents an excellent reference for comparison with a PEDOT:PSS electrode. The solar cell with PEDOT:PSS on glass exhibits lower PCE of 2 % and fill factor (FF) of 47.1 % as compared with those of solar cell with ITO (with PCE of 2.55 % and FF of 59.4 %) caused by higher series resistance.

As mentioned above, PEDOT:PSS is very hygroscopic and its tendency to uptake water causes significant loss of conductivity. This factor is also expected to influence the performance of solar cells, with residual water in the PEDOT:PSS film diffusing into the active layer as well as causing a higher contact resistance between the PEDOT:PSS layer and the hole transport layer.[59, 161, 170] To remove the residual water in the PEDOT:PSS electrode, the electrode is heated in the vacuum chamber before evaporation. The pre-heated electrode is kept in the high vacuum under 10^{-8} mbar in the whole process of solar cell fabrication, ensuring that most of the water is removed from the PEDOT:PSS. The solar cell with pre-heated PEDOT:PSS on glass shows an improvement of the PCE from 2 % to 2.54 % with the increased FF of 57.7 %. Also, a high efficiency of 1.95 % has been obtained for a flexible solar cell with pre-heated PEDOT:PSS electrode on PET. These improvements are mainly attributed to the removal of water from the PEDOT:PSS electrode, showing a reduction of the series resistance of the solar cell with pre-heating treatment. The series resistance of the solar cell with PEDOT:PSS on glass decreases from 30.4 to 16.4 ohm cm^2 by pre-heating treatment of the electrode. It is also expected that water removal by pre-heating enhances the long term stability of the solar cells. The variations of FF and PCE of solar cells as a function of illumination intensity are presented in **Fig. 5.10 (c)**. The unheated PEDOT:PSS cell shows an increasing FF and PCE with decreasing illumination intensity while those of the ITO solar cell remains at a constant level. This indicates the importance of a low series resistance for high illumination intensities and a relative performance increase for cells on less conductive

electrodes in reduced light environments. The pre-heated PEDOT:PSS cell shows similar behavior of FF and PCE to the ITO cell, because of the reduced series resistance as well as probably a lower hole extraction barrier.[171] These results suggest that the pre-heating treatment of PEDOT:PSS electrodes can produce cells with a comparable PCE to that of an ITO-based cell.
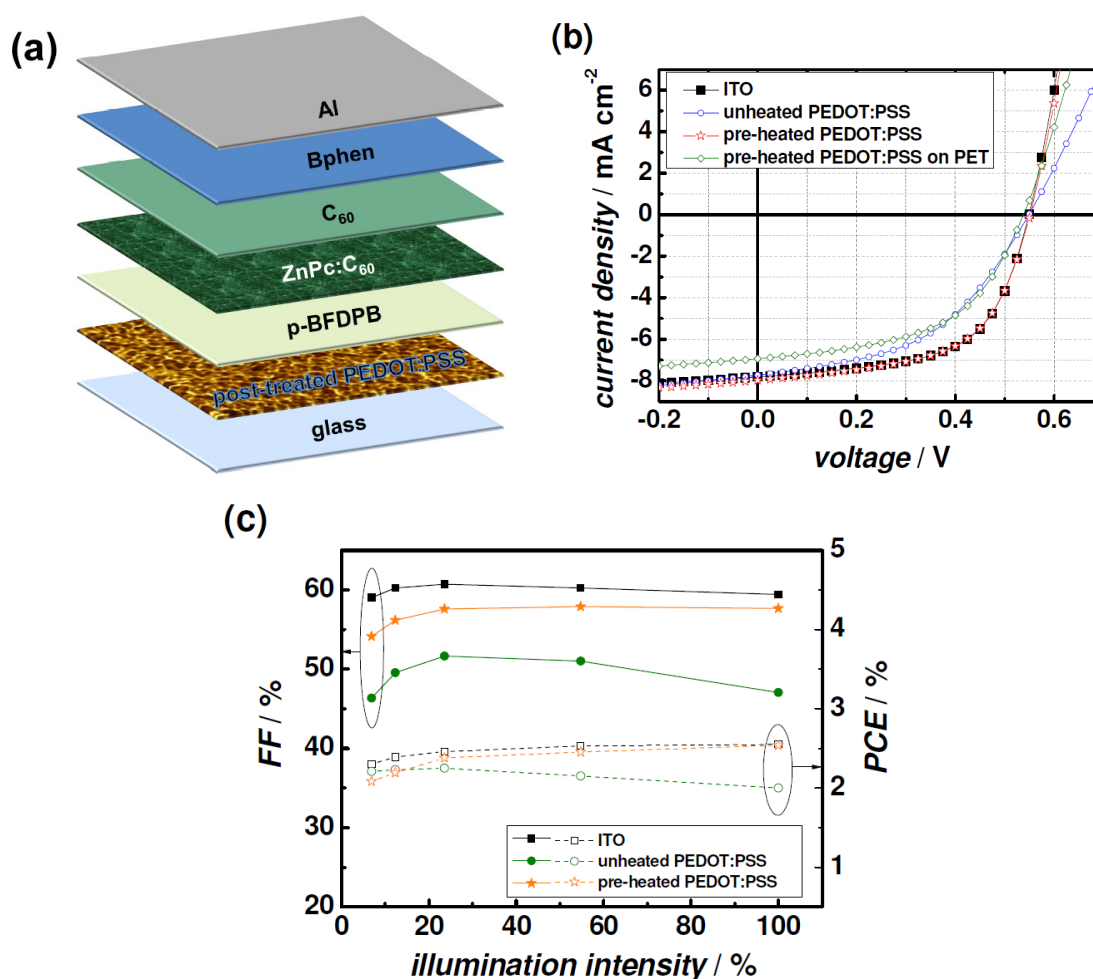
Figure 5.10. (a) The structure of p-i-n small molecule organic solar cell with ZnPc:C$_{60}$ bulk heterojunction concept. (b) Current density vs voltage characteristics for solar cells with ITO, unheated PEDOT:PSS and pre-heated PEDOT:PSS electrode under 100 mW/cm^2 AM 1.5G illumination. (c) Variations of fill factor and PCE of solar cells with ITO, unheated PEDOT:PSS and pre-heated PEDOT:PSS electrode with respect to illumination intensities.

Rowell et al. calculated the dependence of cell area and a power loss of organic solar cells caused by the sheet resistance of electrode.[113]

$$P_{loss} = \frac{(jlw)^2 R_s w}{3l}$$

(3)

where P_{loss} is the power loss, j the short current density, l the length of area, R_S the sheet resistance of electrode, and w is the width of area, respectively. It is expected that a cell, based on a PEDOT:PSS electrode (sheet resistance of PEDOT:PSS electrode < 100 ohm/sq) with a square area not exceeding 20 mm^2, does not show a power loss of more than 10 %. However, for large area cells, the PEDOT:PSS electrode still needs to be combined with grid structures.

	V_{OC} [V]	J_{SC} [mA/cm^2]	FF [%]	PCE [%]	Series R [ohm cm^2]
ITO on glass	0.55	7.81	59.4	2.55	14.5
unheated PEDOT:PSS on glass	0.55	7.73	47.1	2.00	30.4
pre-heated PEDOT:PSS on glass	0.55	7.98	57.7	2.54	16.4
pre-heated PEDOT:PSS on PET	0.54	6.94	52.2	1.95	25.5

Table 5.1. The performances of small molecule organic solar cells with different anodes, which are measured under an AM 1.5G illumination and corrected to 100 mW/cm^2.

In summary, based on this highly conductive PEDOT:PSS, ITO-free, small molecule organic solar cells have been produced on the PEDOT:PSS electrode on glass and PET substrates and achieved excellent PCEs of 2.54 % and 1.95 %, respectively. The removal of residual water in the PEDOT:PSS film by substrate pre-heating has remarkably enhanced the performance of solar cells. The results indicate that PEDOT:PSS films with highly enhanced conductivity and stability by solvent and heating treatment could serve as a promising transparent electrode for low-cost and flexible ITO-free organic solar cells.

5.3.2. Enhancement of efficiency and lifetime in OPV cells

In this work, the effect of post-treated PEDOT:PSS on the lifetime of OPV cells is investigated. The post-treatment does not only improve the conductivity of PEDOT:PSS, but also significantly enhances the lifetime and the efficiency of OPV cells.

- Fabrication of OPV cells

The layer sequence for devices is as follows (bottom to top): PEDOT:PSS as a bottom electrode / 1 nm 2,2'-(perfluoronaphthalene-2,6-diylidene)dimalononitrile (F6TCNNQ) as a hole injection layer / 50 nm 5 or 10 wt.% F6TCNNQ doped hole transport layer (HTL) / 30 nm mixed zinc phthalocyanine (ZnPc) : fullerene C_{60} (ratio of 1 : 2) as an absorber layer / 40 nm C_{60} as an additional absorber layer / 6 nm BPhen as an exciton blocking layer / 100 nm Al as a top electrode. MeO-TPD (N,N,N',N'-tetrakis(4-methoxyphenyl)-benzidine), BF-DPB (N,N'-((diphenyl-N,N'-bis)9,9,-dimethyl- fluoren-2-yl)-benzidine), and Di-NPD (N,N'-diphenyl-N,N'-bis(4'-(N,N-bis(naphth-1-yl)-amino)-biphenyl-4-yl)- benzidine), are used as HTLs. After evaporation, all devices are encapsulated with cover glass using epoxy glue and additionally getter material is placed in the cover glass cavity. The active areas are 6.7 ~ 7.6 mm^2, measured using an optical microscope.

- Results

OPV cells with different types of HTL layers are prepared to investigate the influence of the post-treatment on the PEDOT:PSS/HTL interface as well as device performances. **Figure 5.11** shows the typical *I-V* curves of solar cells with PEDOT:PSS electrodes (PEDOT_OPV cells) having an HTL of Di-NPD with solvent post-treated and untreated electrodes. The highest PCE of 2.7 % is observed in the device with Di-NPD accompanied by the post-treatment. Devices with MeO-TPD and BF-DPB show a PCE of around 2.6 % (see **Fig. 5.12**). The highest occupied molecular orbital (HOMO) levels of MeO-TPD, BF-DPB, and Di-NPD are 5.1 eV, 5.25 eV, and 5.35 eV, respectively (measured by UPS).[172] The p-doping of the HTL shifts the Fermi energy level closer towards the HOMO level of the HTL.[6] Considering these effects, charge injection and extraction barriers are minimized at the PEDOT:PSS (work function : ~ 5.1 eV, as measured by UPS) and HTL interfaces. It is notable that the post-treatment improves J_{SC} for all solar cells, especially for the device with Di-NPD. The J_{SC} increases from 7.5 to 8.3 mA/cm^2 and the FF increases from 55.4 to 56.7 % as well as PCE from 2.4 to 2.7 %. Similar devices which have an additional 5 nm thick layer of 25 wt.% F6TCNNQ doped Di-NPD between PEDOT:PSS and HTL (5 wt.% F6TCNNQ doped Di-NPD), to observe the influence of interface doping, show similarly enhanced J_{SC} and PCE on the post-treated electrodes (untreated device : J_{SC} of 7.6 mA/cm^2, PCE of 2.3 %, post-treated device : J_{SC} of 8.3 mA/cm^2, PCE of 2.7 %), as shown in **Fig. 5.11**. For both types, the reference devices with untreated PEDOT:PSS, have almost the same transmittance in the visible region as those with post-treated electrodes, indicating similar incident photon rates on

74

the absorber layer. Injection or extraction barriers at the interface of PEDOT:PSS/doped HTL are low enough for good carrier transport. Considering these points, the improvement of J_{SC}, together with the increase of FF, is likely to be caused by the removal of PSS from the PEDOT:PSS surface, which is known to be PSS rich, and bulk region, being able to collect more photo-generated carriers by eliminating insulating PSS which hinders the carrier extraction at the interface of PEDOT:PSS/HTL electrode.
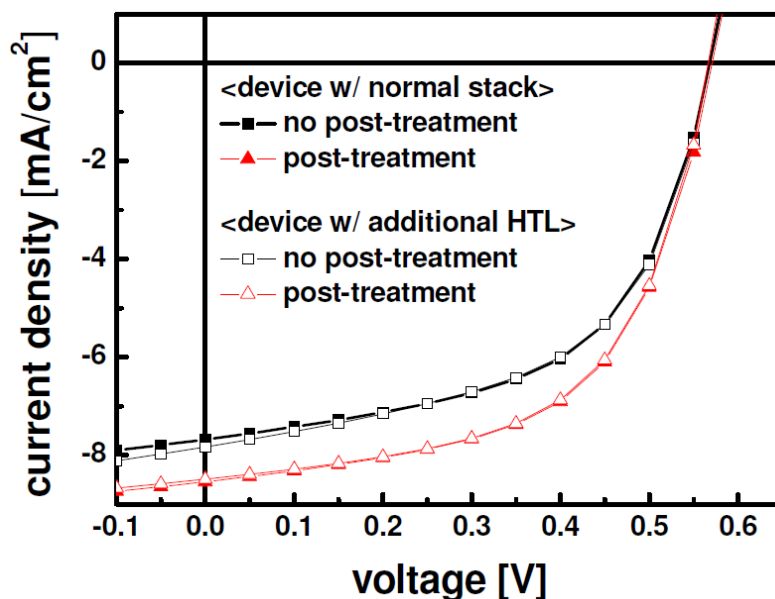
Figure 5.11. *I-V curves of OPV cells with the HTL of Di-NPD fabricated on the PEDOT:PSS electrodes (full symbols) with and without solvent post-treatment. Devices with the additional highly p-doped Di-NPD layer between the PEDOT:PSS and the Di-NPD (open symbols).*
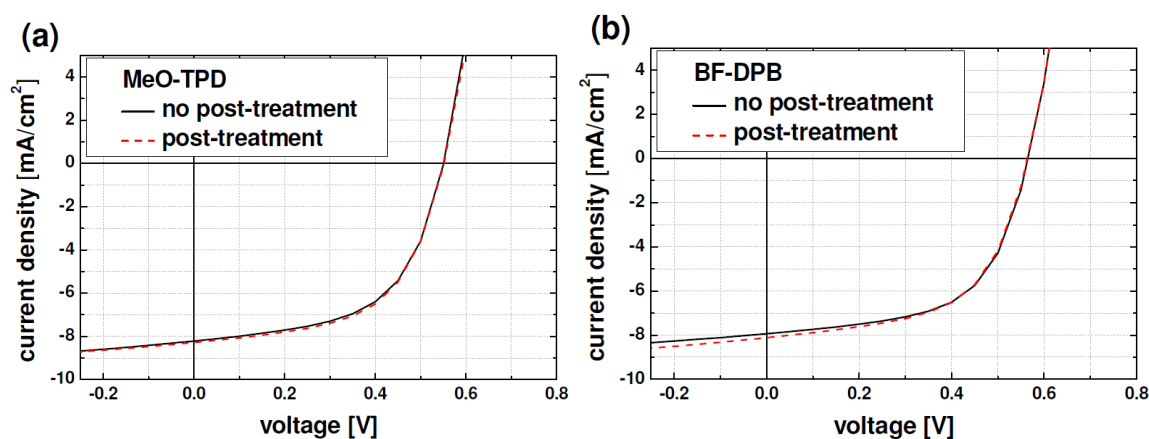

Figure 5.12. *I-V curves of OPV cells with the HTL of (a) MeO-TPD and (b) BF-DPB fabricated on the PEDOT:PSS electrodes with and without the solvent post-treatment.*

To investigate the effect of the solvent post-treatment on the lifetime of the devices, ageing measurements are carried out for selected devices. **Figure 5.13 (a)** shows the *I-V* curves of PEDOT_OPV cells having the HTL of MeO-TPD with and without solvent post-treatment of electrodes under 5 suns over 1000 hours, showing the degradation behavior over time. Normalized power outputs at maximum power point are plotted in **Fig. 5.13 (b)**. After 600 hours, the untreated device shows a larger power decay compared to the post-treated device, indicating that power loss due to the increase of series resistance with ageing is more significant for the untreated device.
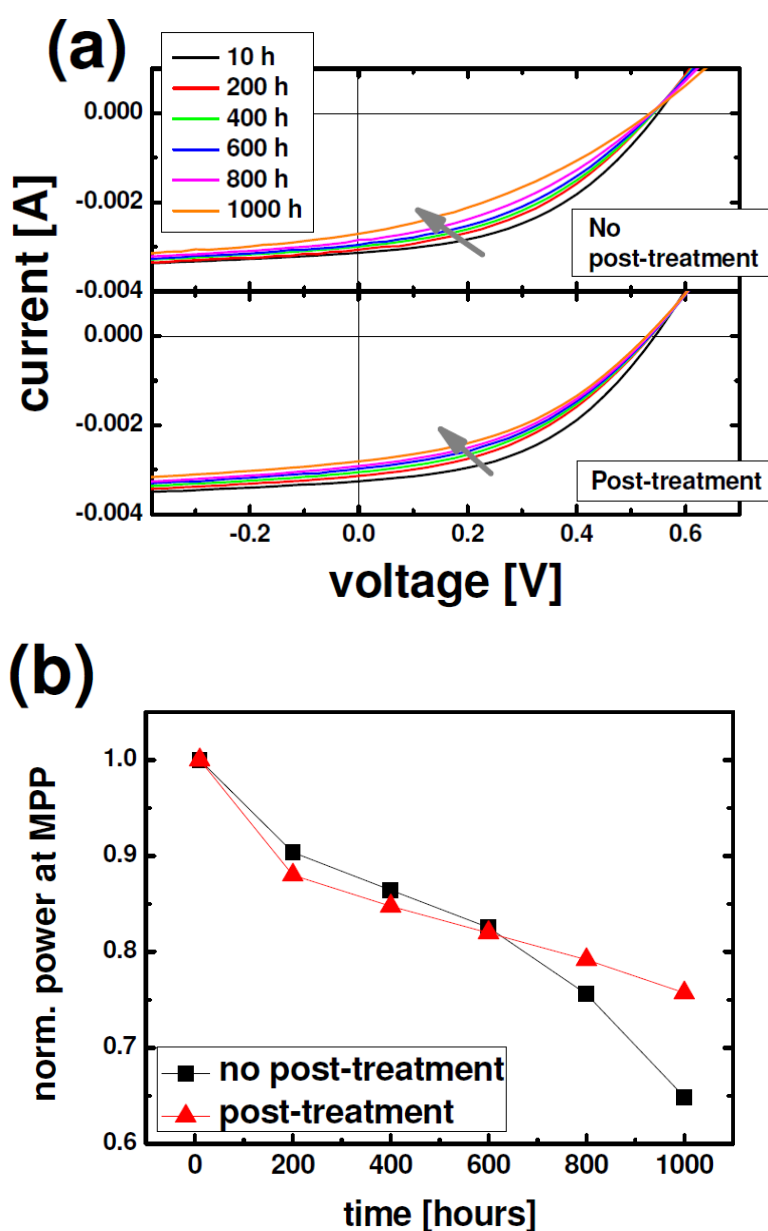

Figure 5.13. *(a) I-V curves and (b) normalized power at a maximum power point (MPP) of OPV cells having the HTL of MeO-TPD on the PEDOT:PSS electrodes with and without the*

post-treatment. The encapsulated devices are heated up to ~ 50 °C and illuminated by white LEDs equivalent to 5 suns.

Figure 5.14 shows the behavior of normalized PCE, FF, J_{SC}, and V_{OC} for OPV cells in the ageing experiment. The devices are illuminated with an intensity of 3 or 5 suns to accelerate ageing speed. All parameters of devices decrease over time, showing different ageing speeds. The device with the ITO electrode shows a normalized efficiency decay of ~ 3.5 % over 800 hours under 3 suns with almost stable FF, but a decrease of J_{SC} and V_{OC}. The PEDOT_OPV cells having an HTL of BF-DPB without the solvent post-treatment show a PCE decay of 17 %, after ~ 800 hours under 3 suns. With the solvent post-treatment, the stability of the PEDOT_OPV cells is improved, showing a PCE decay of only 9 %. It is shown that the main factor of different ageing behavior in this experiment is the difference rate of the FF decay. Both solar cells show similar trends in loss of J_{SC} and V_{OC}. The device with solvent post-treated PEDOT:PSS is more resistant against FF decay compared to the untreated device. The post-treated device shows a FF decay of only 5 %. In contrast, the FF decay of the untreated device is about 11 % after ~800 hours under 3 suns.
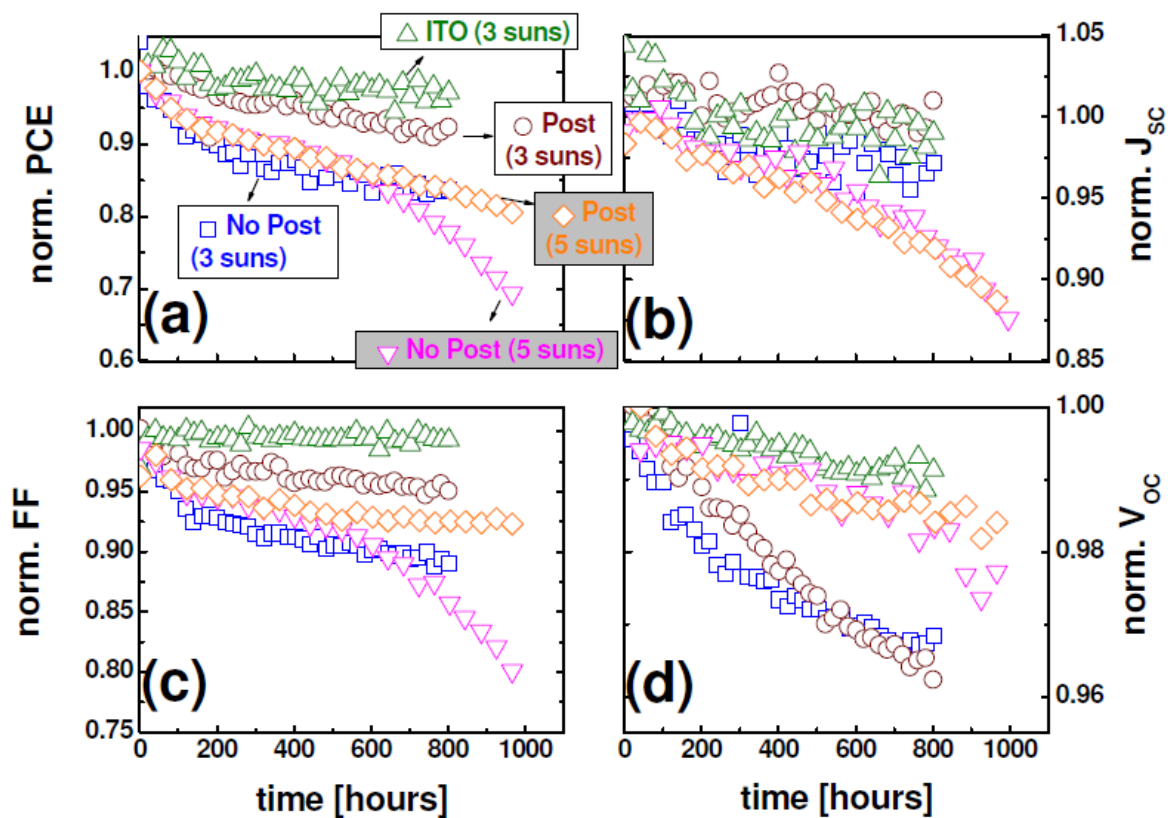
Figure 5.14. Ageing characteristics of solar cells with ITO or PEDOT:PSS electrodes treated with and without the solvent post-treatment. The encapsulated devices are heated up to ~ 50 °C and illuminated by white LEDs equivalent to 3 suns or 5 suns. All devices aged at 3 suns have BF-DPB as HTL, the devices aged 5 suns employ a Meo-TPD HTL.

We increase the illumination intensity equivalent up to 5 suns for the PEDOT_OPV cells with the HTL of MeO-TPD. The untreated device shows a PCE and FF decay of 33 % and 22 %, respectively, after 1000 hours. In contrast, the PEDOT_OPV cells with post-treatment shows a remarkably enhanced stability compared to the untreated device, showing a PCE and FF decay of only 20 % and 8 %, respectively. Both PEDOT_OPV cells with and without the post-treatment show a rather similar decrease of J_{SC} and V_{OC}. Some difference in the degradation behavior between the different HTLs and ageing conditions can be observed, but the influence of the post-treatment process is large and clear for both HTLs and ageing conditions. The improved stability for the post-treated samples can be well explained by the influence of PSS which has a hygroscopic and acidic nature. The PSS depleted samples by solvent post-treatment minimize the residual water in the electrode and decrease its acidity. As a result, water and PSS migration to the organic absorber layer are suppressed and the chemical stability is improved. Therefore device degradation is slowed down or hindered.

	V_{OC} [V]	J_{SC} [mA/cm^2]	FF [%]	PCE [%]
no post-treatment				
Di-NPD	0.57	7.5	55.4	2.4
Di-NPD with additional HTL	0.57	7.6	54.1	2.3
post-treatment				
Di-NPD	0.57	8.3	56.7	2.7
Di-NPD with additional HTL	0.57	8.3	57.2	2.7

Table 5.2. Performance parameters of PEDOT_OPV cells with an HTL of Di-NPD with and without solvent post-treatment of the electrodes.

In summary, we have demonstrated efficient ITO-free OPV cells with optimized PEDOT:PSS polymer electrodes and improved lifetimes. The OPV cells with PEDOT:PSS electrodes show

an improvement of J_{SC} and PCE by the solvent post-treatment almost independent of the HTL materials used. In addition, the post-treatment considerably improves the lifetime of devices with a strong reduction in FF decay. These results indicate that the solvent post-treatment for PEDOT:PSS electrodes is a very promising method for the development of low cost and stable ITO-free solar cells.

5.4. Application in transparent OLEDs

Here, we report high efficiency ITO-free transparent OLEDs based on PEDOT:PSS electrodes. By tuning the thickness of the hole transport layer and the PEDOT:PSS electrode, the OLED performance is carefully optimized in terms of efficiency, long-term stability and transmittance of PEDOT:PSS-based devices.

- Fabrication of OLEDs

For removal of residual water in the PEDOT:PSS (PH1000 + EG 6 vol.%) electrode, the prepared PEDOT:PSS films are thermally annealed at 110 °C for 30 min in a vacuum chamber directly before evaporation of organic materials. The layer sequence for devices is as follows (bottom to top): glass / ITO or PEDOT:PSS / X nm (N,N,N',N'-tetrakis(4-methoxyphenyl)-benzidine) (MeO-TPD) : 2,2'-(perfluoronaphthalene-2,6-diylidene)dimalononitrile (F6TCNNQ) (4 wt.%) / 10 nm 2,2',7,7'-tetrakis-(N,N'-diphenylamino)-9,9'-spirobifluorene (Spiro-TAD) / 20 nm N,N'-di(naphthalene-1-yl)N,N'-diphenyl-benzidine (NPB) : Iridium(III)bis(2-methyldibenzo-[f,h]chinoxalin)(acetylacetonat) (Ir(MDQ)2(acac)) (10 wt.%) / 10 nm bis(2-methyl-8-chinolinolato)-4-(phenyl-phenolato)-Aluminum-(III) (Balq$_2$) / 60 nm 4,7-diphenyl-1,10-phenanthroline (BPhen) : Cs (1:1) / 15 nm Ag / 130 nm NPB. The device structure is visualized in **Fig. 5.15 (a)**. After evaporation, all devices are encapsulated with cover glass using epoxy glue without getter material. The active areas of the devices are ~ 6.1 mm^2, measured using an optical microscope.

- Results

To figure out the effect of the device structure on the performance of OLEDs, different HTL and PEDOT:PSS thicknesses are investigated. Since the HTL thickness determines the position of the emission layer and emitting dipoles relative to the boundaries of the stack, controlling its thickness is crucial to obtain a maximum external quantum efficiency (EQE). The overall device structure is illustrated in **Fig. 5.15 (a)**; the selected stacks are visualized in the simulated photon flux map in **Fig. 5.15 (b)**. The transmittance of 60 nm and 130 nm thick

PEDOT:PSS films used in this work are 88.9 % and 84.4 % at a wavelength of 550 nm, respectively (**Fig. 5.15 (c)**). The transmittance of the ITO reference film (83.6 %) is close to that of the 130 nm thick PEDOT:PSS film. Since the refractive indices and extinction coefficients of the two investigated electrode materials differ substantially (see **Fig. 5.16**), it is important that the device structure is modified to the respective optimum stacks according to the type of electrodes, using thin film optics. Although both 60 nm and 130 nm thick PEDOT:PSS thin films yield much higher sheet resistances of 209 ohm/sq and 93 ohm/sq, respectively, compared to ITO (30 ohm/sq), the following results show a promising performance of PEDOT:PSS-based OLEDs in small area devices. To scale-up of OLEDs based on PEDOT:PSS electrodes, an additional metal grid within the active area is required to reduce electrical losses. The calculated σ_{dc}/σ_{Op} value of 60 nm and 130 nm thick PEDOT:PSS films are 52.2 and 46, respectively. Their σ_{dc}/σ_{Op} values exceed the minimum σ_{dc}/σ_{Op} ratio of 35, which is sometimes cited as a minimum requirement for practical use. Thus, the PEDOT:PSS films show great performance as highly conductive electrodes and maybe used in practical device applications.[173]
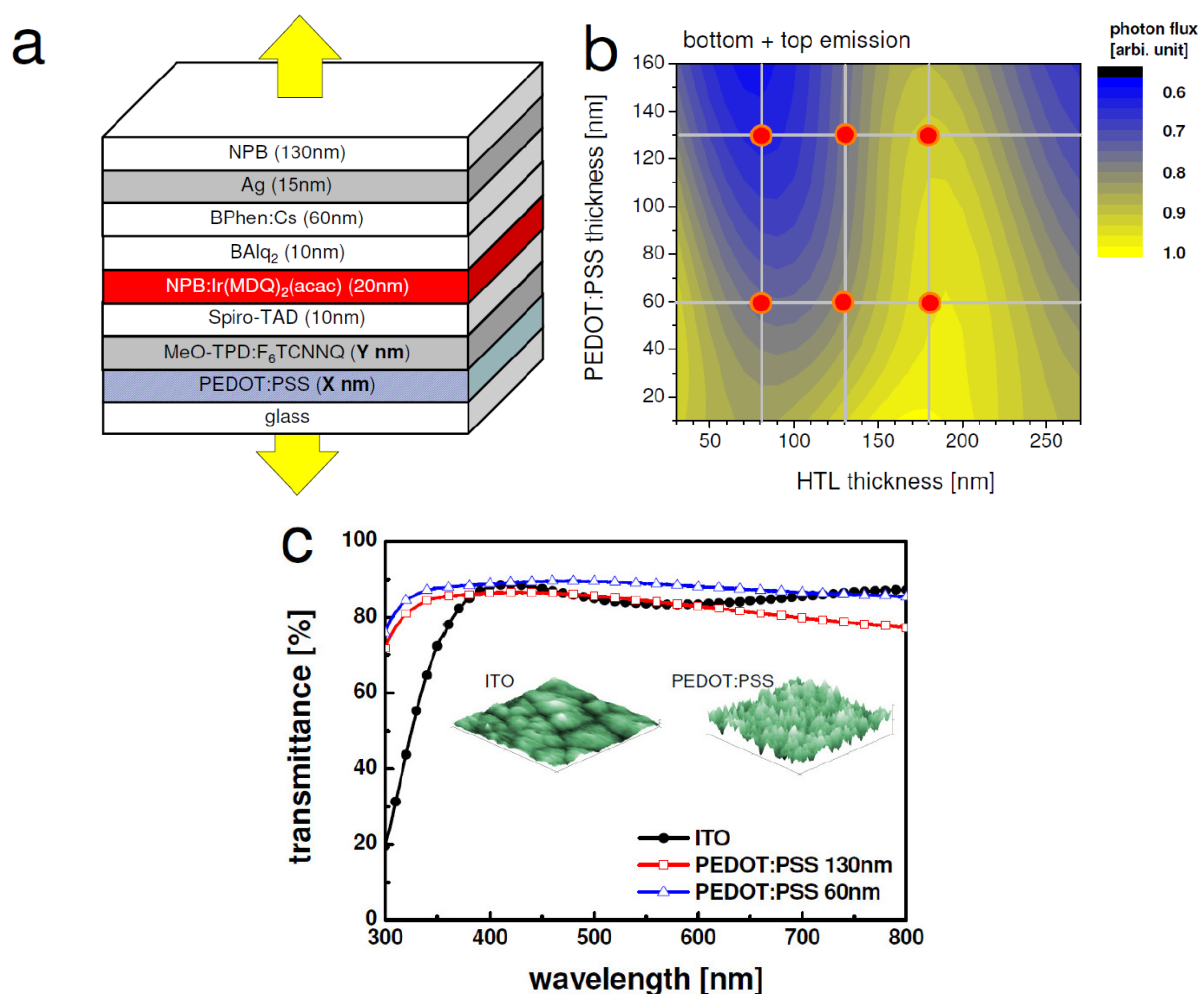
Figure 5.15. *(a) The device structure of ITO-free transparent red OLEDs based on a PEDOT:PSS electrode. The thicknesses of PEDOT:PSS and HTL are varied. (X: 60, 130 nm, Y: 80, 130, 180 nm) (b) Simulated out-coupled photon flux in both bottom and top directions as a function of HTL and PEDOT:PSS thickness. Red dots represent the selected thicknesses for the fabrication of OLEDs. (c) Transmittances of the electrodes used. The inset shows the surface topography of ITO and PEDOT:PSS, measured by AFM (1 × 1 μm^2).*

The surface morphology of the electrodes can greatly influence the shunt behavior of OLEDs in the low voltage regime. As shown in the inset of **Fig. 5.15 (c)**, the surface of ITO is very smooth whereas PEDOT:PSS shows a rough topography by comparison. The corresponding root-mean-square roughness values of ITO and PEDOT:PSS are around 0.4 nm and 1.6 nm, respectively. In the literature, thin films of PEDOT:PSS are frequently reported to smooth the ITO surface and reduce electrical shorts. The relatively high roughness of PEDOT:PSS used in our experiment, however, is due to the use of different, highly conductive formulation and it is further aggravated during the post-annealing process directly after spin-coating of films. During this process, the residual solvent, i.e. ethylene glycol, evaporates, which remarkably transforms the surface topography of the films. Despite the relatively rough surface of PEDOT:PSS, it can be successfully used in organic solar cells as well as in OLEDs.[174, 175]

Prior to the fabrication of devices, we simulate the external photon flux of OLEDs in order to optimize the device structure as shown in **Fig. 5.15 (b)**. The simulation is based on a transfer matrix approach for obtaining the electromagnetic field in planar OLED structures.[156, 176] The number of out-coupled photons is calculated according to

$$\text{photon flux} \propto \frac{2\pi}{hc} \int \int \lambda I_e'(\lambda, \theta) \sin\theta \, d\lambda \, d\theta \tag{4}$$

where λ is the wavelength, θ is the viewing angle, I_e' is the simulated spectral radiant intensity, h is the Planck constant, and c is the speed of light in vacuum. Exciton annihilation processes such as triplet-triplet annihilation and triplet-polaron annihilation are not considered in this simulation. Therefore, the comparison to experimentally obtained EQEs is performed in the low current density region, where annihilation processes are of minor importance. It is shown that the thicknesses of the bottom electrodes and the HTL significantly influence the photon flux. The maximum photon flux of PEDOT:PSS-based OLEDs is obtained for a ~180 nm thick HTL and a rather thin PEDOT:PSS layer. The relatively large optical absorption coefficient of PEDOT:PSS is a limiting factor in the OLED performance; from an optical

viewpoint a thin and highly transparent PEDOT:PSS is therefore desirable for high efficiency devices.
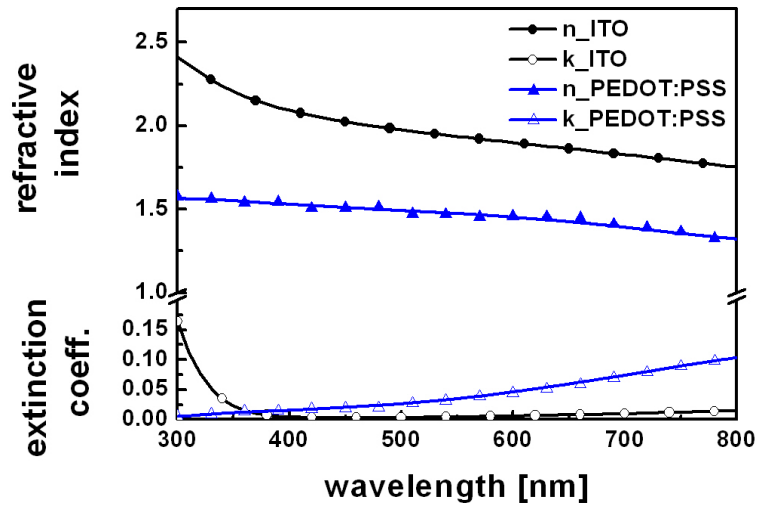

Figure 5.16. *The refractive indices and extinction coefficients of ITO and PEDOT:PSS films*

Based on the simulation predictions, six kinds of ITO-free OLEDs with various HTL and PEDOT:PSS thicknesses and three kinds of reference ITO-based OLEDs with various HTL thicknesses are fabricated. **Figure 5.17** presents the EQE data of those OLEDs. The EQE is calibrated using the angular dependent emission spectra, ensuring reasonable results. It is important that the EQE for transparent OLEDs needs to be evaluated taking the angular dependence behavior into account since the top emission significantly deviates from the Lambertian behavior.[177, 178] The EQE is calculated by

$$\text{EQE} = \frac{2\pi e}{Ihc} \int \int \lambda I_e(\lambda, \theta) \sin\theta d\lambda d\theta \tag{5}$$

where e is the elementary charge, I is the current through the device and I_e is the measured spectral radiant intensity. It is observed that the optimum HTL thicknesses are different for different kinds of bottom electrodes, seen from both simulation and experimental results. In the series of OLEDs with ITO (Device_ITO) bottom contacts, the highest EQE of 11.9 % (sum of bottom and top emission at a current density of 10 mA/cm^2) is observed at a HTL thickness of 80 nm. For the PEDOT:PSS-based devices, the OLEDs having a 60 nm thick PEDOT:PSS (Device_ PEDOT60) electrode exhibit the highest EQE of 12.1 % at a HTL thickness of 180 nm. Despite the higher sheet resistance of PEDOT:PSS compared to ITO, the performance of PEDOT:PSS-based OLEDs in optimal condition is comparable to that of ITO-based OLEDs. The high performance of PEDOT:PSS-based OLEDs is mainly attributed to the weak microcavity effect, which reduces organic waveguided mode as described by Cai et

al.[179] The lower refractive index of PEDOT:PSS (n~1.5), which nearly matches to glass (n~1.5), causes the different cavity length and organic waveguided mode from those of ITO-based OLEDs. In addition, the use of a doped HTL allows an ohmic interface between PEDOT:PSS and HTL despite the high sheet resistance of PEDOT:PSS, which enhances hole injection and minimizes energy loss.[6, 180] This is observed experimentally, as the onset voltages of the PEDOT:PSS- and ITO-based OLEDs in our work are almost equal (2.3 V), despite of the work function difference between PEDOT:PSS (~5.0 eV) and ITO (~4.8 eV).
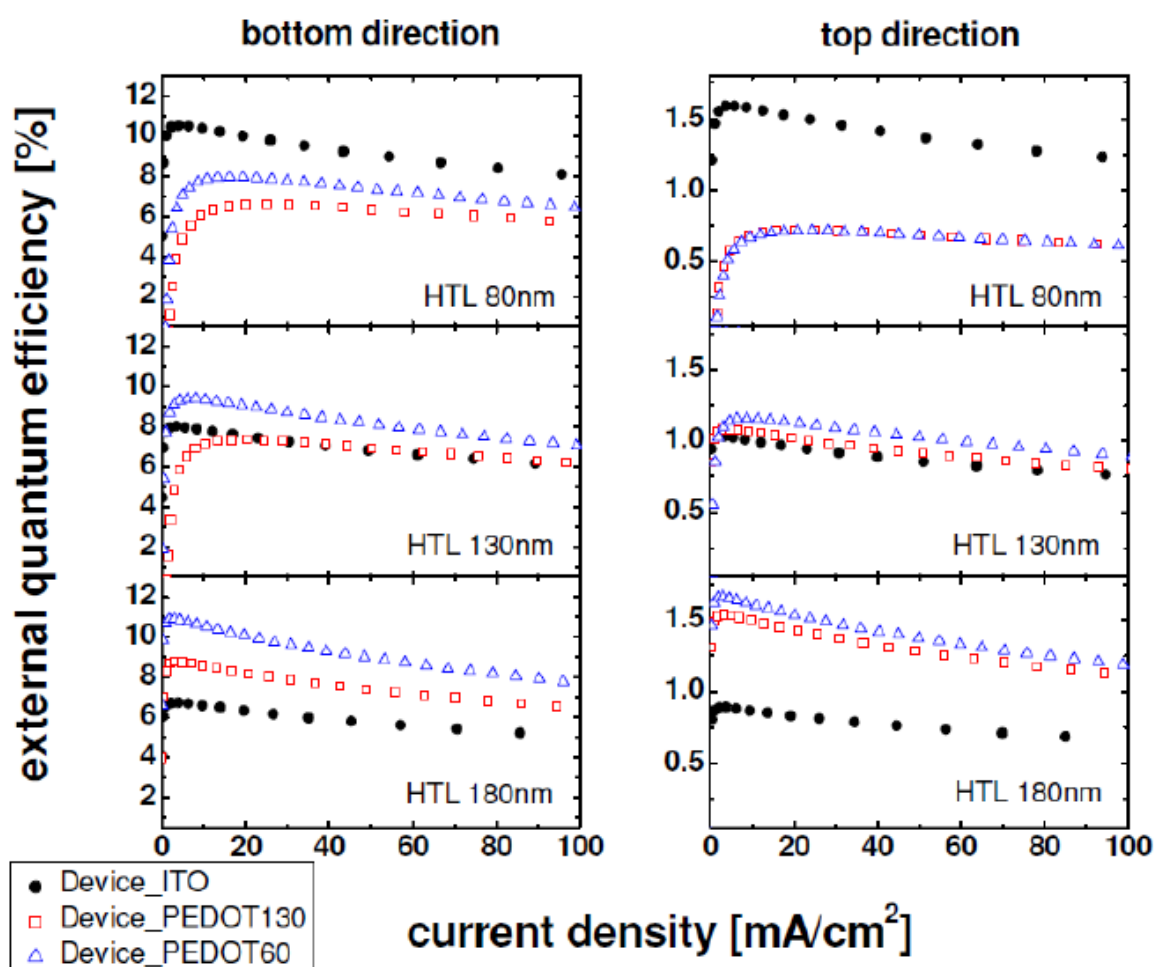
Figure 5.17. The EQE of ITO- and PEDOT:PSS-based OLEDs as a function of the type of electrodes and HTL thicknesses.

As expected, the device performance is significantly changed by the various HTL thicknesses. **Figure 5.18** shows both experimental EQE and simulated photon fluxes, which are agree well. The EQE of the Device_ITO decreases with increasing HTL thickness for both bottom and top emission. In contrast, devices with PEDOT:PSS electrodes show an increasing EQE with increasing HTL thickness. Furthermore, the thickness of the PEDOT:PSS electrodes

remarkably affects the performance of the OLEDs. The Device_ PEDOT60 series consistently shows higher EQEs than devices with 130 nm thick PEDOT:PSS electrodes (Device_ PEDOT130). This is seen for all HTL thicknesses studied here and in both bottom and top emission. These results indicate that thickness tuning for both doped transport layers and electrodes is of great importance to maximize the amount of light extracted from the devices. It should be highlighted that the OLED performance is drastically influenced by the device geometry, especially the type of electrodes. Photon flux for the Device_ITO reaches its maximum at the same HTL thickness where PEDOT:PSS-based OLEDs have a minimum. Thus, to study the application of alternative electrodes in OLEDs, the adequate device structure needs to be investigated taking the changed optics of the respective electrodes into account. As expected, the behavior of the current efficiency in OLEDs is similar to that of the EQE. Furthermore, it is observed that the bottom to top emission ratio can be also controlled by changing the thickness of the HTL or the electrodes as shown in **Table 5.3**.
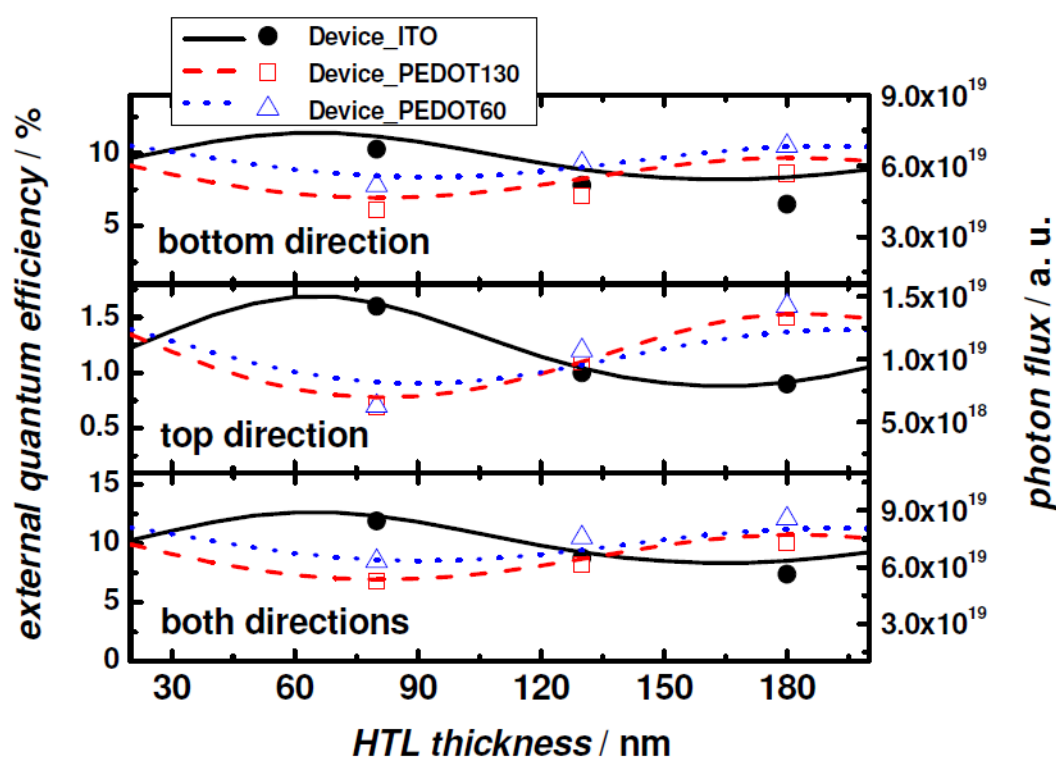

Figure 5.18. *The comparison of EQEs and corresponding photon fluxes for bottom, top emission, and the sum of both, obtained from experiment (symbols) and optical simulation (lines), respectively.*

Figure 5.19 (a) shows the normalized electroluminescence (EL) spectra of the Device_ITO and Device_PEDOT60 at HTL thicknesses of 80 nm and 180 nm, respectively, i.e. at the

thickness for which each device shows the best EQE value. The normalized EL spectra of the best performing ITO- and PEDOT:PSS-based OLEDs are nearly equal for both bottom and top emissions with the peak at a wavelength of 617 nm. However, non-optimized devices show blue shifted EL peaks together with reduced EQE, due to the device stack deviating from the optimal condition. Spectral angular-dependent emission characteristics are also investigated for the best devices in each series of ITO- and PEDOT:PSS-based OLEDs by spectro-goniometer measurements, showing the influence of different electrodes on the emission distribution with viewing angles (**Fig. 5.19 (b)**). The bottom emission of both devices is closer to the Lambertian emission pattern than the top emission which shows the non-Lambertian nature. Especially, the Device_PEDOT60 exhibits a nearly perfect Lambertian emission pattern in the bottom direction due to the optimized cavity length.

		Device_ITO	Device_PEDOT130	Device_PEDOT60
HTL 80 nm	bottom	10.3 %	6.1 %	7.8 %
	top	1.6 %	0.7 %	0.7 %
	total	**11.9 %**	**6.8 %**	**8.5 %**
	bottom:top	6.4:1	8.7:1	11.1
HTL 130 nm	bottom	7.8 %	7.1 %	9.3 %
	top	1.0 %	1.1 %	1.2 %
	total	**8.8 %**	**8.2 %**	**10.5 %**
	bottom:top	7.8:1	6.5:1	7.8:1
HTL 180 nm	bottom	6.5 %	8.6 %	10.5 %
	top	0.9 %	1.5 %	1.6 %
	total	**7.4 %**	**10.1 %**	**12.1 %**
	bottom:top	7.2:1	5.7:1	6.6:1

Table 5.3. *EQE values and bottom to top EQE ratio of OLEDs with various electrode types and HTL thicknesses at a driving current density of 10 mA/cm^2.*
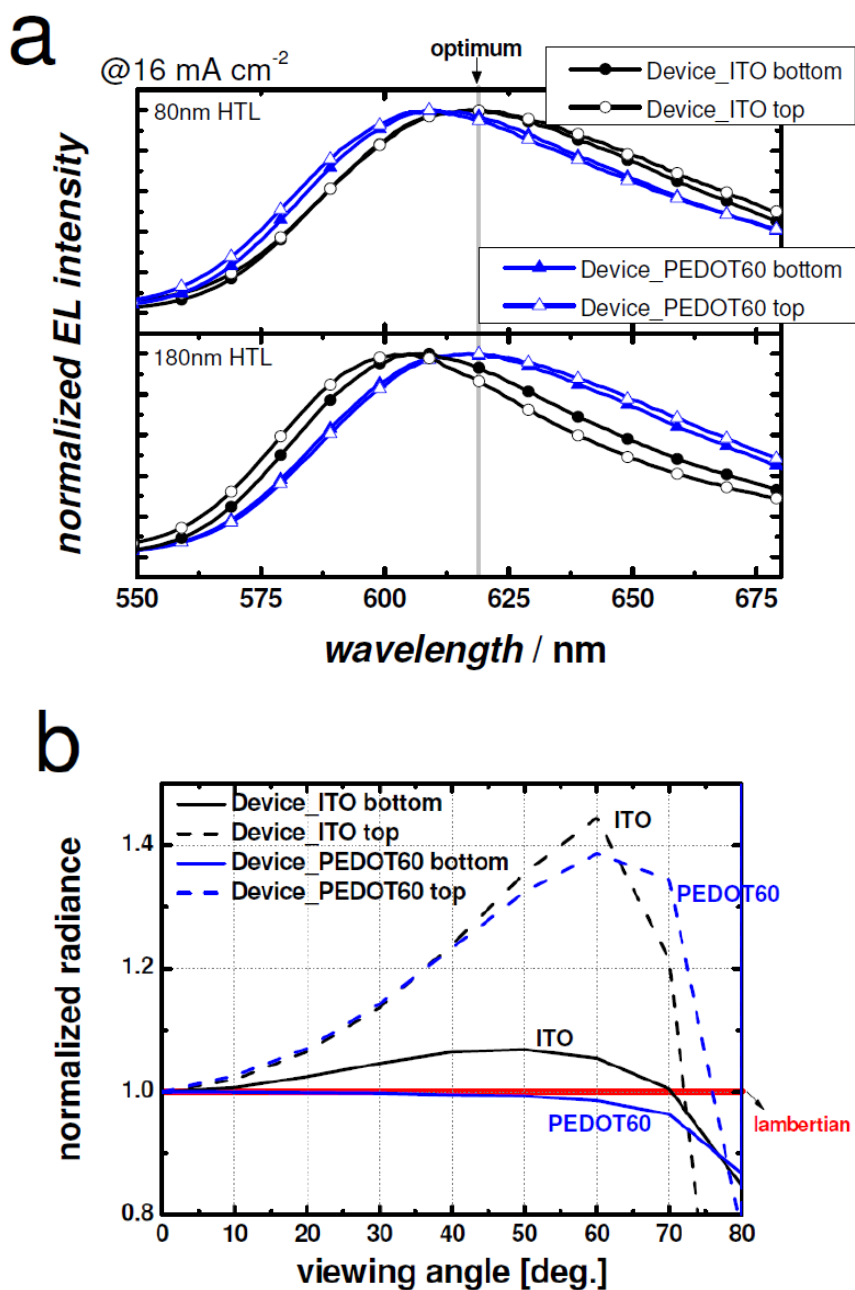
Figure 5.19. *(a) The normalized electroluminescence spectra of Device_ITO and Device_PEDOT:PSS60 with 80 and 180 nm thick HTL. (b) The normalized radiance of devices.*

For practical applications of hygroscopic PEDOT:PSS electrodes in OLEDs, realizing a long and stable lifetime of the devices is of great importance. To investigate the effect of the device structure on the lifetime of the devices, the Device_PEDOT60 with a HTL thickness of 80 nm and the Device_ PEDOT130 with a HTL thickness of 80 nm are chosen for lifetime measurements (**Fig. 5.20**). At high luminance of around 1500 cd/m^2, which is much brighter than in display applications (400-500 cd/m^2), both PEDOT:PSS-based OLEDs do not exhibit

any drop of luminance over 900 hours, showing very stable performance. This indicates that water induced degradation from hygroscopic PEDOT:PSS electrodes is not a significant issue at this condition. To accelerate aging further, we increase the initial luminance to around 5000 cd/m^2. In contrast to the test at lower luminance, the devices with higher luminance exhibit clear degradation behavior. The luminance of the Device_ PEDOT130 exponentially decreases while the Device_ PEDOT60 shows a linear drop of luminescence. It is clearly shown that the thinner PEDOT:PSS electrode leads to better stability. Since the amount of residual water inside the PEDOT:PSS layer strongly depends on the amount of PSS contained, due to the hygroscopic nature of PSS.[59, 68, 180, 181] Thus, thicker PEDOT:PSS electrodes result in poorer stability of the device. It is, therefore, expected that the optimization of the PEDOT:PSS electrode thickness is crucial for designing stable OLEDs.
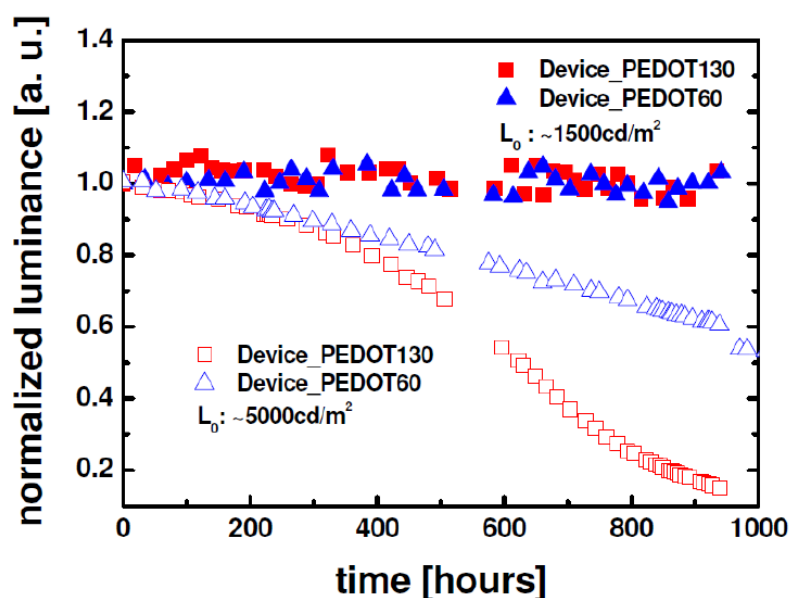

Figure 5.20. *Aging characteristics of PEDOT:PSS-based OLEDs having a different electrode thickness. The encapsulated devices are aged over around 900 hours with an initial luminance of around 1500 or 5000 cd/m^2. Constant currents are applied for each sample according to the corresponding luminance.*

Figure 5.21 shows the transmittance spectra and photographs of selected transparent OLEDs. As can be seen from the photographs, the PEDOT:PSS-based OLEDs show good transmittances in the off-state as well as on-state. The average transmittances in the visible range of the Device_ITO and the PEDOT:PSS-based OLEDs series are 25 ~ 28 % and 22 ~ 25 %, respectively. Due to negligible optical losses in the HTL, the HTL thickness can be increased further without affecting the transmittance of the OLEDs. The thinner

Device_PEDOT60 series shows 2~3 % higher transmittances than the Device_PEDOT130 series at the same HTL thickness regime, indicating that the thickness and absorption of PEDOT:PSS are the critical parameters determining the transmittance of devices. According to the structure engineering, thinner PEDOT:PSS electrodes are more beneficial for transparent OLEDs in our study in terms of efficiency, lifetime, and transmittance of devices.
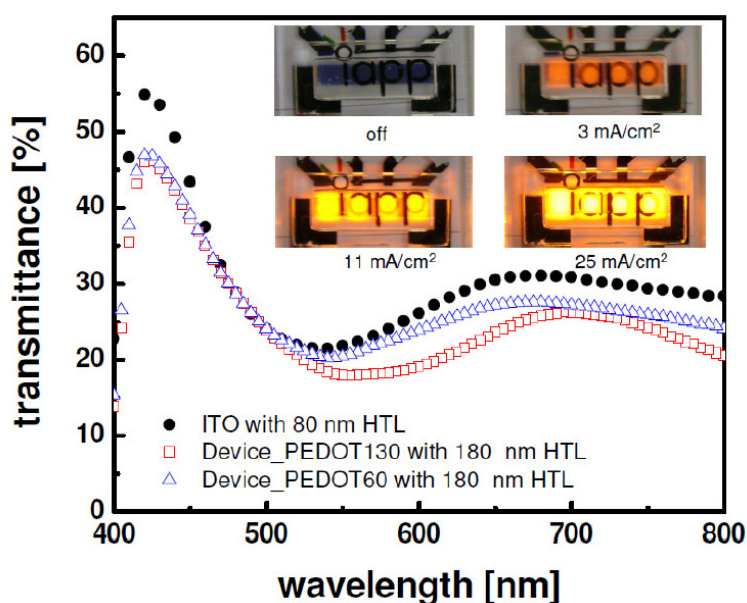

Figure 5.21. Transmittances of transparent OLEDs with respect to different bottom electrodes. Inset shows the top view of red emitting light of PEDOT:PSS-based OLEDs with different applied current densities. Four pixels are connected for lighting.

In summary, we demonstrate efficient ITO-free transparent OLEDs with conductive polymer electrodes. The high performance of the OLEDs is achieved by careful optimization of the device stack, supported by optical simulation, which fits well with the experimental results. The PEDOT:PSS-based OLEDs achieve comparable performance to the ITO-based OLEDs using adapted devices. The doping technology used for the HTL leads to a very low onset voltage of the PEDOT:PSS-based OLEDs despite of the high sheet resistance of electrode. Moreover, a reasonably long lifetime of the PEDOT:PSS-based OLEDs is obtained by tuning the electrode thickness. The structure engineering performed in this work, which improves efficiency, stability, and transmittance of OLEDs with a polymer electrode, is beneficial for realizing low-cost, flexible, and long living OLEDs applications.

5.5. PEDOT:PSS combined with light scattering layer

Here we report on an easily fabricated internal light extraction system composed of a metal oxide nanostructure and a highly conductive low refractive index polymer electrode for OLEDs. The combined beneficial effects of refractive index matching, corrugated structure, and light scattering allow a significant enhancement of the external quantum efficiency of OLEDs. The color stability over viewing angle is also significantly improved by the light out-coupling system.

5.5.1. Development of light out-coupling system

- Preparation of the metal oxide based light extraction system

300 nm thick Sn films are deposited on glass at room temperature by r.f. magnetron sputtering system. The prepared Sn films are annealed under vacuum (10^{-3} mbar) at 300 °C for 30 min, and subsequently annealed in air at 500 °C for 1 hour. A propylene glycol-monomethyl-ether acetate-based photo-resist (Everlight Chemical Industrial Corporation), used as planarization polymer, is spun onto the fabricated metal oxide films. Afterwards, the spin-coated films are annealed on a hot plate at 130 °C for 10 min. As conductive electrode, PEDOT:PSS (PH1000) mixed with 6 vol.% ethylene glycol is spin-coated on the scattering systems. The coated samples are baked at 120 °C for 15 min, as described in chapter 5.

- Results

The manufacturing process of a simple light extraction layer, consisting of metal oxide nanostructures, is shown in **Fig. 5.22 (a)**. 300 nm thick Sn metal films are deposited on glass. By annealing the films in vacuum, the metal films on glass melt and agglomerate on the glass surface driven by thermal energy, forming a nanocluster structure as shown in scanning electron microscope (SEM) images of **Fig. 5.22 (c)**. The treated films are subsequently annealed at 500 °C in air for the through oxidation of films. The resulting films show randomly distributed metal oxide nanoclusters with size of tens to hundreds of nanometers. The integration of such an internal scattering structure into OLEDs is challenging since the nanostructures lead to leakage currents due to high surface roughness. To overcome this issue, a micrometer-thick transparent planarization polymer whose refractive index is around 1.52~1.55 at the visible ranges, is spun onto the metal oxide nanoclusters. We name this metal oxide based light extraction system MOLES in the following.
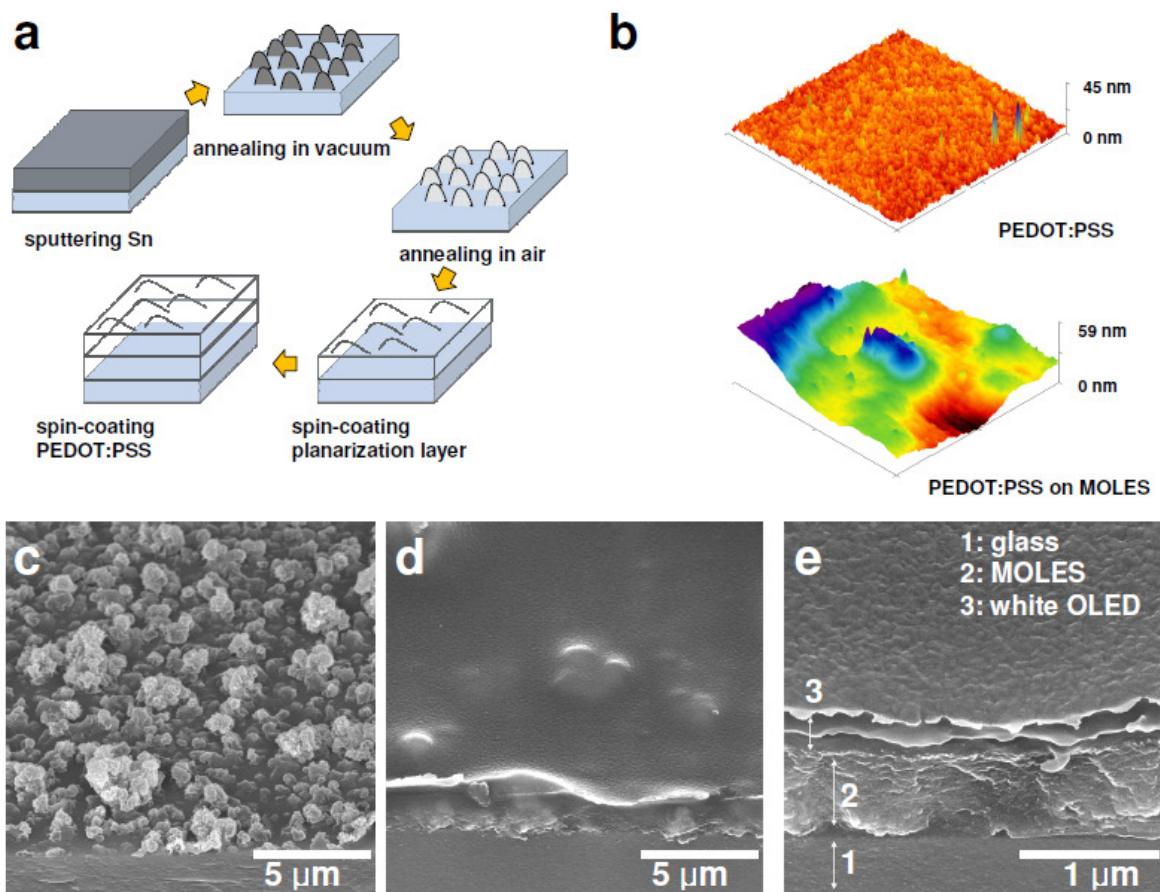
Figure 5.22. *The fabrication of MOLES. (a) Schematic process flow for spontaneously formed metal oxide embedded light scattering systems (MOLES). (b) AFM images of PEDOT:PSS polymer electrodes on planar glass and on MOLES (6×6 μm^2). Tilted SEM images of (c) metal oxide scattering films without planarization layers and (d, e) white OLEDs on MOLES.*

The total (specular + diffuse) and diffuse transmittances of the scattering system are shown in **Fig. 5.23 (a)**. The oxidized Sn film shows a total and diffuse transmittance of 77.0 and 57.6 %, respectively, at a wavelength of 550 nm. The high total (i.e. low absorption) and diffuse (i.e. scattering effects) transmittance of these light out-coupling films are expected to greatly increase the out-coupling of light from the OLEDs with minimal absorption losses. After coating the planarization layer, the total transmittance slightly increases but the diffuse transmittance decreases more than 10 % because of a reduced refractive index difference between the surrounding media and the scattering nanoparticles. Nevertheless, the diffuse transmittance is high enough to scatter light efficiently. The uniformity of the scattering films is observed to be excellent since the initial metal films are homogeneously sputtered, showing the potential for an easy scalable process in practical production (**Fig. 5.23(c)**).
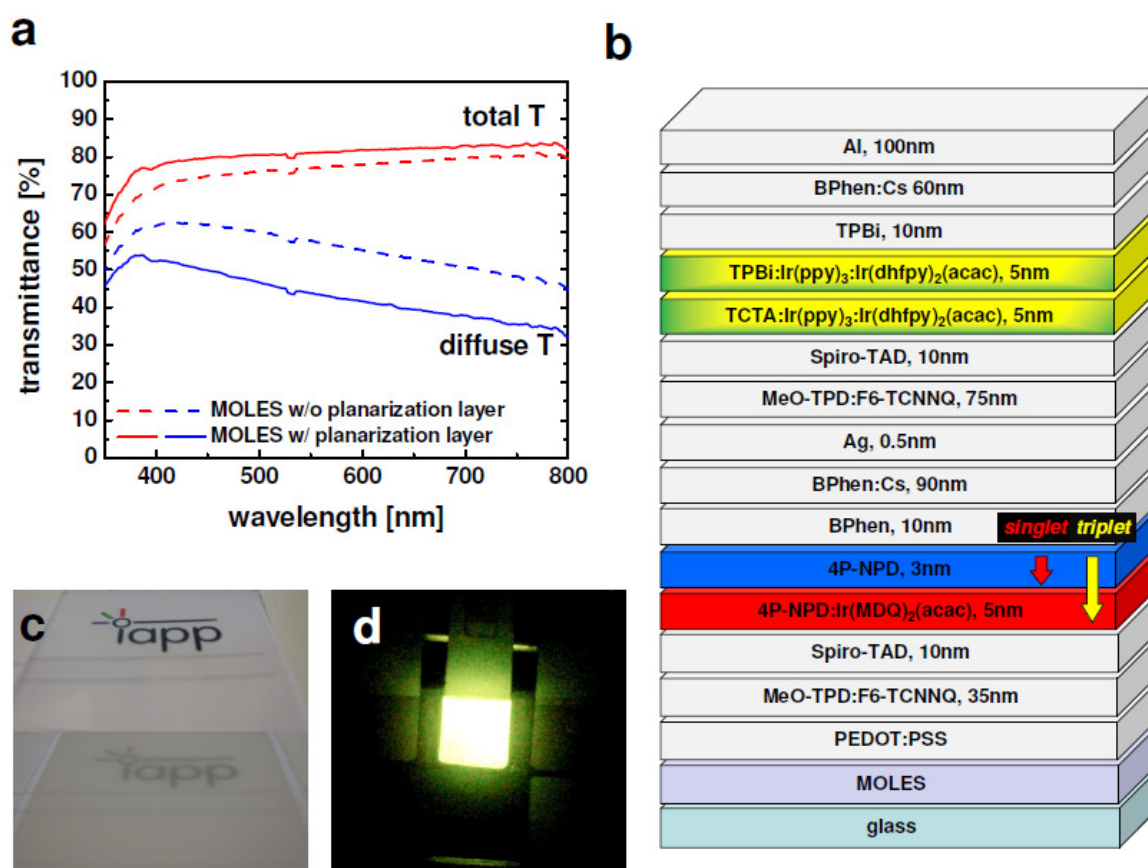
Figure 5.23. *OLED stack and characteristics of the light scattering systems. (a) Transmittances of the scattering film with and without planarization layer. (b) Device structures of white OLEDs with MOLES. (c) Photographs of (top) bare glass and (bottom) scattering film without planarization layers, sitting on the institute logo. (d) A photograph of a white OLED with embedded MOLES.*

For the transparent bottom electrode on top of MOLES, we adopt conductive PEDOT:PSS to minimize refractive index mismatching. The refractive index of PEDOT:PSS (n=~1.5) is similar to that of the planarization polymer. Therefore, the internal reflection between the electrode and the MOLES is significantly reduced by using PEDOT:PSS compared to the use of ITO (n=~2.0). Moreover, wave-guided modes which trap photons in between glass (n=~1.5) and electrode can be notably suppressed by using the low refractive index PEDOT:PSS electrode. Our previous studies showed comparable or even better performance for organic opto-electronic devices based on the highly conductive PEDOT:PSS electrodes in comparison with the ITO electrode for applications in organic solar cells as well as OLEDs.

Figure 5.22 (b) shows atomic force microscopy (AFM) images of MOLES with electrode coating on top. It is observed that the corresponding root mean square (RMS) roughness of the electrode coated MOLES is around 6 nm, which is smooth enough not to cause the electrical short of devices. It is notable that these MOLES show spontaneously corrugated and grooved surfaces despite of the planarization layer, caused by the embedded metal oxide nanoclusters as shown in AFM and SEM images (**Fig. 5.22**), which contribute to interface scattering. In addition, the metal oxide nanoclusters (n=~1.9) have a high optical contrast between glass (n=~1.5) and planarization layer (n=1.52~1.55) and act as scattering objects. The smooth corrugated surface as well as the light scattering effect by the high contrast nanoparticles is the one of key factors to improve the white OLEDs performance, as discussed below.

5.5.2. Enhanced light extraction in OLEDs

- Fabrication of the white OLEDs

The layer sequence used for the white OLEDs is as follows (from bottom to top)[182]: glass substrate / MOLES / PEDOT:PSS / 35 nm (N,N,N',N'-tetrakis(4-methoxyphenyl)-benzidine) (MeO-TPD) : 2,2'-(perfluoronaphthalene-2,6-diylidene)dimalononitrile (F6-TCNNQ) (2 wt.%) / 10 nm 2,2',7,7'-tetrakis-(N,N'-diphenylamino)-9,9'-spirobifluorene (Spiro-TAD) / 5 nm N,N'-di-1-naphthalenyl-N,N'-diphenyl-[1,1':4',1":4",1'''-Quaterpheny]l-4,4'''-diamine (4P-NPD) : Iridium(III)bis(2-methyldibenzo-[f,h]chinoxalin)(acetylacetonat) (Ir(MDQ)$_2$(acac)) (5 wt.%) / 3 nm 4P-NPD / 10 nm 4,7-diphenyl-1,10-phenanthroline (BPhen) / 90 nm BPhen : Cs (1:1) / 0.5 nm Ag / 75 nm MeO-TPD : F6-TCNNQ (2 wt.%) / 10 nm Spiro-TAD / 5 nm 4,4',4" tris(N-carbazolyl)-triphenylamine (TCTA) : fac-tris(2-phenylpyridine) iridium(III) (Ir(ppy)$_3$) : bis(2-(9,9-dihexylfluorenyl)-1-pyridine) (acetylacetonate) iridium(III) (Ir(dhfpy)$_2$(acac)) (91:8:1 wt.%) / 5 nm 2,2'2"-(1,3,5-benzenetriyl)-tris[1-phenyl-1H-benzimidazole] (TPBi) : Ir(ppy)$_3$: Ir(dhfpy)$_2$(acac) (91:8:1 wt.%) / 10 nm TPBi / 60 nm BPhen : Cs (1:1) / 100 nm Al.

- Results

Having designed the combination of MOLES and PEDOT:PSS, we fabricate white OLEDs on it. The white OLEDs stack is carefully optimized to exhibit high performance, consisting of a green/yellow unit and an efficient triplet harvesting blue/red unit in a tandem structure[182]. Three different systems are used in this experiment: The Device_ITO is the reference device with ITO electrode without MOLES. The Device_PEDOT is the reference with PEDOT:PSS

electrode without MOLES. The Device_MOLES is based on the PEDOT:PSS electrode on MOLES.

The resulting current density-voltage-luminance (*J-V-L*) characteristics of the devices are shown in **Fig. 5.24 (a)**. When comparing two reference devices based on ITO and PEDOT:PSS electrodes, the influence of the bottom electrodes on the OLEDs performance is clearly observed. The Device_PEDOT shows higher operating voltages compared to the reference Device_ITO due to the relatively low conductivity of PEDOT:PSS which causes lower luminance at the high brightness region. Although the luminous efficacy of the Device_PEDOT (13.1 lm/W) is slightly lower than that of the Device_ITO (14.5 lm/W), the EQE of the Device_PEDOT (14.3 %) is even higher than that of the Device_ITO (12.3 %) at a brightness of 10000 cd/m^2. This enhancement is mainly caused by suppressed wave-guided mode resulting from an adequate refractive index matching of the glass/MOLES/PEDOT:PSS/organic layers as discussed earlier.

By comparison with the two reference devices, the Device_MOLES shows greatly improved EQE as shown in **Fig. 5.24 (b)** and summarized in **Table 5.4**. The EQE of the Device_MOLES reaches over 20.3 % at a brightness of 10000 cd/m^2, and is improved by a factor of 1.7 compared to the reference Device_ITO. To our knowledge, this enhancement factor is one of the highest values reported for white OLEDs without any additional external out-coupling structures. To investigate and extract further trapped photons in the glass mode, an index-matched hemisphere lens is applied on the glass substrate during the measurement in an integrating sphere at a constant current. As summarized in **Table 5.4**, the Device_MOLES shows significantly increased EQE from 20.3 to 35.6 % (increment: 15.3 %) by the hemisphere lens, while the EQE of the reference Device_ITO with the hemisphere lens increases from 12.3 to 20.8 % (increment: 8.5 %), showing much more extracted glass mode due to more extracted organic mode by MOLES. Finally, the Device_MOLES shows a significant improvement of EQE by a factor of 2.9 compared to the reference Device_ITO without the lens at the high brightness of 10000 cd/m^2 (**Fig. 5.24 (c)**), which is the highest enhancement reported for white OLEDs to the best of our knowledge.
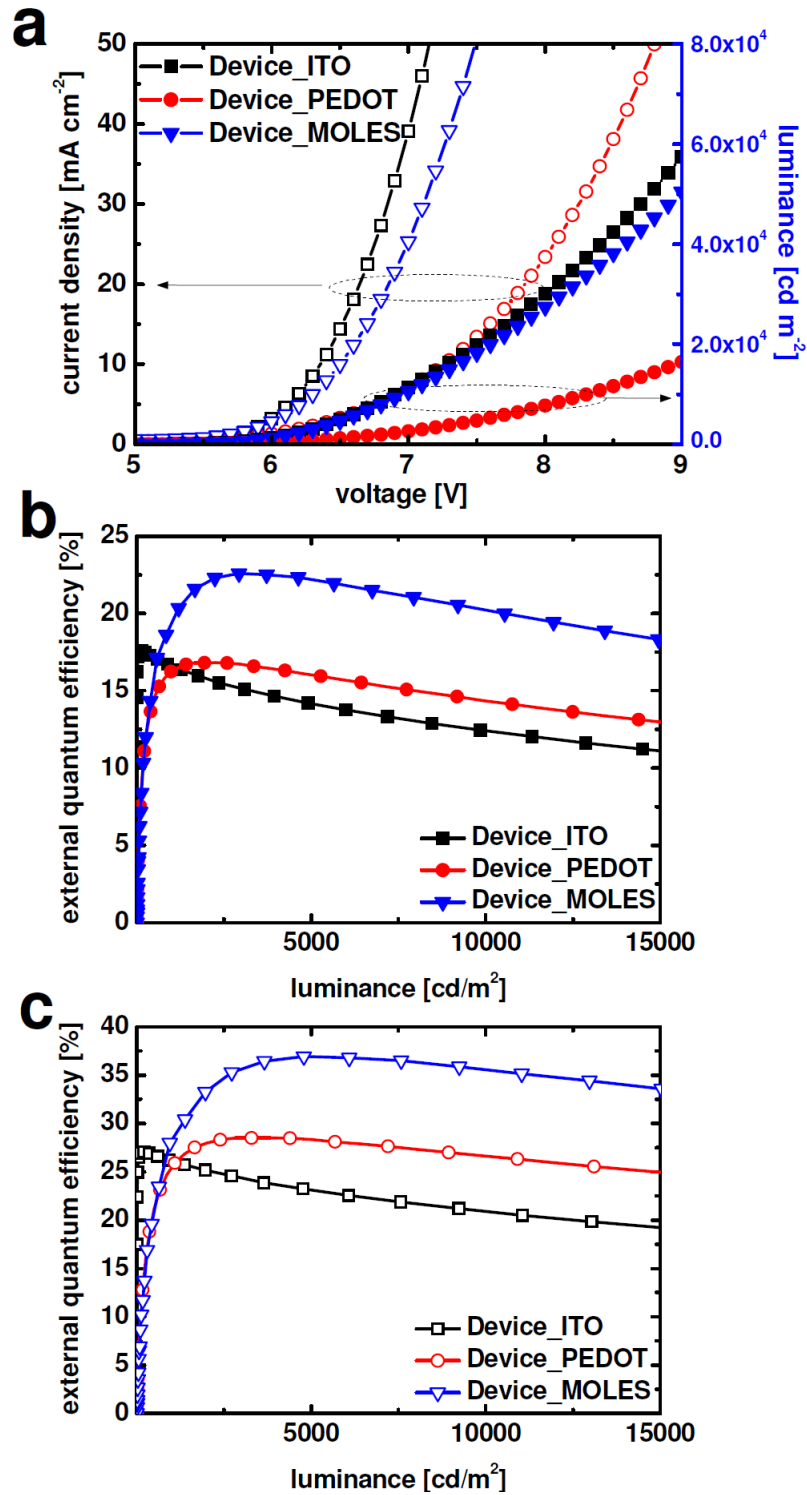
Figure 5.24. *Performance of white OLEDs. (a) Current density and luminance spectra as a function of driving voltages. The external quantum efficiency spectra as a function of luminance for white OLEDs (b) without and (c) with a hemisphere lens.*

It is interesting to note that the Device_MOLES shows a greatly reduced operating voltage which is far closer to that of the Device_ITO. This voltage reduction is attributed to the corrugated surface of our system as shown in AFM and SEM images. It is reported that

94

corrugated substrates improve not only the out-coupling efficiency, but also the electrical performance caused by a partially reduced organic layer thickness[183, 184]. The spontaneously formed corrugated surface structure of MOLES results in beneficial effects of better charge injection and reduction of the operating voltage. Furthermore, considering the large enhancement of EQE with the hemisphere lens, MOLES extracts the organic mode very efficiently, resulting that large parts of glass mode can be extracted. We highlight that the strongly improved out-coupling efficiency at high brightness is a very promising for practical lighting applications. It is further observed that the total/diffuse transmittance and surface roughness of MOLES can be tuned by control of thickness, material, and composition of metal films (**Fig. 5.25**), showing room for further improvement.
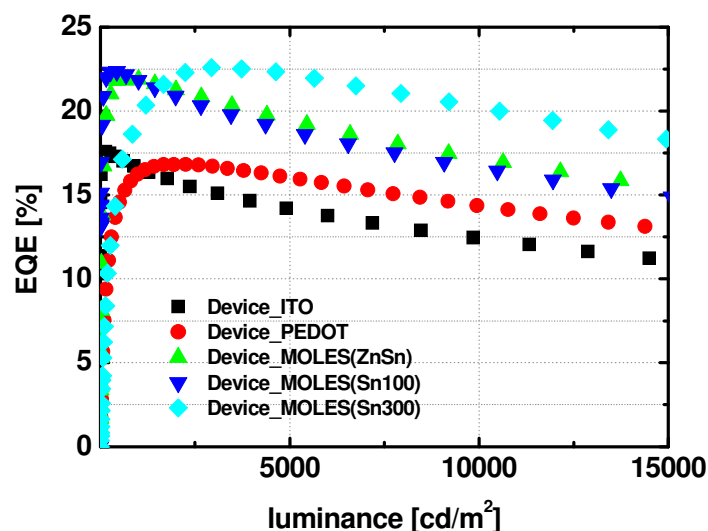
Figure 5.25. *The EQE spectra for the reference Device_ITO and the device with MOLES fabricated from a 100 nm thick ZnSn alloy, a 100 nm thick Sn, and a 300 nm thick Sn.*

@10000 cd/m^2	w/o hemisphere lens			w/ hemisphere lens		
	Lm/W	EQE	EQE enhancement	lm/W	EQE	EQE enhancement
Device_ITO	14.5	12.3	x	25.4	20.8	1.8
Device_PEDOT	13.1	14.3	1.2	26.1	26.6	2.2
Device_MOLES	22.7	20.3	1.7	41.6	35.6	2.9

Table 5.4. *Parameters of white OLEDs at 10000 cd/m² based on the reference and different types of MOLES. The enhancement values are calculated from the reference Device_ITO (marked X) without a hemisphere lens.*

5.5.3. Improvement of color stability in OLEDs

Besides the enhancement of the light out-coupling efficiency, the color stability of the white OLEDs is also markedly improved by MOLES. **Figure 5.26 (b)** shows the angular emission of the Device_MOLES. The emission dependence of the Device_MOLES on viewing angles is very small compared to the Device_ITO (**Fig. 5.26 (a)**), showing high quality white light. **Figure 5.26 (c)** presents the behavior of the Commission Internationale del'Eclairage (CIE) color coordinates of the devices with respect to the viewing angle. The Device_MOLES exhibits an extremely stable color balance as a function of the viewing angle, indicating that MOLES drastically suppresses the color shift of the device due to re-distribution of photons by scattering[49, 50]. Stabilizing the color balance of white OLEDs a very challenging task, due to the wide emission spectrum, which is important for researchers and OLED manufacturers. Thus, we believe the great color stability, achieved by scattering with MOLES is a great achievement for OLED development and some kind of scattering layer has to be included in any commercial, white OLED product.

In summary, we have developed a highly efficient internal light extraction and color stabilizing system by using a simple and easy manufacturing process. The metal oxide embedded nanostructures (MOLES) combined with a conductive polymer electrode show a superior refractive index matching from organic layer to the substrate, a simultaneously formed corrugated surface, and an excellent light scattering effect, resulting in a greatly enhanced EQE of white OLEDs by factor of 2.9 at a high luminance of 10000 cd/m² together with an excellent color stability over broad viewing angles. Furthermore, an improvement of lifetime in white OLEDs is expected caused by the enhanced luminous efficacy.
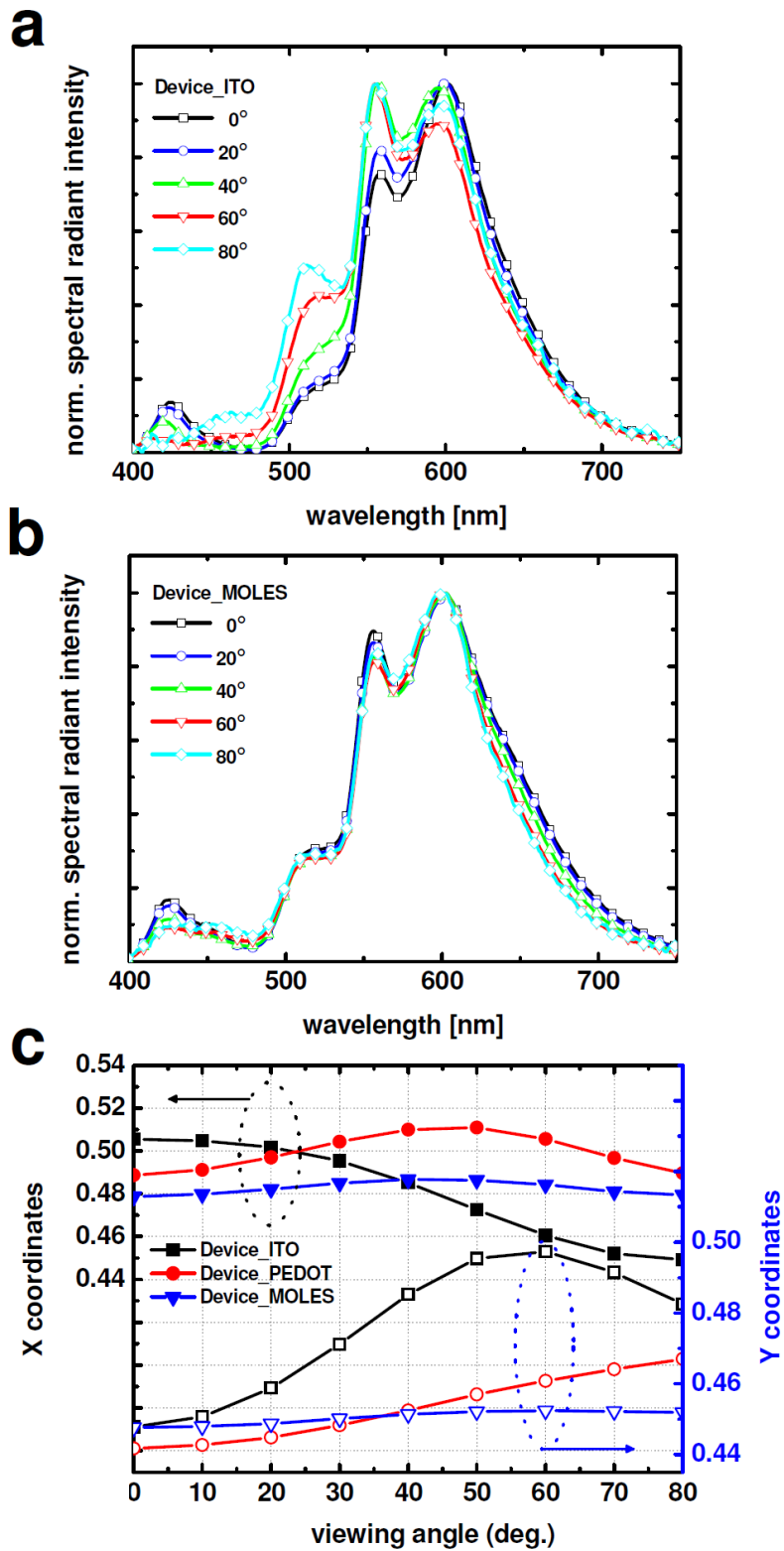
Figure 5.26. *Angular color dependence of white OLEDs. Normalized spectral emission intensity for (a) the Device_ITO and (b) the Device_MOLES for different viewing angle. (c) CIE coordinate shift of the white OLEDs over the viewing angle. Note the minimal shift of the MOLES device.*

Chapter 6. ZnO electrodes co-doped with non-metallic dopants[*]

6.1. Introduction

Doped ZnO films are regarded as a promising alternative electrode to replace indium tin oxide (ITO) due to its low material cost, high transmittance and conductivity. Metallic elements such as aluminum and gallium are the most widely studied dopants on ZnO films, providing a high electrical conductivity. However, these films suffer from significant optical absorption loss in near infra-red (IR) and visible range due to free carrier absorption, and strong perturbation of the conduction band from each metallic dopant. In contrast to metallic dopants, studies on anionic dopants such as fluorine are rare in spite of their possible benefit in producing ZnO films with high figure of merit in conjunction with low optical absorption loss.[185, 186] Fluorine dopants substitute oxygen atoms whose orbitals dominate the valence band states. Therefore fluorine donors have only little influence on the conduction band states, resulting in low free carrier scattering. In addition, a proper dose of fluorine dopants in the ZnO films has been reported to enhance the crystallization of ZnO and to reduce grain boundary scattering.[187] Another effective dopant in ZnO films is hydrogen. When doped, hydrogen is known to form an O-H complex which acts like an anionic dopant.[188, 189] Hydrogen incorporated into ZnO films can increase the carrier concentration as well as passivate the grain boundaries.[190-192] Furthermore, our previous studies on ZnO or ZnO:Al films co-doped with hydrogen and fluorine have shown that balancing the dopant contents and subsequent annealing could yield ZnO films with high figure of merit via counter acting mechanisms of hydrogen and fluorine.[190, 191] A schematic illustration of the ZnO structures co-doped with non-metallic dopants and the acting mechanisms is presented in **Fig. 6.1**.

In this study, we successfully produce high performance ZnO electrodes co-doped with alternative non-metallic dopants and report enhanced efficiencies in small molecule OPV cells and OLEDs using the alternative transparent conducting oxides (TCO).

---

[*] The content of chapter 6 is accepted in *Advanced Functional Materials*.
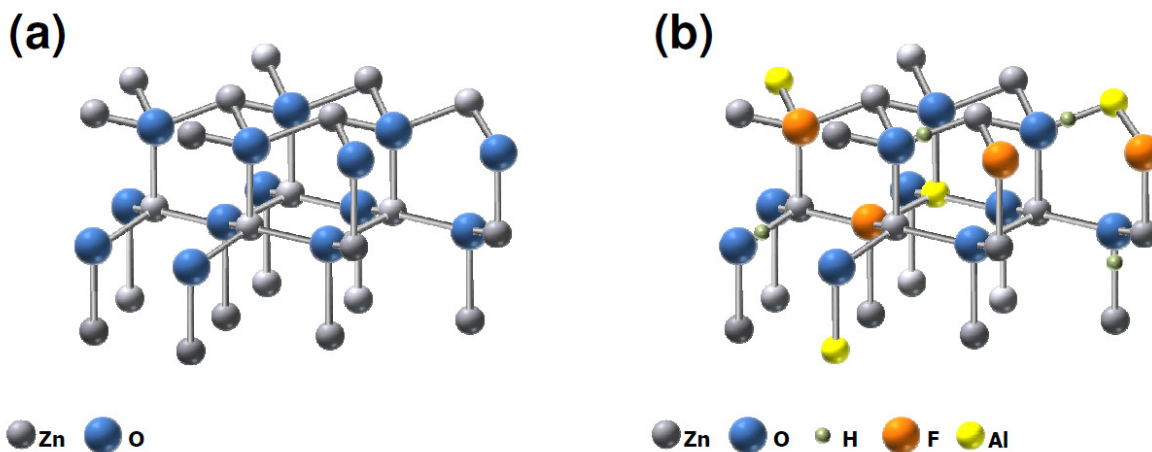
Figure 6.1. *A schematic illustration of the (a) intrinsic ZnO and (b) co-doped ZnO hexagonal wurtzite structures, illustrating the different doping mechanisms: the classic metallic doping, the electron rich Al atom substitutes a Zn lattice atom and similarly, the electron rich fluorine replaces an oxygen atom, both donating an electron to the system. The hydrogen exists as single isolated interstitial bound with oxygen, thereby acting like fluorine and creating mobile charges.*

6.2. Properties of optimized ZnO films

- Preparation of ZnO films

ZnO thin films doped with aluminum (Al) (ZnO:Al), and co-doped with hydrogen (H) and fluorine (F) (ZnO:H,F), or Al, H and F (ZnO:Al,H,F) are prepared on boronite glass substrates by using a conventional radio frequency (rf) magnetron sputtering system. The films were fabricated at Korea Institute of Science and Technology. The base pressure in the chamber is kept below 5×10^{-7} Torr. For all ZnO based TCO films, the sputtering deposition is carried out at a pressure of 1 mTorr and substrate temperature of 150 $^{\text{o}}$C with an rf power of 50 W. The distance between the target and the substrate is 60 mm, and the substrate is rotated at a constant speed of 12 rpm during sputtering. **Table 6.1** lists the ID of TCO films, the target composition, and sputter gas composition. Among the tested films, only ZnO:Al,H,F film is post-heat treated in vacuum at 300 $^{\text{o}}$C for 1 hour.

TCO ID	Target	Working gas	Remark
ITO	-	-	Reference:purchased
ZnO:Al	ZnO-Al$_2$O$_3$(2 wt.%)	Ar	
ZnO:H,F	ZnO-ZnF$_2$(10 wt.%)	Ar-H$_2$(4 vol.%)	
ZnO:Al,H,F	ZnO-Al$_2$O$_3$(1 wt.%)	Ar-H$_2$(4 vol.%)-CF$_4$(0.4 vol.%)	Annealed in vacuum at 300 ^{o}C

Table 6.1. Fabrication details of TCO electrodes prepared by rf magnetron sputtering. Co-doping process is carried out by using carefully designed mixed target and mixed gas plasma.

- Results

The electrical characteristics of the fabricated ZnO films are summarized in **Table 6.2**. The co-doping process is carried out based on previous experimental conditions by adjusting sputter gas composition as well as the target.[191] For a reliable comparison of the electrode effects on OPV cells, we tried to match the sheet resistances of the ZnO films with that of the ITO reference film by controlling the film thickness. Small differences in the values of sheet resistance are observed due to process variations, especially the nature of decreasing electrical resistivity with increasing film thickness of ZnO films, but those are in an acceptable range for reliable comparison between devices with small cell area.

TCO ID	Thickness (nm)	Resistivity ($\times 10^{-4}$, ρ cm)	Hall mobility (cm^2/Vs)	Carrier density ($\times 10^{20}$, cm^{-3})	Sheet resistance (ohm/sq)	Work function (eV)	σ_{dc}/σ_{Op}
ITO	87	2.28	34.7	7.88	26.3	4.7	142
ZnO:Al	188	6.27	20.3	4.90	33.4	4.4	149
ZnO:H,F	596	14.9	24.4	1.72	24.9	4.3	166
ZnO:Al,H,F	205	4.97	23.8	5.27	24.3	4.5	283

Table 6.2. The electrical characteristics of TCO electrodes. All electrodes are designed to have similar sheet resistances. σ_{dc} and σ_{Op} are the dc and optical conductivities, calculated

from transmittance and sheet resistance. σ_{dc}/σ_{Op} values present a figure of merit for the electrodes used.

Figure 6.2 shows the transmittances, absorption coefficients, and refractive indices of the TCO electrodes used. At sheet resistances of around 24-33 ohm/sq, the average transmittances of ITO, ZnO:Al, ZnO:H,F, and ZnO:Al,H,F in the visible range of 400-800 nm are 83.3, 85.4, 84.1, and 87.2 %, respectively. All ZnO films exhibit higher transmittances than the ITO reference. Since their sheet resistances are roughly equal, the highly transparent ZnO films are expected to be more favorable to the application of OPV cells. The striking feature in ZnO films with hydrogen and fluorine is the very low optical absorption loss as shown in **Fig. 6.2 (b)**. The average absorption coefficient of the ZnO:Al,H,F film is 703 cm^{-1} which is much lower than that of ITO (1724 cm^{-1}) in the visible range. The ZnO:H,F film fully doped with non-metallic contents shows an even lower absorption coefficient of 514 cm^{-1}. When ZnO thin films are fabricated in normal processing conditions, they are known to possess doubly charged defects such as zinc interstitials or oxygen vacancies, even in the presence of extrinsic dopants like aluminum or gallium. Those intrinsic and extrinsic defect centers increase in the optical absorption of thin films. Although zinc interstitials are not stable at room temperature, [193] oxygen vacancies can be formed despite their high formation energy[194] and exist up to 400 °C.[195] Thus, the low absorption losses observed in hydrogen and fluorine co-doped ZnO films are attributed to the removal of oxygen vacancies by fluorine and a lower content of metallic elements.

Furthermore, the refractive index values of the ZnO series are lower than that of ITO, resulting in a reduced refractive index mismatch between the electrodes and the organic layers. Considering these properties, ZnO films are regarded as good alternative electrode material due to their excellent optical properties, i.e. higher transmittance, lower absorption loss, and lower refractive index compared to ITO. A figure of merit for transparent electrodes can be derived from the following equation, linking absorption and conductivity in thin, homogenous films:[196]

$$T = \left(1 + \frac{Z_0}{2R_S} \frac{\sigma_{Op}}{\sigma_{dc}}\right)^{-2} \tag{1}$$

where T is the transmittance, R_S is the sheet resistance, Z_0 (377 ohm) is the impedance of free space, and σ_{Op} and σ_{dc} are the optical and dc conductivities, respectively. The ratio of σ_{dc}/σ_{Op} can be used as a figure of merit and the resulting values for the electrodes used in this study

are shown in **Table 6.2**. As expected, the ZnO:Al,H,F film shows a much higher σ_{dc}/σ_{Op} value (283) than ITO (142), indicating that optimized ZnO films are a superb material for the highly transparent and conductive electrode.
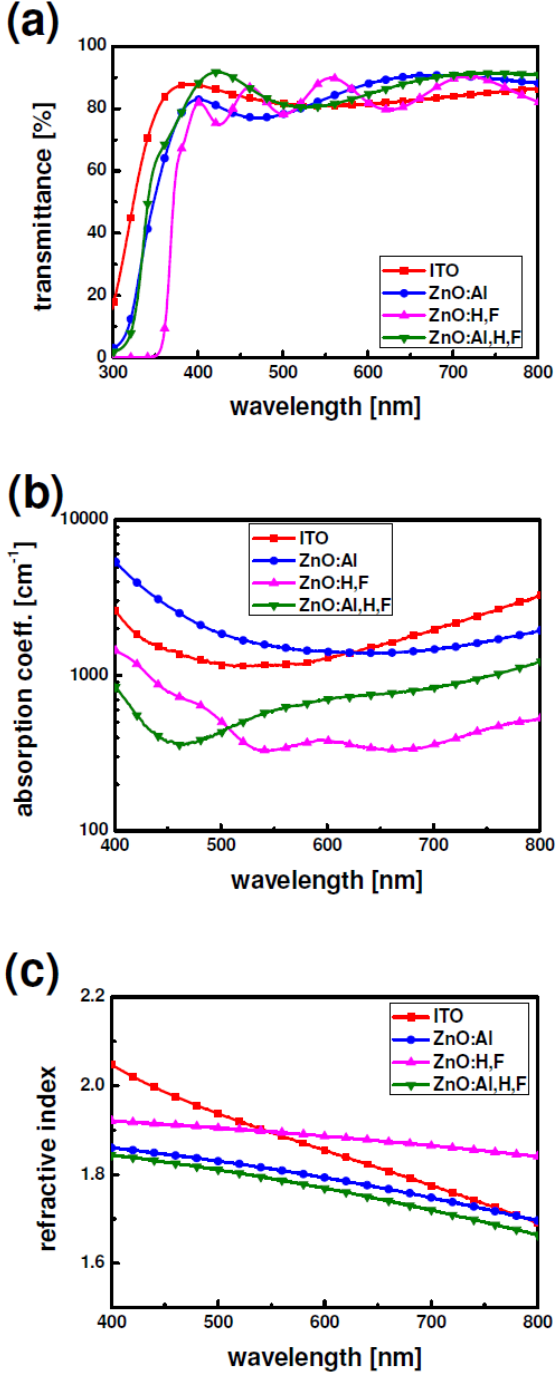

Figure 6.2. *(a) Transmittances (including the glass substrate), (b) absorption coefficients, and (c) refractive indices of TCO electrodes. ZnO films doped with hydrogen or fluorine show excellent optical properties such as higher transmittances, lower absorption coefficients, and lower refractive indices compared to ITO. All electrodes have roughly equal sheet resistances.*

Since the properties of OPV cells are often known to be influenced by the electrode surface microstructure, the surface characteristics of ZnO electrodes are investigated by atomic force microscopy (AFM). The AFM images show clear differences in the surface topography of the different kinds of TCO electrodes as shown in **Fig. 6.3**. The ITO film exhibits a very smooth surface with large, planar grains of several hundred nanometers in size. In contrast to ITO, a rough surface with fine granular structures is observed in the case of the ZnO:Al film. The ZnO:H,F and ZnO:Al,H,F films exhibit an even rougher surface along with round grains and densely distributed high peaks. These spontaneously formed nano-structures have a size of tens of nanometers. The molecular orientation, crystallinity, and quality of the donor/acceptor junction of OPV cells are significantly affected by an underlying layer (i.e. bottom electrode or buffer layer).[197-200] The photovoltaic performances are expected to be influenced by the observed differences in surface morphology, which will be discussed later.
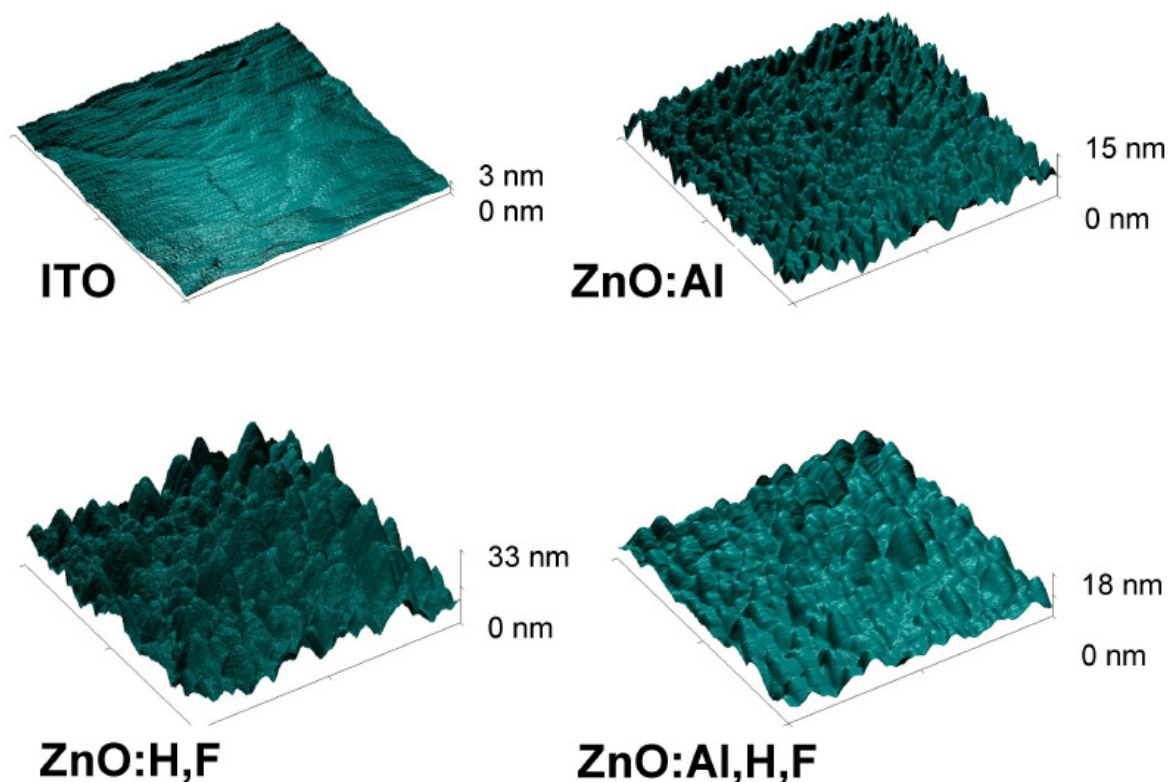

Figure 6.3. *Topography images of TCO electrodes (1×1 μm^2). ZnO films co-doped with hydrogen and fluorine show spontaneously textured rough surfaces while the ITO film has a very smooth surface.*

6.3. Application in OPV cells and OLEDs

- Fabrication of OPV cells

The layer sequence of OPV cells is as follows (bottom to top) : TCOs as bottom anodes / 1 nm p-type dopant NDP9 (Novaled AG) / 80 nm 10 wt.% NDP9 doped N,N'-((diphenyl-N,N'-bis)9,9,-dimethyl-fluoren-2-yl)-benzidine (BF-DPB) as a hole transport layer (HTL) / 5 nm fluorinated zinc phthalocyanine (F4-ZnPc) / 65 nm mixed F4-ZnPc : fullerene C_{60} (volume ratio of 1 : 1) heated at 100 $^{\circ}$C as a photoactive absorber layer / 30 nm C_{60} as an additional absorber layer and electron transport layer / 6 nm 4,7-diphenyl-1,10-phenanthroline (BPhen) as an exciton blocking layer / 100 nm Al as a top electrode. After device fabrication, all devices are encapsulated. The solar cell active areas are 4.0 ~ 5.7 mm^2 measured using an optical microscope. All organic materials except dopant are purified at least twice by vacuum gradient sublimation. NDP9 is used for a thermal stability, but behaves similarly to other dopants [201]. The solar cells are processed in our proven vacuum system, including reference samples, tracking of materials as well as frequent performance monitoring and comparisons, to ensure high reproducibility and significance of the samples made.

- Fabrication of OLEDs

The layer sequence for devices is as follows (bottom to top): ITO or ZnO:Al,H,F / 80 nm (N,N,N',N'-tetrakis(4-methoxyphenyl)-benzidine) (MeO-TPD) : 2,2'-(perfluoronaphthalene-2,6-diylidene)dimalononitrile (F6TCNNQ) (2 wt.%) / 10 nm 2,2',7,7'-tetrakis-(N,N'-diphenylamino)-9,9'-spirobifluorene (Spiro-TAD) / 8 nm 4,4',4''-tris(N-carbazolyl)-triphenylamine (TCTA) : tris(2-phenylpyridine)-iridium (Ir(ppy)$_3$) (8 wt.%) / 12 nm 1,3,5-tris(N-phenylbenzimidazole-2-yl)benzene (TPBI) : Ir(ppy)$_3$ (8 wt.%) / 10 nm bis(2-methyl-8-chinolinolato)-4-(phenyl-phenolato)-Aluminum-(III) (Balq2) / 55 nm 4,7-diphenyl-1,10-phenanthroline (BPhen) : Cs (1:1) / 200 nm Al.

- Results

Having investigated the TCO properties, we fabricate p-i-i (p-doped, intrinsic, intrinsic layer) type small molecule OPV cells, carefully optimized for high efficiency. As absorber layer, a fluorinated zinc phthalocyanine:fullerene (F4-ZnPc:C_{60}) bulk heterojunction is used. ZnPc and C_{60} are commonly used donor and acceptor materials in the small molecule OPV community. The F4-ZnPc used in this work is modified by fluorination, giving higher open circuit voltage (V_{OC}) compared to pure ZnPc as reported recently.[153] The blend layer is heated at 100 $^{\circ}$C for better crystallinity and nanomorphology, resulting in improved fill

factors (FF) and short circuit current densities (J_{SC}). The hole transport layer (HTL) is doped with a p-dopant and a very thin p-dopant layer is introduced at the interface between electrode and HTL to achieve an ohmic contact with a negligible hole extraction barrier, showing more efficient carrier transport properties.[6, 180] Thanks to the interface doping, the common problem of an energy level mismatch between highest occupied molecular orbital (HOMO) of the HTL and ZnO does not affect our system. This allows us to avoid PEDOT:PSS and the associated chemical instability in combination with the ZnO. An intrinsic C_{60} layer is deposited on the absorber blend layer for additional light absorption and electron transport. 4,7-diphenyl-1,10-phenanthroline (BPhen) is used as an exciton blocking layer to prevent exciton quenching and damage of cathode deposition. All OPV cells are fabricated in one run, enabling reliable comparison of the influence of electrodes. The devices are denoted as OPV$_X$, where the subscripts of X indicate the type of bottom electrodes used such as ITO, ZnO:Al, ZnO:H,F, and ZnO:Al,H,F.

The typical IV curves are shown in **Fig. 6.4 (c)**, and the resulting parameters are listed in **Table 6.3**. J_{SC} values in this work have been measured with a mask to minimize side effects for accurate results,[202] meaning that there is negligible waveguided light or extended electrode area by conductive transport layers. Despite the lower work functions of the ZnO series (4.3 eV ~ 4.5 eV) compared to ITO (4.7 eV) as shown in **Table 6.2**, using molecular doping in transport layers results in ohmic contacts and results in the same V_{OC} of 0.71 V without any injection problems for all devices. The power conversion efficiency (PCE) of the ITO reference device is 3.7 % with a J_{SC} of 9.6 mA/cm^2 and a FF of 54.6 %. It is observed that ZnO-based OPV cells exhibit higher J_{SC}, FF, and PCE compared to the reference ITO device. The OPV$_{ZnO:Al,H,F}$ cell exhibits a highest PCE of 4.4 % with a J_{SC} of 10.7 mA/cm^2 and a FF of 58.3 %, showing a great improvement of PCE by a factor of 1.2, when compared with the ITO-based device. To the best of our knowledge, this efficiency value as well as enhancement factor is the highest value reported for OPV cells with alternative electrodes.[199, 203] Alternative electrode-based OPV cells typically show lower or comparable PCEs to the ITO reference device but they do not significantly exceed it in literature.[113, 122, 126, 196, 199, 204] Especially replacing ZnO electrodes with ITO is far challenging for polymer solar cells based on PEDOT:PSS hole transport layers which show reduced PCEs compared to the ITO reference device.[70, 71, 204, 205] It is worth mentioning that a similar enhancement to our results is observed only for intentionally textured substrates for efficient light trapping prepared by lithography, laser structuring, or chemical etching process.[206-210]

External quantum efficiency (EQE) spectra of the different cells are shown in **Fig. 6.4 (d)**. The $OPV_{ZnO:Al,H,F}$ cell shows an enhanced EQE in almost the whole wavelength range of 400 ~ 700 nm, when compared with that of the OPV_{ITO} cell. This enhancement is especially pronounced at ~530 and 630 nm. This enhanced EQE is attributed to the low optical absorption loss of the ZnO electrode series with hydrogen and fluorine co-dopants. J_{SC} values calculated by integrating EQE data are consistent with those obtained from IV measurement as shown in **Table 6.3**. In addition, the lower refractive index of the ZnO:Al,H,F film (n~1.8, at 500 nm) compared to ITO (n~1.94, at 500 nm) is acting as improvement factor. The ZnO:Al,H,F film with lower refractive index is reducing the reflection of in-coming light at the interface of glass (n~1.5)/electrode, and the electrode/organic layers (n~1.8) due to good refractive index match.
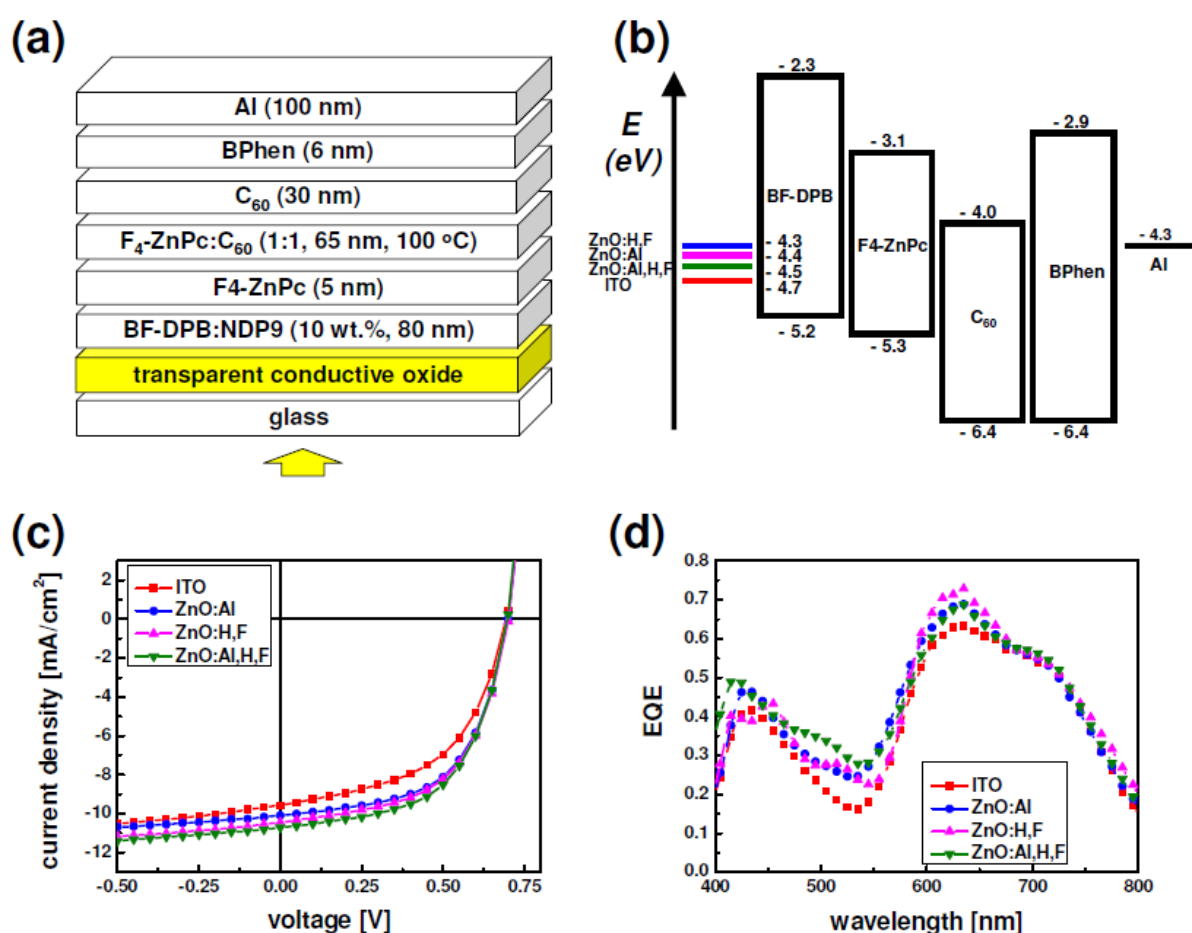

Figure 6.4. (a) Schematic of the structure, (b) energy level diagram, (c) IV curves, and (d) EQE spectra of OPV cells with different types of bottom electrodes such as ITO, ZnO:Al, ZnO:H,F, and ZnO:Al,H,F. Enhanced J_{SC} and EQE are observed for the $OPV_{ZnO:Al,H,F}$ cell due to excellent optical properties of the optimized bottom electrode.

OPV cells	V_{OC} [V]	J_{SC} [mA/cm^2]	FF [%]	PCE [%]	J_{SC} [mA/cm^2] from EQE
OPV$_{ITO}$	0.71	9.6	54.6	3.7	10.9
OPV$_{ZnO:Al}$	0.71	10.1	58.7	4.2	12.0
OPV$_{ZnO:H,F}$	0.71	10.5	57.6	4.3	12.1
OPV$_{ZnO:Al,H,F}$	0.71	10.7	58.3	4.4	12.5

***Table 6.3.** The characteristics of OPV cells with different types of bottom electrodes. The PCE of the OPV$_{ZnO:Al,H,F}$ cell is improved by a factor of 1.2 compared to that of the OPV$_{ITO}$ cell. The improved J$_{SC}$ and FF are attributed to the optical and morphological effects of the bottom electrode.*

The main differences between the ITO and ZnO electrodes used are the optical and morphological properties since the sheet resistances are kept at a similar level. At the major absorption peaks of F4-ZnPc (630 nm) and C_{60} (450 nm), the ZnO:Al,H,F film shows around 1.06 and 1.05 times higher transmittances than ITO, respectively. The J_{SC} of the OPV$_{ZnO:Al,H,F}$ cell is improved by a factor of 1.11 and the FF is also improved, compared to the ITO reference. Thus, the better transmission alone cannot fully explain the observed performance improvement in the ZnO-based OPV cells. Therefore, it is considered that a certain part of the improvement in OPV performance may stem from the surface topography. It is well known that the surface topography of electrodes and buffer layers plays a significant role in the performance of OPV cells.[116, 206, 211-215] Considering the improved FF as well as J_{SC} of the OPV$_{ZnO:Al,H,F}$ cell, it is expected that naturally structured ZnO electrodes collect charges more effectively than the flat ITO electrode, which might be due to the combined effects such as an increased contact area, shortened carrier transport distance, and desirable contact quality, enhancing J_{SC} and FF. Such an improvement of J_{SC} as well as FF by an introduction of rough metal oxide films has been reported by several groups recently.[206, 211-217] To investigate the morphological effect of the electrode topography on the device performance, AFM measurements are carried out on the top organic layers of the OPV cells (**Fig. 6.5**). It is noted that, even though relatively thick organic layers (~175 nm) are deposited on the bottom electrodes, the surface of the organic film is different and still reflects the effect of the original electrode topography. The organic surface of the ITO reference cell shows small grains with diameters of several tens of nanometers. In contrast, the OPV$_{ZnO:Al,H,F}$ cell shows large organic

structures. These results clearly demonstrate that the structures of the organic thin films and the back metal reflector are influenced by the original bottom electrode surface. Thus the nanostructure in the absorber blend (F4-ZnPC:C_{60}) and the adjacent (C_{60}) layers are probably changed. The same applies for the back electrode, which probably reflects more diffusively, due to the increased roughness.
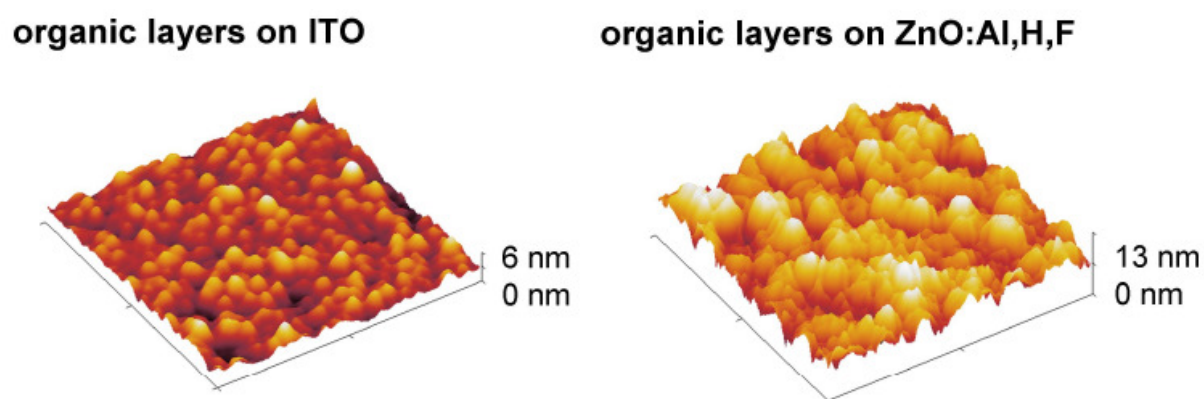

Figure 6.5. *Topography images (1×1 μm^2) of evaporated organic layers on ITO and ZnO:Al,H,F electrodes, showing different surface topographies, reflecting a different morphology caused by the underlying electrode surface structure.*

The outstanding optical properties of the ZnO:Al,H,F film are expected to improve the performance of OLEDs as well. Thus we fabricate phosphorescent green OLEDs based on ITO and ZnO:Al,H,F electrodes. **Figure 6.6 (c)** shows typical IVL curves for OLEDs. The IV behavior of both devices is nearly equal due to similar sheet resistance of electrodes. In addition, as observed for the solar cells, the work function difference of the electrodes barely affects the electrical performance of the OLEDs due to the use of doped HTLs as shown in the IV curves. For example, the onset voltages of both OLEDs are equal at 2.5 V. **Figure 6.6 (d) and (e)** show the EQE and luminous efficiency (LE) of OLEDs with respect to luminance. The OLED with ZnO:Al,H,F exhibits an enhanced EQE compared to the reference ITO-based OLED. The EQE of the ITO-based OLED is 9.1 % at a luminance of 1000 cd/m^2, while it is improved to 12.5 % with the OLED on ZnO:Al,H,F by a factor of 1.37. As the IV behavior for both devices is almost identical, it is clear that the enhancement is mainly attributed to the improvement of light out-coupling. A nearly matched refractive index between ZnO:Al,H,F and organic layers reduces the total internal reflection of light at the interface of electrode and organic layers. In addition, the lower optical losses of the ZnO:Al,H,F electrode allow to extract more light compared to ITO. Thus, the combined optical benefits of ZnO:Al,H,F enhance the performance of the OLEDs.
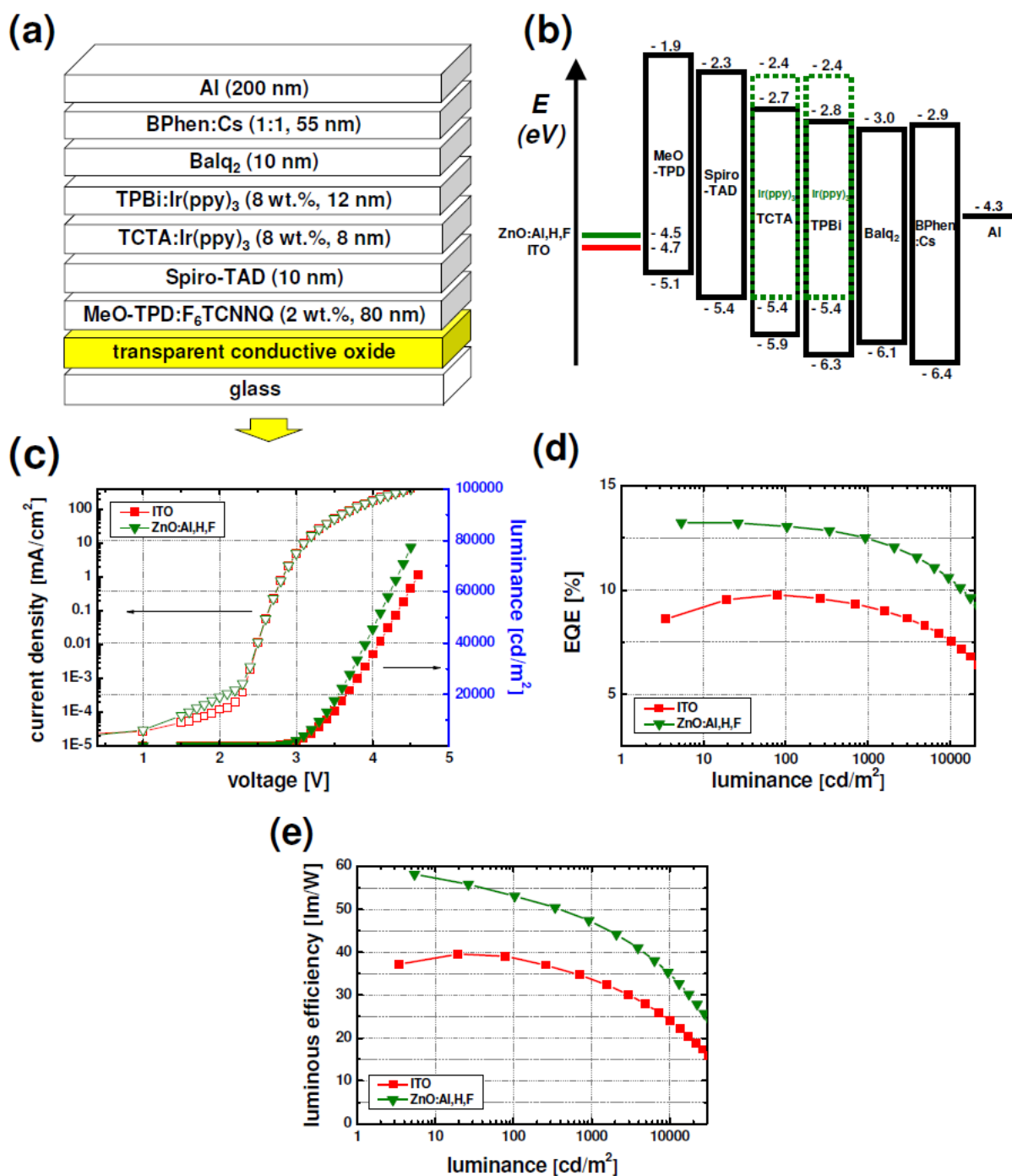
Figure 6.6. (a) Schematic of the structure, (b) energy level diagram, (c) IVL curves, (d) EQE, and (e) luminous efficiency versus luminance of OLEDs based on ITO or ZnO:Al,H,F electrodes. The OLED with ZnO:Al,H,F exhibits improved EQE and luminous efficiency.

In summary, ZnO thin films are successfully optimized by co-doping of hydrogen and fluorine dopants for high optical and electrical performance as electrode for ITO-free organic solar cells. The highly transparent ZnO electrodes with hydrogen and fluorine co-dopants lead to highly improved J_{SC} and FF of OPV cells. Due to combined optical and morphological

effects, caused by the naturally rough surface texture of the ZnO electrodes, a large improvement approaching 20 % is possible. The enhancement factor is among the highest values reported for ITO-free OPV cells. Furthermore, the application of the same, optically optimized ZnO electrodes is possible for OLEDs as well and shows an improved light extraction efficiency resulting from a reduction of wave-guided light and optical losses in the electrodes. Molecular doping in transport layers of the devices allows using the ZnO electrodes in OPV cells and OLEDs without any carrier injection/extraction problem or chemical instabilities.

Chapter 7. Laminated free-standing carbon nanotubes as a top electrode[*]

7.1. Introduction

In this study, we report on inverted semi-transparent small molecule n-i-p OPV cells with free-standing carbon nanotube (f-CNT) top electrodes. The top f-CNT electrodes are deposited on OPV cells using a room temperature orthogonal liquid solution assisted self laminating process, which is simple and damage-free for organic layers. The OPV cells with f-CNT top anode electrodes show very low leakage currents, high fill factors, and promising efficiencies, transparencies, and long-term stability. The OPV cells parameters are systematically studied, with a variation of p-doped hole transport layer (HTL) thickness adjacent to top f-CNT anodes. The optimal optical field distribution in these OPV cells is investigated by optical simulations based on the transfer-matrix formalism. These results show that f-CNT cells can serve as highly promising semi-transparent OPV cells.

Furthermore, to achieve low-cost or semi-transparent OPV cells, the compatibility and favourable combination between bottom and top contacts should be investigated. However, such a study about alternative electrode combinations is currently missing. In this work, we demonstrate semi-transparent or ITO-free small molecule OPV cells utilizing various bottom electrodes with either thin metal layers or laminated CNT top electrodes. The results of the electrode combinations can be a practical guidance for the consideration of electrodes in semi-transparent and low-cost ITO-free OPV cells with straightforward extension to flexible substrates.

7.2. Applications in transparent OPV cells

- Preparation of OPV cells with lamination process

The layer sequence for solar cells is inverted, as compared to usual direct OPV cells with top Al cathode, since it has a bottom indium tin oxide (ITO) cathode with n-doped electron transport layer (ETL) and a top f-CNT anode as follows (bottom to top): ITO as a bottom cathode / 10 nm tetrakis(1,3,4,6,7,8-Hexahydro-2H-pyrimido[1,2-a]pyrimidinato)ditungsten (II) ($W_2(hpp)_4$) doped C_{60} as an ETL / 30 nm C_{60} as an additional absorber layer and ETL / 30 nm mixed zinc phthalocyanine (ZnPc) : fullerene C_{60} (volume ratio of 1 : 2) as an photoactive absorber layer / X nm 10 wt.% 2,2'-(perfluoronaphthalene-2,6-diylidene)dimalononitrile (F6TCNNQ) doped N,N'-((diphenyl-N,N'-bis)9,9,-dimethyl-fluoren-2-yl)-benzidine (BF-DPB) as a hole transport layer (HTL) / 1 nm p-type dopant as a hole injection layer / a top anode. The stack is visualized in **Fig. 7.1 (a)**.

For the reference solar cell (Ag cell), the thickness of the HTL is 50 nm and a thin metal layer (Al 1 nm, Ag 14 nm) is evaporated as a top electrode. Subsequently, 60 nm of tris(8-hydroxy-quinolinato)-aluminum (Alq_3) is deposited on the top as a capping layer increasing the transparency of the Ag cell. The sheet resistance and transparency of this type of reference metal electrode are around 5 ohm/sq and 64.7 % (at 550nm, with Alq_3), respectively.

For the solar cells with the f-CNT (f-CNT cells), the HTL thicknesses are varied from 20 to 80 nm. The f-CNT sheets (sheet resistance : ~ 250 ohm/sq and transparency : ~ 38 % (at 550 nm)) are prepared from a multi-walled CNT forest produced by a chemical vapor deposition (CVD) process at the Alan G. MacDiarmid NanoTech Institute as described previously.[109] The as-prepared f-CNT sheets are directly deposited by manual lamination assembly on top of organic stacks in a nitrogen filled glove box without air exposure. Afterwards, the f-CNT cells are subsequently immersed into orthogonal liquid hydrofluoroether (HFE) for several seconds to densify the f-CNT sheets (from typically 15-20 micron wide aerogel to 50-100 nm f-CNT film) on top of the solar cells. As shown before, such densification significantly improves the f-CNT electrode performance by increased transparency and improved conductivity due to dense tube to tube interconnects without any device degradation.[218] The densified f-CNT sheet used in this study turns into an around 80 nm thick porous film. The solar cell active areas are 2.56 ~ 6.91 mm^2 measured using an optical microscope.

- Results

ZnPc : C_{60} bulk heterojunction based small molecule OPV cells with n-i-p configuration are fabricated with top f-CNT electrodes. A schematic drawing of the fabrication process for f-CNT cells, a photograph of the semi-transparent cell, atomic force microscopy (AFM), and scanning electron microscope (SEM) image of an f-CNT sheet on top of the device after densification are shown in **Fig. 7.1**. It is known that f-CNTs have predominant orientation with respect to the direction of drawing. Laminated nanotubes on the device keep their orientation, as visible in microscope images.[109] The averaged transparency of the f-CNT cell (HTL of 50 nm) in the visible region is about 27 % (see **Fig. 7.2**).
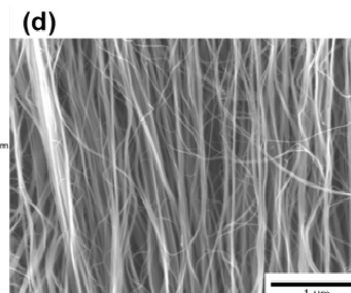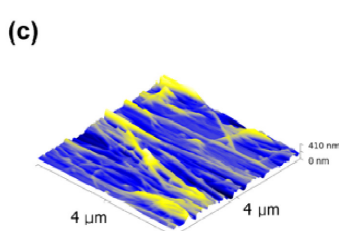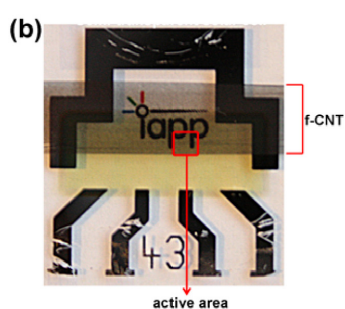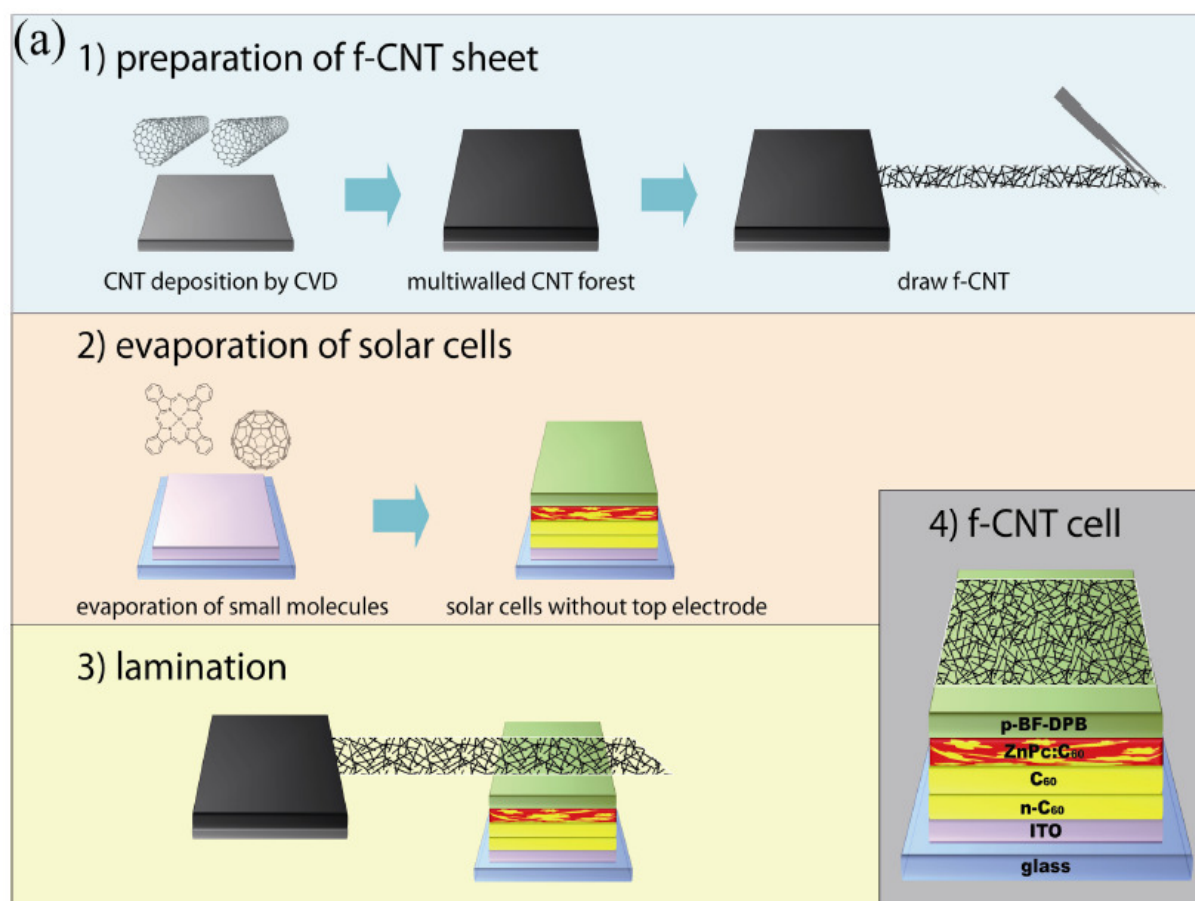
Figure 7.1. *(a) Fabrication process for f-CNT cell, (b) a photograph of f-CNT cell, (c) AFM (4 × 4 μm², and (d) SEM image of f-CNT sheet on the top of solar cell.*
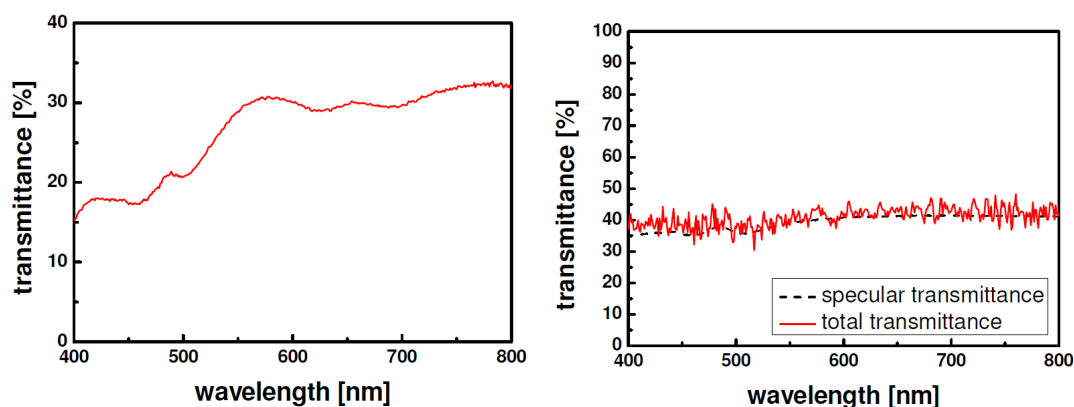

Figure 7.2. *(left) Transmittance of an f-CNT cell with an HTL thickness of 50 nm. (right) Specular and total transmittance of an f-CNT sheet on glass.*

Figure 7.3 shows typical current-voltage (*I-V*) characteristics of OPV cells as a function of the different HTL thickness and illumination from bottom (ITO side) and top (f-CNT side). The characteristic values of all devices are shown in **Table 7.1**. A thin metal layer (Al 1 nm/Ag 14 nm) is employed as the top electrode for the reference cell (Ag cell), using a similar stack to that reported for the semi-transparent cells by Meiss et al.[219] They showed optimized semi-transparent OPV cells with thin Ag layer with power conversion efficiencies (PCE) up to 2.2 %. The bottom illuminated Ag reference cell in our experiment shows a PCE of 1.9 % (short circuit current (J_{SC}) = 5.6 mA/cm², fill factor (FF) = 61.3 %, and open circuit voltage (V_{OC}) = 0.57 V). All f-CNT cells show high FFs (58 ~ 59 %) comparable to that of the reference Ag cell but somewhat lower J_{SC}. The highest observed PCE of f-CNT cells is 1.5 % with a J_{SC} of 4.7 mA/cm² for an HTL thickness of 20 nm and bottom illumination. With top illumination, the f-CNT cell with an HTL thickness of 50 nm shows a PCE of 0.9 % and a FF of 59.4 %, comparable to that of the Ag cell (PCE of 1.0 %, FF of 60.4 %). All f-CNT cells show very low leakage current, showing saturation factors [$J(-1 V)/J_{SC}$] below 1.2, which are even lower than those of highly optimized ZnPc : C_{60} bulk heterojunction OPV cells[130, 220]. This result indicates that neither the lamination process of top f-CNT sheets nor the densification in orthogonal hydrofluoroether (HFE) fluid cause any sizable shunt paths in the device. Electrical shorts of OPV cells caused by a rough CNT surface is a very common problem for devices with CNT electrodes, which is typically solved by smoothing planarization layers such as PEDOT:PSS[112, 117], which are not applied here.
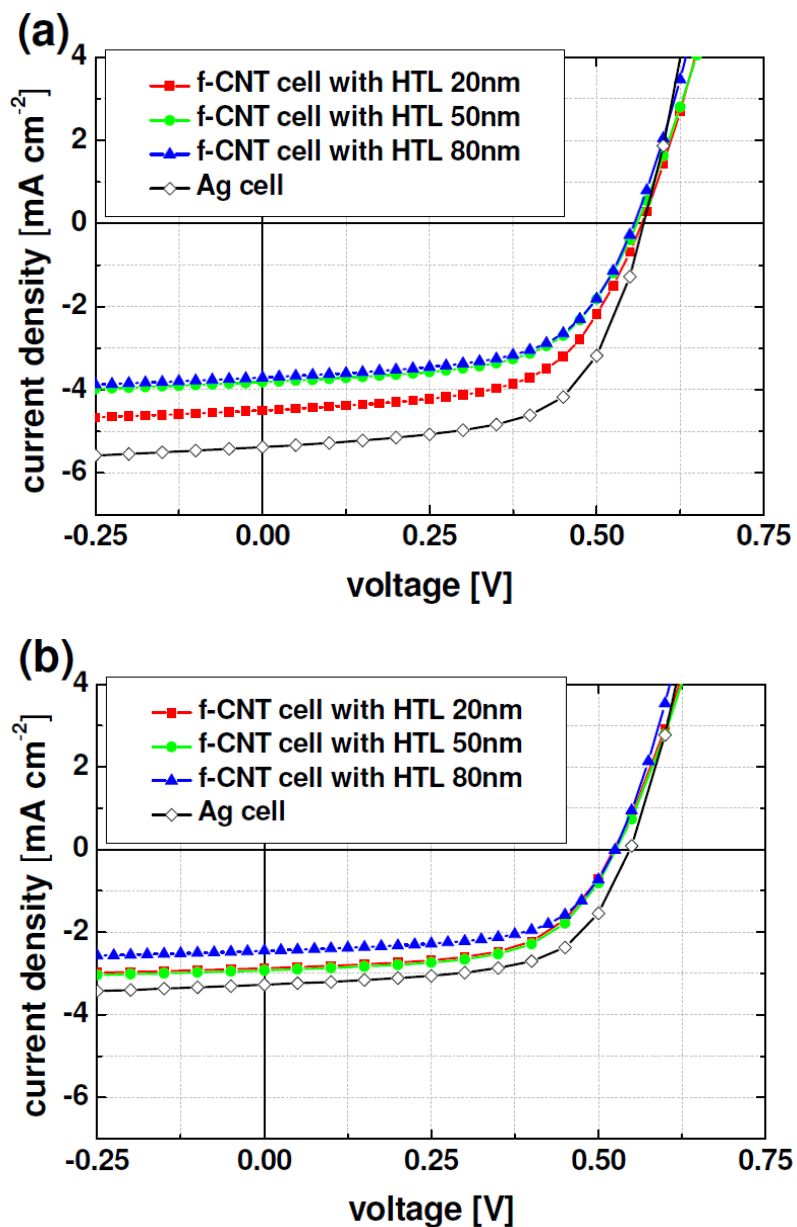
Figure 7.3. *I-V characteristics of Ag reference cell and f-CNT cells with different HTL thicknesses (20, 50, and 80 nm) during (a) bottom and (b) top illumination.*

The high FFs as well as low leakage currents, observed for all f-CNT cells, with both bottom and top illumination, indicate four points: (i) f-CNT sheets are uniformly deposited on all devices without major mechanical deviations. (ii) The conductivity of f-CNT is sufficiently high for the top electrode not to cause a large loss in photo-generated current. (iii) No charge carrier extraction barriers are formed at the f-CNT/organic interfaces. (iv) The rough f-CNT surface does not cause significant structural defects on the underlying organic layers during deposition. Therefore, the lower J_{SC} of the f-CNT cells compared to the Ag cell is attributed mostly to lower light absorption in the bulk heterojunction. Considering the important role of the top electrode, which reflects unabsorbed light back to the absorber layer, more reflective

115

thin Ag electrode enables the Ag cell to generate more photo-current than the f-CNT cell when illuminated from the bottom (ITO) side. However, during top illumination, low reflectivity of the ITO electrode leads to a negligible and equal reflection for both cells, therefore only a small performance difference between the Ag cell and the f-CNT cells is observed, which can be attributed to different transmission properties (PCE and J_{SC}, Ag cell : 1.0 %, 3.2 mA/cm^2, f-CNT cell : 0.9 %, 2.8 mA/cm^2, respectively). Generally, the lower J_{SC} for top illumination, compared to bottom illumination is attributed to a lower transparency of the top electrodes than the bottom electrodes and the weak reflection at the ITO interface. We believe that further enhancement of the conductivity and transparency of CNT networks by optimized synthesis process and other means enables further improvements in efficiency and transparency of the f-CNT cell. In fact, coating CNTs by very thin metal layers (Au or Al) of ~ 30 nm changes significantly sheet resistance of highly transparent MWCNTs bring it down to 20-30 ohm/sq while transparency is still quite high.

It is well known that tuning an optical field distribution in devices is of great importance for optimization of solar cells stack. In our experiment, the J_{SC} of f-CNT cells increases 3.7 to 4.5 mA/cm^2 with decreasing HTL thickness from 80 to 20 nm, when illuminated from bottom, showing the effect of an optical spacer in front of the f-CNT electrode. To continue the investigation of the thickness effect on J_{SC}, or any interactions between CNT and absorber layer, the HTL thickness is further decreased down to 0 nm, as shown in **Fig. 7.4**. The generally lower FF and PCE compared to the previous results are caused by more resistive f-CNT sheets used in this experiment. It is shown again that the J_{SC} strongly depends on the thickness of the HTL when illuminated from bottom. With decreasing HTL thickness from 50 to 10 nm, J_{SC} increases from 3.2 to 4.0 mA/cm^2. The enhanced external quantum efficiency (EQE) over the complete wavelength range for f-CNT cells with thinner HTL demonstrates the effect of HTL thickness during bottom illumination, as shown in the insets of **Fig. 7.4**. In contrast, all top illuminated f-CNT cells show similar J_{SC} and EQE with respect to HTL thickness except for the HTL of 0 nm. The poor performance of the cells without HTL is attributed to the absence of electron blocking effect and damage of the absorber layer.
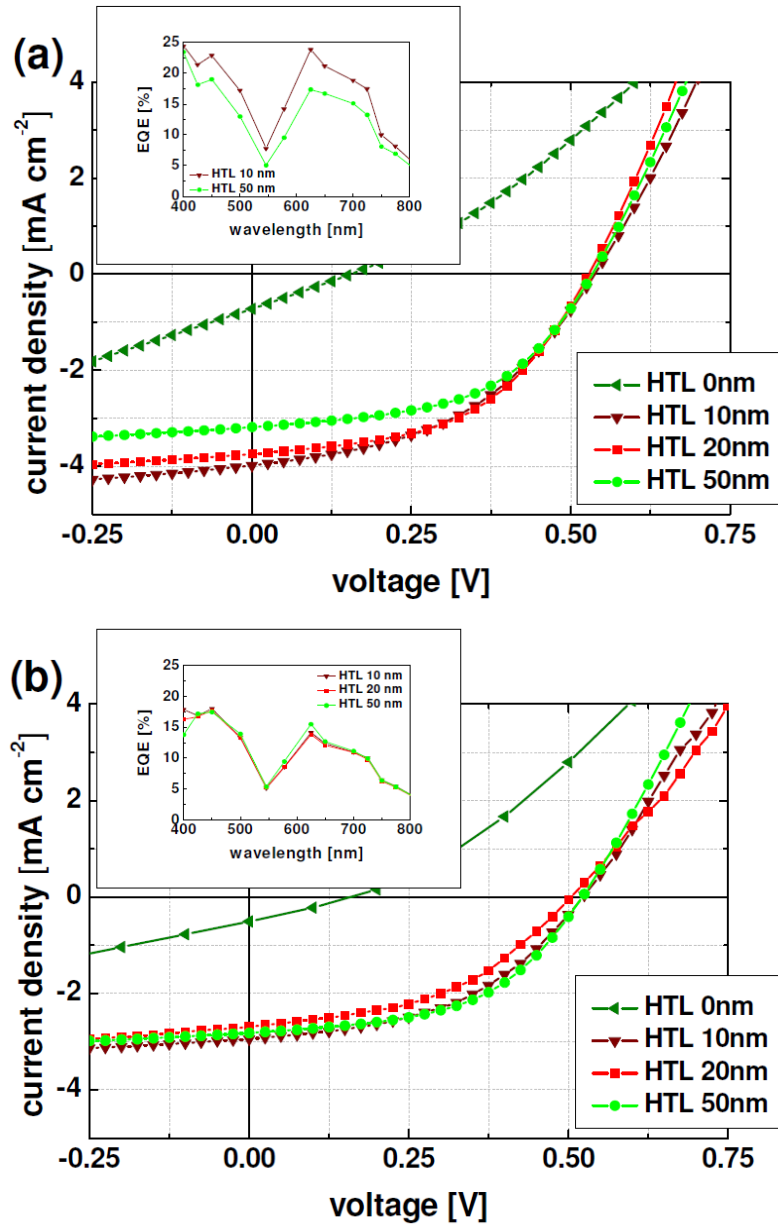
Figure 7.4. *I-V characteristics of f-CNT cells with different HTL thicknesses (0, 10, 20, and 50 nm) during (a) bottom and (b) top illumination. Inset shows EQE results of f-CNT cells.*

Optical simulations for f-CNT cell series with HTL thicknesses of 20, 50, and 80 nm are carried out to investigate the optical field effect with respect to the HTL thickness. **Figure 7.5** shows the absorbed photon rates in the f-CNT cells along the device configurations. It is shown that thinner HTL thicknesses lead to a strong increase in the absorbed photon rate of f-CNT cells in the bulk heterojunction region when illuminated from bottom. Therefore, highly enhanced J_{SC} for thinner HTLs is mainly attributed to the improved photon absorption in the bulk heterojunction. These results show that the maximum optical field intensity for bottom illuminated f-CNT cells is properly located at the bulk heterojunction absorber layer when the HTL thickness is around 20 nm, well consistent with the experimental results. In contrast, top

illuminated f-CNT cells with all different HTL thicknesses exhibit similar absorbed photon rates for all devices, showing small influence of the HTL thickness on J_{SC}. The HTL does not serve as an optical spacer in these OPV cells due to large optical absorption of the top f-CNT electrode and the reversed illumination conditions.
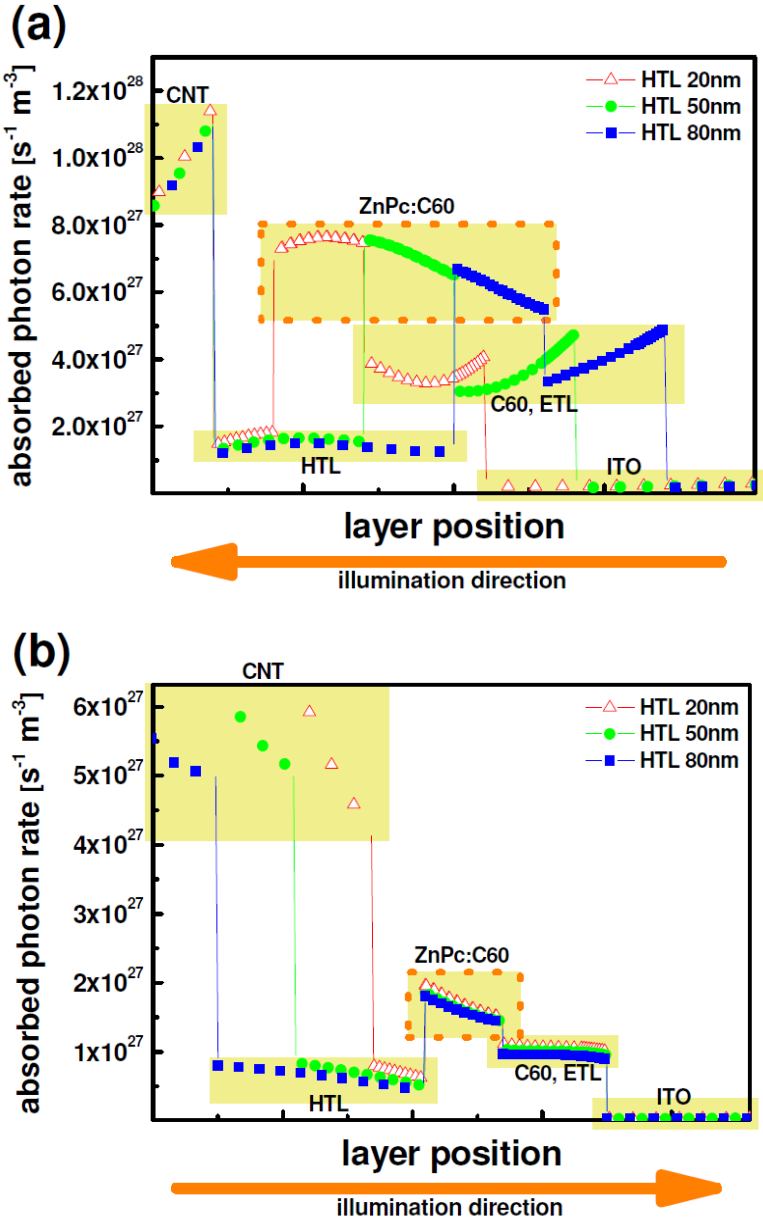

Figure 7.5. *Simulated absorbed photon rates profile of f-CNT cells with different HTL thicknesses (20, 50, and 80 nm) during (a) bottom and (b) top illumination under an AM 1.5G illumination condition.*

Figure 7.6 shows the simulated optical field distribution for f-CNT cells under bottom illumination. It is shown that the highest intensity optical field is properly situated in the absorber layer for the major absorption peaks of ZnPc (630 nm) and C_{60} (450 nm) of f-CNT

118

cells with 20 nm HTL. On the other hand, relatively low field intensities dominate the absorption area of an f-CNT cell with an HTL of 80 nm. These simulated results clearly demonstrate the effect of HTL thickness on J_{SC}, indicating that the optimization of optical field geometry of devices is quite important to employ a top electrode for efficient semi-transparent OPV cells. It is shown that the optimization of spacer layer thickness remarkably enhances J_{SC} with negligible ohmic losses, because of highly transparent and conductive nature of a doped organic spacer layer [55, 221]. Our results demonstrate that the geometry of semi-transparent OPV cells, including a porous, laminated top electrode, can be optimized by using conventional transfer-matrix theory, assuming top electrodes as a homogeneous layer without optical scattering.
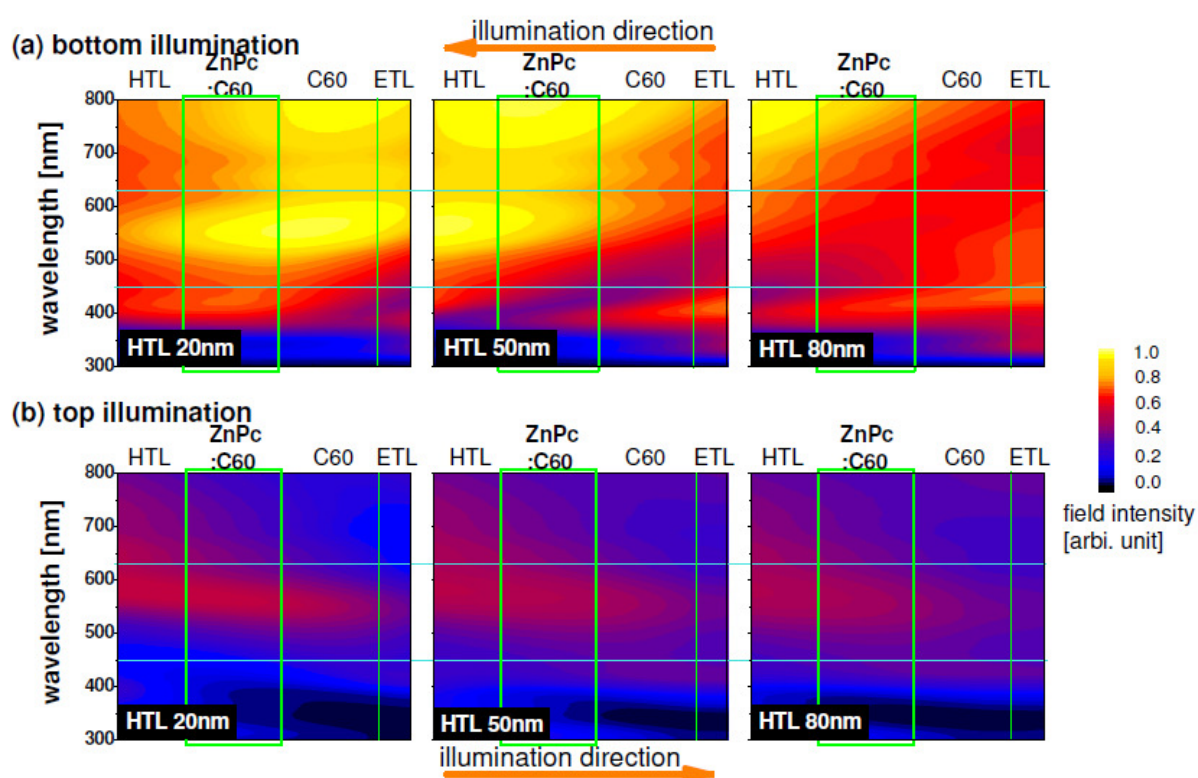

Figure 7.6. *Simulated optical field distributions in f-CNT cells with respect to different HTL thicknesses of 20 nm (left), 50 nm (middle), and 80 nm (right) when illuminated from (a) bottom and (b) top. The interfaces of layers are shown as vertical lines. The major absorption peaks of ZnPc (630 nm) and C_{60} (450 nm) are shown as horizontal lines. f-CNT and ITO electrodes are omitted for better visibility.*

It should be noticed that 3-D charge collection by highly porous f-CNT electrodes found earlier to increase the photo-current in polymeric OPV cells does not play an important role in our present n-i-p devices: the liquid solution assisted lamination process does not cause

significant protrusion of CNT nano-leads into HTL and photoactive layer, while showing very low leakage current as well as high FF due to low manufacturing defects. It is expected that creating architectures with highly porous CNTs protruding into photoactive layers assisted by additional pressure during the lamination process will further enhance performance by the effects of 3-D collection by suppressed charge recombination and transport in built-in electrical fields, strongly enhanced by tips and sides of CNT. The f-CNT cell with highly transparent and conductive CNT electrode with larger porosity will demonstrate this effect of enhanced charge collection at higher overall transparency, which will become particularly important for tandems. The application of f-CNT cells with different transparency and porosity in parallel type versus in series tandem type will be described separately.

Ageing measurements are carried out to investigate the stability of OPV cells with respect to the different kind of top electrodes. The encapsulated devices are illuminated with white LEDs at the intensity of 3 suns (Ag cell : 297 mW/cm^2, f-CNT cell : 312 mW/cm^2) and heated to ~ 50 °C for acceleration of ageing speed. The normalized PCE, FF, J_{SC}, and V_{OC} for OPV cells are shown in **Fig. 7.7**. The Ag cell shows a PCE decay of ~ 6 % after 700 hours. In contrast, the f-CNT cell exhibits more stable performances than the Ag cell, showing a PCE decay of only 3 % after ~ 700 hours. Especially the FF of the f-CNT cell is very stable, retaining its initial value, while that of the Ag cell keeps decreasing, indicating that the degradation of FF for f-CNT cell is almost free from oxidation and deterioration of the top electrode, which directly affect the device degradation reported by Voroshazi et al. [222] and is a common issue for thin film metal electrodes. These results suggest that the f-CNT devices have superior stability compared to the devices because of the metal-free electrodes concept.
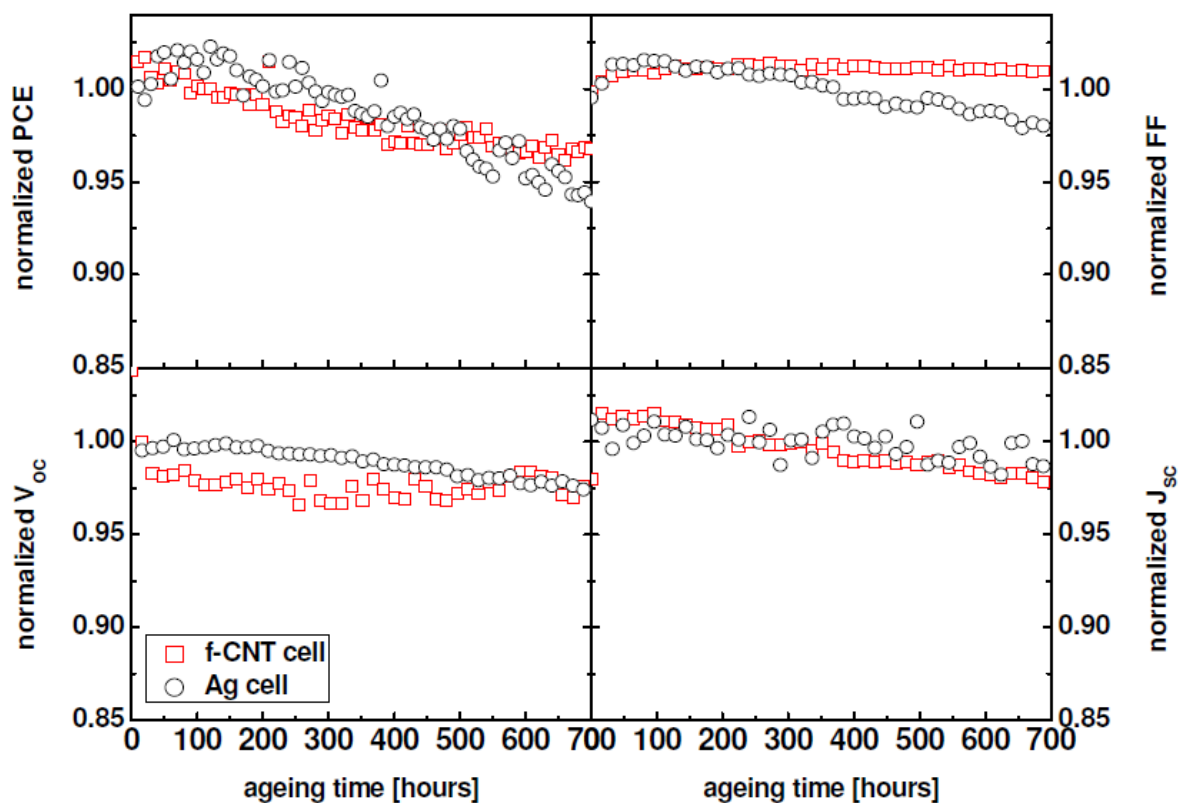
Figure 7.7. *Ageing characteristics of encapsulated OPV cells with an f-CNT or a thin metal top electrode, illuminated by white LEDs equivalent to ~ 3 suns at the temperature of ~ 50 °C .*

In summary, f-CNT top electrodes have been successfully adopted to semi-transparent OPV cells. The fabricated devices show relatively high FFs of up to 60 % and competitive efficiencies of up to 1.5 %. All devices show very low leakage currents without any additional smoothing layers. The metal electrode-free f-CNT cell show better long-term stability compared to the device having an oxidative metal electrode. These results indicate homogeneous and damage-free application of the f-CNT membrane despite of its high roughness and the delicate interface of the device. Optimization of the HTL thickness as optical spacer can control the field distribution in devices, which remarkably improves the efficiency of f-CNT cells. These results illustrate the feasibility of applying transparent f-CNT top electrodes with their unique properties as charge collecting electrodes for large area and efficient semi-transparent OSCs using a simple and reliable process of lamination of free-standing CNT sheets.

	V_{OC} [V]	J_{SC} [mA/cm^2]	FF [%]	PCE [%]	$J(-1\ V)/J_{SC}$
bottom illumination					
f-CNT cell with HTL 20 nm	0.57	4.5	58.2	1.5± 0.03	1.12
f-CNT cell with HTL 50 nm	0.56	3.8	59.5	1.3± 0.04	1.15
f-CNT cell with HTL 80 nm	0.56	3.7	59.4	1.2± 0.03	1.17
Ag cell	0.57	5.4	61.3	1.9± 0.09	1.14
top illumination					
f-CNT cell with HTL 20 nm	0.52	2.8	59.1	0.9± 0.08	1.12
f-CNT cell with HTL 50 nm	0.53	2.8	59.4	0.9± 0.06	1.13
f-CNT cell with HTL 80 nm	0.53	2.4	60.7	0.8± 0.05	1.17
Ag cell	0.55	3.2	60.4	1.0± 0.04	1.19

Table 7.1. The characteristics of semi-transparent OPV cells with different HTL thickness when illuminated from bottom and top directions, which were measured under an AM 1.5G illumination and normalized to 100 mW/cm^2. The experiments were reproduced at least three times, with no relevant deviation, the measurement ranges are given in the efficiency column.

7.3. Comparison of various bottom and top electrodes

In this study, we investigate the combination of various bottom and top electrodes for semi-transparent and ITO-free OPV cells.

- Preparation of OPV cells

Silver (Ag), ITO, PEDOT:PSS, and AgNW are prepared as bottom electrodes. Ag 100 nm is deposited on glass by vacuum thermal evaporation as opaque reference. PEDOT:PSS

(PH1000) mixed with 6 vol.% ethylene glycol is spun onto glass (1500 rpm, 30s) and subsequently annealed at 120 °C in air. AgNWs are prepared by a dip-coating process in AgNW solutions with an average nanowire length of several micrometers, and a diameter of about 60 nm. More details about the fabrication methods are given elsewhere.[223] The AgNWs are subsequently coated with PEDOT:PSS for flattening of the surface roughness. The peak height of AgNWs reduces by half after the PEDOT:PSS coating. Small molecule layers are thermally evaporated onto the bottom electrodes in a high vacuum chamber. As a HTL, 30 nm thick 10 wt.% NDP9 (Novaled AG) doped N,N'-((diphenyl-N,N'-bis)9,9,-dimethyl-fluoren-2-yl)-benzidine (BF-DPB) is deposited on the bottom electrode. Zinc phthalocyanine (ZnPc) and fullerene C_{60} are co-evaporated at the substrate temperature of 104 °C with a ratio of 1:1 as 55 nm thick absorber layer. 10 nm thick C_{60} is followed as an additional absorber and electron transport layer (ETL). 3 wt.% $W_2(hpp)_4$ doped C_{60} (10 nm) is evaporated as an electron transport layer. The devices are denoted as OPV_{X_Y}, where the subscripts of X indicate the type of bottom electrodes and Y is top electrodes.

Finally, thin silver layers (t-Ag) or free-standing carbon nanotubes (f-CNT) sheets are deposited as transparent electrodes on top of the devices. 1 nm thick Al and 14 nm thick Ag are thermally evaporated in the vacuum chamber as $OPV_{X\_t\text{-}Ag}$ top contact. The thin Al layer serves as a surfactant layer for the morphological improvement of the following Ag layer.[134] The f-CNT sheet is laminated on top of the organic layers in a nitrogen filled glove box without air exposure by manual assembly as a top contact for $OPV_{X\_f\text{-}CNT}$. For densification of the f-CNT sheets, the devices are subsequently immersed into the orthogonal liquid hydrofluoroether (HFE) for several seconds. The active areas of $OPV_{X\_t\text{-}Ag}$ and $OPV_{X\_f\text{-}CNT}$ are 5.8 ~ 6.8 mm^2 and 1.3 ~ 1.5 mm^2, respectively, measured using an optical microscope.

- Results

Small molecule OPV cells with ZnPc : C_{60} bulk heterojunction (p-i-n structure) are prepared by vacuum thermal evaporation. Scanning electron microscope (SEM) and atomic force microscopy (AFM) images of the electrodes used in this experiment are shown in **Fig 7.8 (a)**. The f-CNT sheet shows well-oriented CNT networks with individual tube diameters of 10 ~ 30 nm, which cause a high surface roughness. The AgNW electrode consists of nanowires with about 60 nm diameter and good wire-wire junctions, resulting in high conductivity electrodes and an even larger surface roughness, compared to the f-CNT electrodes. PEDOT:PSS has a granular surface with an average grain size of 30 ~ 50 nm and a root-

mean-square roughness (RMS) of around 1.6 nm, which is measured in an area of 1×1 μm^2. ITO exhibits a polycrystalline structure with grains of several hundred nanometers in size having a very smooth surface (RMS : 0.42 nm). In **Fig. 7.8 (b)**, the stack of p-i-n OPV cells on various electrodes are shown.
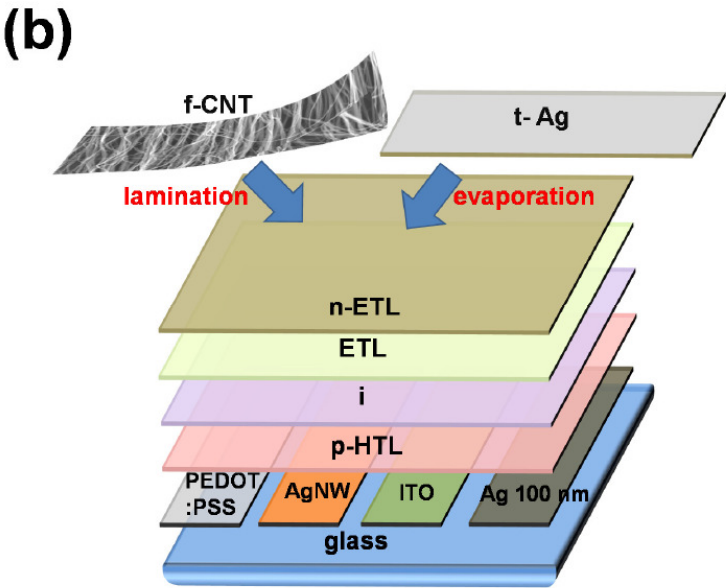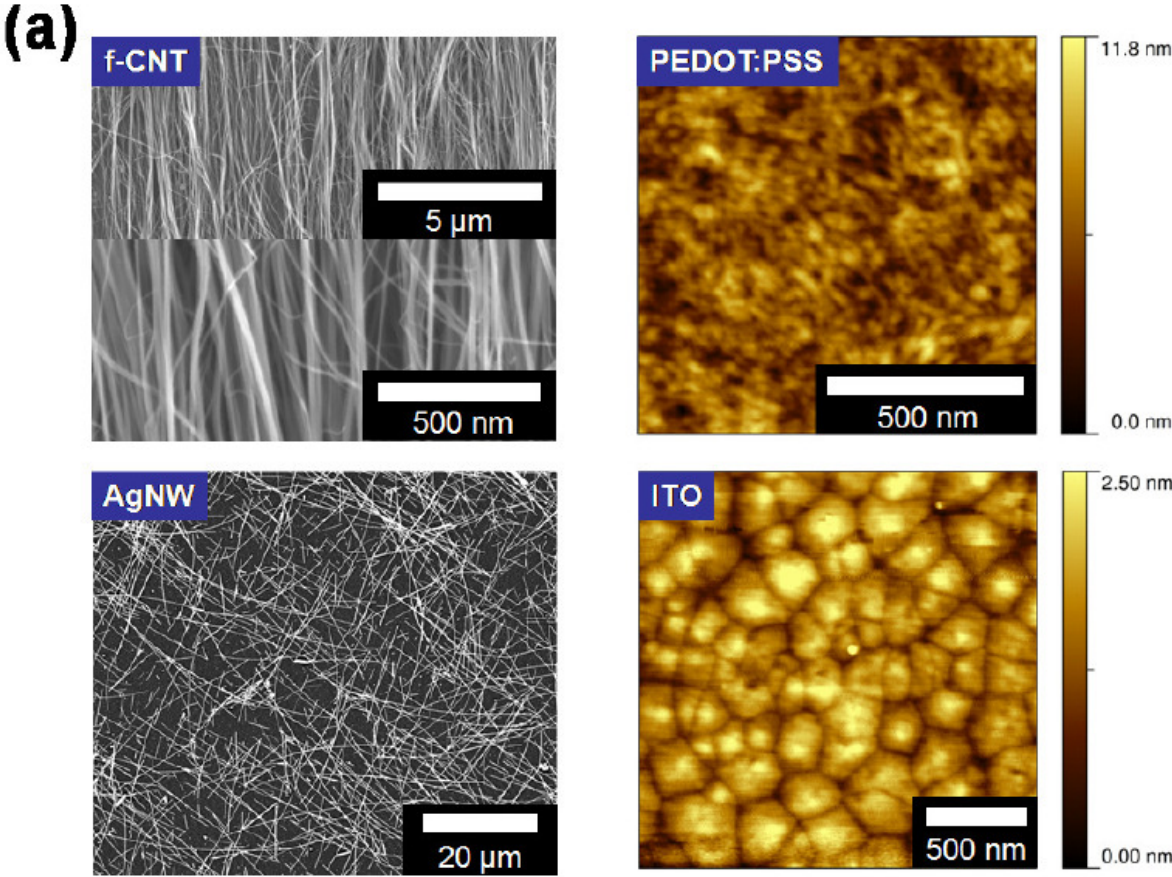
*Figure 7.8. (a) SEM and AFM images of the f-CNT sheet, AgNW, PEDOT:PSS, and ITO, (b) p-i-n layer stack of the small molecule OPV cells with various bottom electrodes and top electrodes. *The AgNW electrode actually is a hybrid electrode and includes an additional layer of PEDOT:PSS, which is spin-coated on the AgNW film for surface planarization.*

The transmittances of the conductive electrodes are shown in **Fig. 7.9** and summarized in **Table 7.2** along with the respective sheet resistance values. The transmittances of bottom electrodes are in the range of 83 ~ 87 % at a wavelength of 550 nm. The f-CNT and t-Ag employed as top electrodes have lower transmittances (41 ~ 58 %) in comparison to the bottom electrodes used.
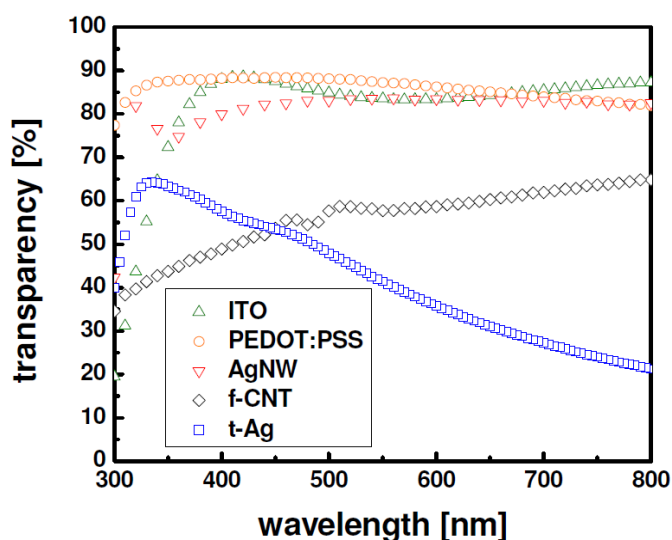

*Figure 7.9. Transmittances (including the glass substrate) of the conductive electrodes. *The t-Ag film contains a thin 1 nm Al layer beneath.*

Figure 7.10 shows typical current-voltage (I-V) characteristics of OPV cells with different kinds of bottom and top electrodes. All devices are fabricated at the same time in one run, ensuring comparability. Similar short circuit current density (J_{SC}) values of around 8.5 mA/cm^2 are observed for OPV$_{PEDOT:PSS\_t-Ag}$, OPV$_{ITO\_t-Ag}$, and OPV$_{AgNW\_t-Ag}$ cells. OPV$_{ITO\_t-Ag}$ and OPV$_{AgNW\_t-Ag}$ cells are comparable in power conversion efficiencies (PCE) of 2.2 and 2.1 %, respectively. Despite the rough surface of the AgNW electrodes, which can cause severe leakage currents, the OPV$_{AgNW\_t-Ag}$ cell shows a higher fill factor (FF) of 50.6 % compared to the OPV$_{ITO\_t-Ag}$ cell (48.9 %), which is attributed to the lower sheet resistance of the AgNW electrode. The combination of bottom AgNW and top t-Ag is regarded as a promising combination to achieve a high PCE with both semi-transparent and ITO-free

properties. The OPV$_{\text{PEDOT:PSS\_t-Ag}}$ cell shows a decent efficiency of 1.9 %, but lower FF of 42 % compared with other devices in OPV$_{\text{X\_t-Ag}}$ series. This is attributed to the more resistive electrode, which results in higher series resistance of the devices. One way to improve the PEDOT:PSS based cell to become comparable to the ITO based cell is to remove residual water and excess PSS. The residual water in the polymeric electrode significantly deteriorates the performance of devices as reported in chapter 5. In addition, the solvent post-treatment process for PEDOT:PSS can improve the device performance and lifetime by removal of excess hygroscopic PSS.[180] The OPV$_{\text{Ag\_t-Ag}}$ cell exhibits a higher FF of 52.4 % but a lower J_{SC} of 7.5 mA/cm^2 compared to other cells in the OPV$_{\text{X\_t-Ag}}$ series. The lower J_{SC} is attributed to less absorbed photons in the absorber layer because of the lower transmittance of metal thin-film. In case of OPV$_{\text{Ag\_t-Ag}}$ cell, the light is illuminated from the top t-Ag electrode which has lower transmittance (41 %) compared to other bottom electrodes.

electrodes	transmittance [%] (550 nm)	sheet resistance [ohm/sq]
ITO	84	30
PEDOT:PSS	87	155
AgNW	83	10
f-CNT	58	360
t-Ag	41	5

*Table 7.2. Transmittances and sheet resistances of the transparent conductive electrodes used in this work. *The t-Ag film contains a thin 1 nm Al layer beneath.*

The difference of PCEs according to the illumination direction for semi-transparent OPV cells was studied in the previous section. The OPV$_{\text{ITO\_t-Ag}}$ cell illuminated from bottom showed a 1.9 times higher PCE than for the top illuminated case. When comparing opaque (100 nm Ag on top) and semi-transparent (14 nm Ag on top) OPV cells fabricated with a similar stack based on ZnPc : C$_{60}$ as in this experiment, the J_{SC} and PCE of semi-transparent device were around 70 % and 67 %, respectively, of that of the opaque device. Open circuit voltages and FFs of both devices were rather similar. It is expected that the introduction of an organic capping layer for optical in-coupling on t-Ag can further improve the efficiency of the device as reported by Meiss et al., who demonstrated that an organic capping layer remarkably

improves the efficiency of OPV cells from 1.27 % to 1.84 %, which is attributed to an enhancement of light absorption.[130]

The OPV$_{X\_f\text{-}CNT}$ series exhibits worse device performance compared to the series of OPV$_{X\_t\text{-}Ag}$ cell as shown in **Fig. 7.10 (b)**, which is mainly due to the low conductivity of the f-CNT electrodes. The OPV$_{Ag\_f\text{-}CNT}$ cell shows the highest PCE of 1.5 % among the OPV$_{X\_f\text{-}CNT}$ series. It is interesting to note that a significant electrical short is not observed in the OPV$_{X\_f\text{-}CNT}$ series despite the very thin transport layers of 20 nm between the absorber layer and the rough f-CNT top electrode. It is widely known that a smoothing buffer layer such as PEDOT:PSS is essential for most of devices using rough CNT electrodes to prevent electrical short.[111-113, 116, 117, 224] OPV cells with more conductive and less transparent f-CNT top electrodes than the one used in this study show equally low leakage currents, as shown in the previous section, indicating that the rough f-CNT top electrode does not cause significant damage of underlying organic layers. The trade-off between conductivity and transmittance of CNT networks affects the J_{SC} and FF of the devices. Therefore, balancing the electrical and optical properties of CNT networks can further improve the performance of OPV$_{X\_f\text{-}CNT}$ cells.
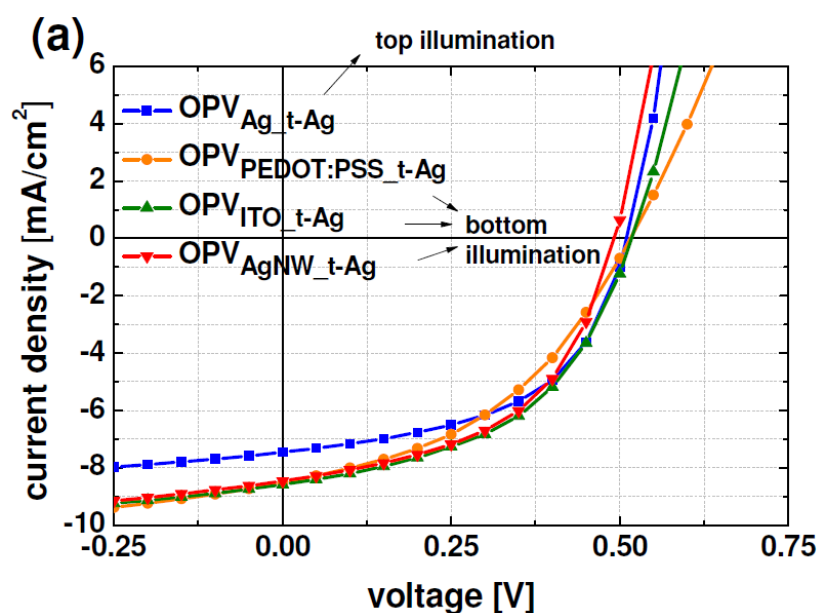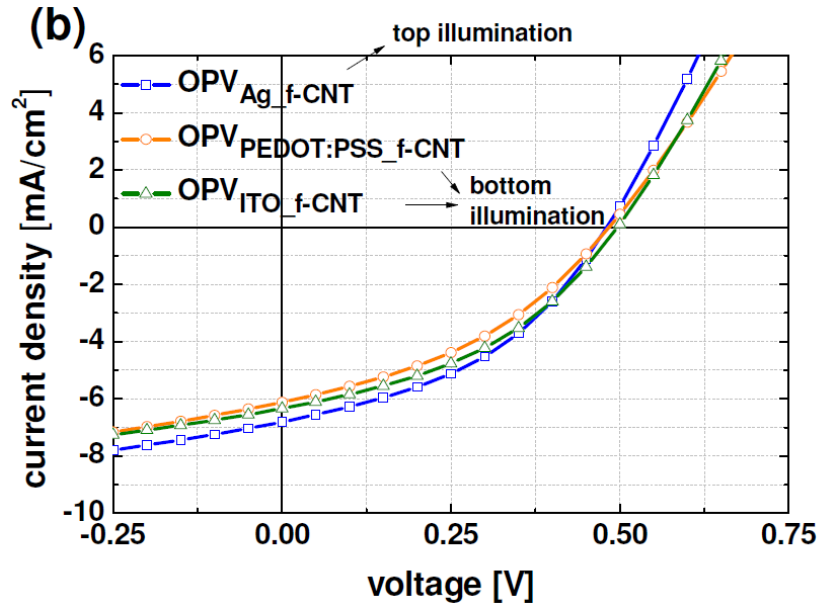
Figure 7.10. *I-V characteristics of the series of (a) OPV$_{X\_t-Ag}$ and (b) OPV$_{X\_f-CNT}$. *The top illuminated OPV$_{Ag\_t-Ag}$ cell exhibits lower J$_{SC}$ due to lower transmittance of t-Ag compared to that of other bottom electrodes.*

The light illumination intensity (I$_{sun}$) dependence of various kinds of OPV cells is shown in **Fig. 7.11**. Measured data is normalized due to disparity of PCE values from different OPV fabrication runs in this measurement. Each device shows clearly different light dependence behaviour. It is notable that the PCE of OPV$_{Ag\_f-CNT}$ cell continuously increases with decreasing I$_{sun}$ from 100 to 2 mW/cm^2, which results in an enhancement of 61 %. In contrast, most other devices show peak PCEs at intermediate I$_{sun}$ and decrease down again at low I$_{sun}$. It is well known that J_{SC} is nearly linear dependent on I$_{sun}$, showing a power law dependence, $J_{SC} \propto I_{sun}{}^{\alpha}$, with α being close to 1. Extracted α values, fitted to the power law relationship, are shown in **Table 7.3**. It is observed that various electrode combinations give remarkably different α. The α is known to be related to the recombination dynamics and balance of charge transport.[225-227] The OPV$_{X\_f-CNT}$ cells show large deviation of α from unity $\alpha = 1$, which shows unbalanced charge extraction behaviour at the electrodes, which is at least partially caused by the effect of a large sheet resistance in the top electrode.
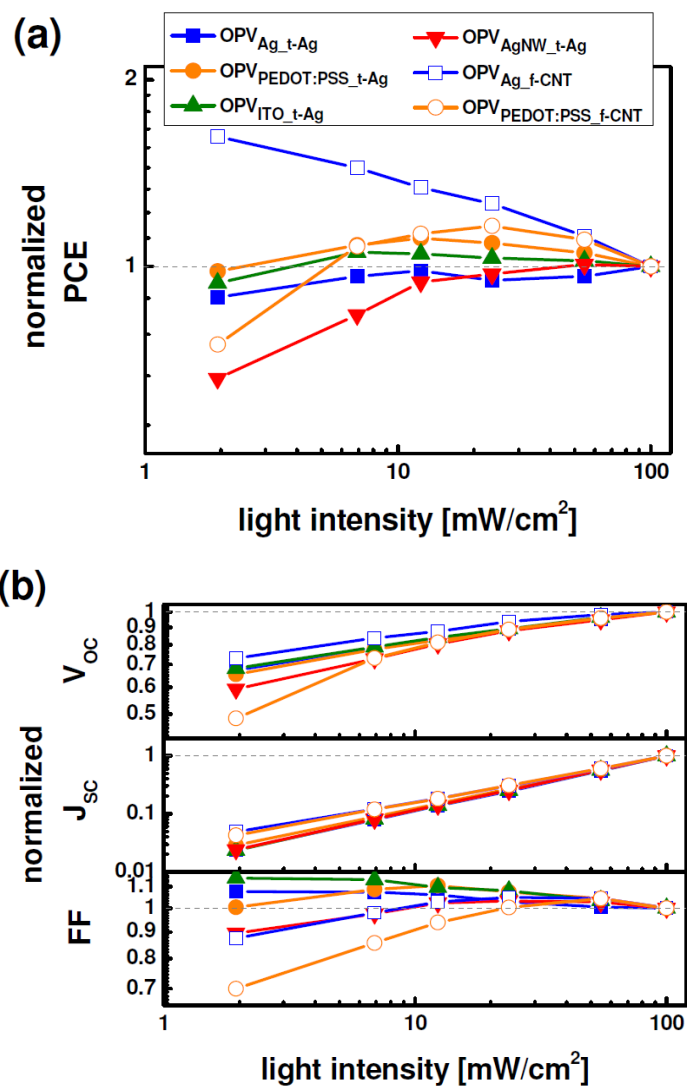
Figure 7.11. *Light intensity dependence of the device performance of the OPV cells. Graphs are plotted on log scale. Measured data is normalized at 100 mW/cm² due to disparity of PCE values from different OPV fabrication run in this measurement.*

Figure 7.12 shows the transmittances of the whole OPV cell. The averaged transmittances of the devices in the visible region (400 ~ 800 nm) are in the range of 20 ~ 30 %. The peak transmittances of OPV$_{PEDOT:PSS\_t-Ag}$ and OPV$_{ITO\_t-Ag}$ cells reach up to 40 %. Further optimization of device transmittance is possible by introducing an organic capping layer onto the top contact.[131]
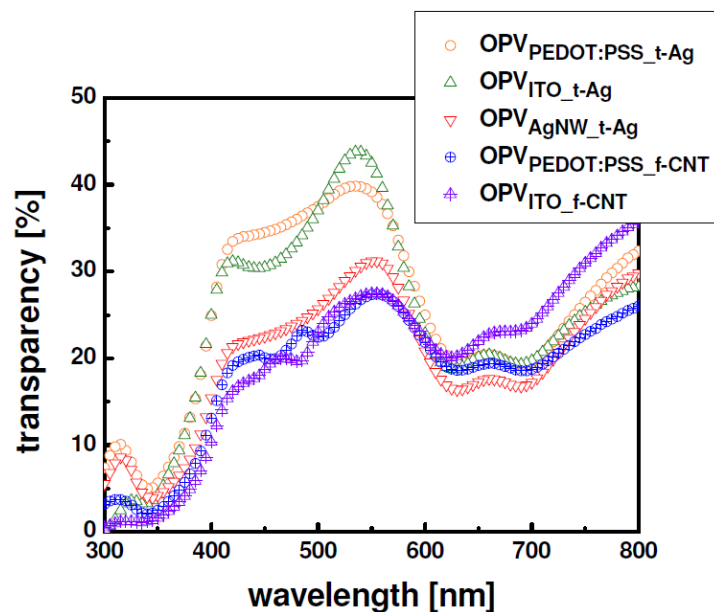
Figure 7.12. *The transmittances of semi-transparent OPV cells.*

Device	type	V_{OC} [V]	J_{SC} [mA/cm^2]	FF [%]	PCE [%]	transmittance [%] (400-800nm)	α	J(-1 V)/J_{SC}
OPV$_{Ag\_t-Ag}$	ITO-free	0.51	7.5	52.4	2.0	-	0.94	1.17
OPV$_{PEDOT:PSS\_t-Ag}$	ITO-free Semi-trans.	0.52	8.5	42.0	1.9	29	0.90	1.28
OPV$_{ITO\_t-Ag}$	Semi-trans.	0.52	8.6	48.9	2.2	28	0.95	1.20
OPV$_{AgNW\_t-Ag}$	ITO-free Semi-trans.	0.49	8.5	50.6	2.1	23*	0.94	1.22
OPV$_{Ag\_f-CNT}$	ITO-free	0.48	6.8	41.6	1.5	-	0.76	1.42
OPV$_{PEDOT:PSS\_f-CNT}$	ITO-free Semi-trans.	0.48	6.1	38.6	1.1	22	0.80	1.55
OPV$_{ITO\_f-CNT}$	Semi-trans.	0.50	6.3	40.2	1.3	24	-	1.41

Table 7.3. *Characteristics of OPV cells measured under an AM 1.5G illumination and normalized to 100 mW/cm^2. *The value of transmittance of OPV$_{AgNW\_t-Ag}$ cell does not contain the diffuse transmission.*

In summary, we have demonstrated the combination of bottom and top electrodes for semi-transparent or ITO-free small molecule OPV cells. Promising efficiencies up to 2.2 % are shown for the devices with t-Ag top electrodes. The AgNW and t-Ag combination shows a particularly promising PCE with semi-transparent and ITO-free properties. The devices with top f-CNT electrodes show an efficiency of 1.5 %. In addition, a different behaviour of light

130

intensity dependence of the devices is observed according to the various electrode combinations. We believe that this study provides a comprehensive overview on the performance and combination possibilities of different electrode types and allows to optimize semi-transparent and low-cost ITO-free flexible OPV cells.

Chapter 8. Conclusion and outlook

8.1. Conclusion

In this thesis, novel approaches to develop low-cost, efficient, long-term stable, semi-transparent, and flexible organic photovoltaic (OPV) cells and organic light-emitting diodes (OLEDs) based on alternative electrodes are demonstrated. Conductive polymer, transparent conductive oxide, and carbon nanotube are investigated as electrode materials for organic devices. For high efficiency and long lifetime of devices, electrodes, interfacial layers, and device stack are carefully optimized.

First, highly conductive poly(3,4-ethylenedioxythiophene):poly(styrenesulfonate) (PEDOT:PSS) films as standalone electrodes for organic solar cells have been optimized using a solvent post-treatment method. The treated PEDOT:PSS films show enhanced conductivities up to 1418 S/cm accompanied by structural and chemical changes. The effect of the solvent treatment on PEDOT:PSS has been investigated in detail and is shown to cause a reduction of insulating PSS in the conductive polymer layer. Using these optimized electrodes, indium tin oxide (ITO)-free small molecule OPV cells with zinc phthalocyanine (ZnPc) : fullerene C_{60} bulk heterojunction have been produced on glass and PET substrates. The system is further improved by pre-heating the PEDOT:PSS electrodes, which enhances the power conversion efficiency to the values obtained for solar cells on ITO electrodes. In addition, the solar cells with post-treated PEDOT:PSS electrodes show significantly improved short circuit current densities and efficiencies compared to untreated devices. Moreover, the removal of PSS by the post-treatment significantly improves the lifetime of devices, which are more resistant to loss of fill factor compared to untreated devices. The results present that optimized PEDOT:PSS with solvent and thermal post-treatment is a very promising electrode material for highly efficient flexible ITO-free organic solar cells.

Furthermore, we have reported efficient transparent OLEDs with improved stability based on PEDOT:PSS electrodes. Based on optical simulations, the device structures are carefully optimized by tuning the thickness of doped transport layers and electrodes. As a result, the

performance of PEDOT:PSS-based OLEDs reaches that of ITO-based reference devices. In addition, not only the efficiency but also the long-term stability of PEDOT:PSS-based OLEDs is significantly improved. The structure engineering demonstrated in this study greatly enhances the overall performances of ITO-free transparent OLEDs in terms of efficiency, lifetime, and transmittance. These results indicate that PEDOT:PSS-based OLEDs have a promising future for practical applications in low-cost and flexible device manufacturing.

In addition, a high performance internal light out-coupling system for efficient white OLEDs with spontaneously formed metal oxide nanostructures has been developed. The fabrication process of the out-coupling system is simple and can be scaled to large area manufacturing. The enhancement of the external quantum efficiency (EQE) in white OLEDs with the out-coupling system reaches a factor of 1.7. Moreover, hightly enhanced EQE by a factor of 2.9 is observed for a device integrated with an additional hemisphere lens structure, being able to extract all light from the substrate. Together with the improvement of light extraction, excellent color stability over broad viewing angles is achieved.

Next, we have demonstrated high performance ITO-free small molecule OPV cells and OLEDs, using optimized ZnO electrodes with alternative non-metallic co-dopants. The co-doping of hydrogen and fluorine reduces the metal content of ZnO thin films, resulting in a low absorption coefficient, a high transmittance, and a low refractive index as well as the high conductivity which are needed for the application in OPV cells and OLEDs. While the established metal doped ZnO films do have good electrical and optical properties with a long history over the past few decades, their application in organic devices is not as efficient as other alternative electrode approaches, due to their low work function and poor chemical stability. The optimized ZnO electrodes presented here are employed in OPV cells as well as OLEDs and allow not only the replacement of ITO, but also significantly improve the efficiency compared to our lab-standard ITO. The enhanced performance is attributed to the outstanding optical properties and spontaneously nanostructured surfaces of the ZnO films with non-metallic co-dopants and their straightforward integration with our molecular doping technology, which avoids several common drawbacks of ZnO electrodes such as high energy barriers at the interfaces or chemical instabilities. Our observations show that optimized ZnO films with non-metallic co-dopants are a promising and competitive electrode for low-cost and high performance OPV cells and OLEDs.

Finally, we have developed semi-transparent n-i-p OPV cells with free-standing multi-wall carbon nanotube (f-CNT) sheets as transparent top electrodes. By a simple and damage-free room temperature orthogonal liquid solution assisted self-laminating process, f-CNT top electrodes are successfully deposited on top of $ZnPc : C_{60}$ bulk heterojunction small molecule OPV cells. The cells show high fill factors above 58 % as well as efficiencies up to 1.5 % and greater long-term stability compared to the device having a metal electrode. For the given cell structure with f-CNT semi-transparent electrodes, the influence of an optical spacer on light absorption is studied by a systematic variation of the hole transport layer thickness, supported by optical simulations. The results strongly indicate that OPV cells with f-CNT top electrodes and optimized thin film stack are highly promising for semi-transparent OPV cells, which can be used in tandem devices, in tinted smart windows and similar applications by a simple and damage-free process in roll-to-roll configuration, that can be scaled to large area manufacturing.

Furthermore, we have investigated various electrode combinations of bottom and top contacts for OPV cells. Silver (Ag), ITO, PEDOT:PSS, and silver nanowires (AgNW) are used as bottom electrodes. As top electrodes, thin silver layers (t-Ag) and f-CNT sheets are employed. The manufactured $ZnPc : C_{60}$ small molecule bulk heterojunction OPV cells with different kinds of bottom electrodes show efficiencies of 1.9 ~ 2.2 % and 1.1 ~ 1.5 %, when comprised of t-Ag and f-CNT top contacts, respectively. We demonstrate alternative electrodes beyond ITO, silver, and aluminum, which can be readily used for organic photovoltaics technology.

To conclude, small molecule OPV cells and OLEDs based on alternative electrodes such as PEDOT:PSS, CNT, and doped ZnO have been studied in this thesis. The research has focused on not only the improvement of efficiency in devices but also the stability/lifetime of devices by various optimization processes for electrodes, interfaces, and stack of devices. We have achieved a record conductivity of PEDOT:PSS as well as very high device efficiencies based on PEDOT:PSS and ZnO alternative electrodes, comparable to ITO reference devices. We believe that the methods studied here will be a good guidance for developing efficient, stable, semi-transparent, low-cost, and flexible organic optoelectronic devices based on alternative electrodes.

8.2. Outlook

Up to now, most studies of alternative electrodes have focused on achieving high device efficiency. One should pay great attention not only to the efficiency of organic devices but also to their stability and try to find a way to improve both of them. Furthermore, for any alternative electrode for OPV cells and OLEDs, the device structure has to be carefully optimized in terms of thin-film optical effects in order to achieve optimum in/out-coupling, i.e., constructive interference. It should be also highlighted that not only the high transmittance and low sheet resistance of electrodes, but also electrode surface roughness, chemical stability, energy level alignment with adjacent organic layers, and optimum geometry of organic devices should be further studied for efficient and long-living OPV cells and OLEDs based on alternative electrodes.

PEDOT:PSS has a great potential for practical applications in low-cost, flexible devices. However, the high sheet resistance and large amount of hygroscopic PSS limit its potential. To further improve the conductivity of PEDOT:PSS especially for large area devices, metal grid can be used. In the application of PEDOT:PSS reinforced by metal grid, balancing the transmittance and the conductivity of hybrid system is of importance for achieving high performance of organic devices. Thin semi-transparent metal grids will allow the high transmittance of PEDOT:PSS electrodes while maintaining the high conductivity. In addition to the use of metal grids, the novel solvent or post-treatment process for PEDOT:PSS films provides the opportunity to further enhance the conductivity. It is also worth trying to introduce an ultra thin metal layer onto the surface of PEDOT:PSS films, with a subsequent heat treatment. This may selectively cover insulating PSS, thus forming a conductive bridge between PEDOT grains, which are surrounded by thin PSS shell, which might further enhance charge carrier transport. The issue of chemical instability in PEDOT:PSS can be solved by reducing the amount of hygroscopic PSS as well as water. The use of insitu polymerized PEDOT or a solvent post-treatment on PEDOT:PSS presented in chapter 5 are good ways to remove PSS and residual water in PEDOT:PSS films for practical use.

The most promising transparent electrodes from a performance view point are ZnO-based electrodes due to its high conductivity and high transmittance with the longest history among alternatives. For the further improvement of the conductivity of ZnO, achieving a high mobility is desirable rather than the high carrier concentration which leads to optical losses due to free carrier absorption. Therefore, approaches for high mobilities while retaining a

moderate carrier concentration need to be studied. A possible method for the purpose is to increase a grain size of ZnO films, which is typically in the size of 20-30 nm, for efficient charge carrier transport by reducing grain boundaries. Introducing a template layer having large grains under ZnO might influence the growth mode of ZnO and give the probability to control the grain size. Furthermore, a thermal treatment during the growth of ZnO to provide sufficient diffusion energy to form large grains is worth studying. The inherent brittleness of metal oxide films strongly limits practical use in flexible devices. The approaches using oxide-metal-oxide multilayer structure have been widely investigated to improve the flexibility of ZnO thin films. The surface treatment on the flexible substrate might improve adhesion and mechanical properties so the flexibility of ZnO films is expected to be improved.

Despite of the excellent mechanical flexibility of CNT, the higher sheet resistance of CNT electrodes compared to other electrodes limits the high performance organic devices due to the high tube-tube contact resistance and the high surface roughness. The molecular doping into the CNT surface is believed to reduce the junction resistance, thus enhancing the conductivity of CNT films. The use of thick molecular doped transport layers could flatten the CNT surface to prevent electrical shorts and leakage currents without any electrical and optical losses.

Further studies to improve conductivity, chemical stability, and flexibility of alternative electrodes are needed for fully replacing the conventional ITO electrode. It is believed that extensive studies on alternative electrodes will finally realize the practical highly efficient, low-cost, flexible organic optoelectronic devices in the near future.

Bibliography

[1]   B. Bolto, R. McNeill, D. Weiss, *Aust. J. Chem.* **1963**, *16*, 1090.
[2]   R. McNeill, R. Siudak, J. Wardlaw, D. Weiss, *Aust. J. Chem.* **1963**, *16*, 1056.
[3]   F. Carey, *Organic Chemistry On-Line Learning Center.*
[4]   W. Brütting, *Physics of organic semiconductors*, Wiley-VCH, **2005**.
[5]   M. Pfeiffer, S. R. Forrest, *Organic light emitting devices*, Wiley-VCH, Weinheim, 2nd edition, **2005**.
[6]   J. Blochwitz, T. Fritz, M. Pfeiffer, K. Leo, D. Alloway, P. Lee, N. Armstrong, *Organic Electronics* **2001**, *2*, 97.
[7]   M. Pope, C. E. Swenberg, *Electronic processes in organic crystals and polymers*, Oxford University Press, **1999**.
[8]   M. Schwoerer, H. C. Wolf, *Organische Molekulare Festkörper*, Wiley-VCH Weinheim, **2005**.
[9]   P. W. Atkins, R. S. Friedman, *Molecular quantum mechanics*, Vol. 3, Oxford University Press Oxford, **1997**.
[10]   T. Drori, *Optical study of pi-conjugated polymers and pi-conjugated polymers/fullerene blends*, ProQuest, **2009**.
[11]   R. Farchioni, *Organic electronic materials: conjugated polymers and low molecular weight organic solids*, Vol. 41, Springer Verlag, **2001**.
[12]   M. Pope, C. Swenberg, *Electronic processes in organic molecular crystals*, Oxford University Press, New York, **1982**.
[13]   S. Pawlizak, *University of Leipzig, diploma thesis* **2009**.
[14]   C. Adachi, M. A. Baldo, M. E. Thompson, S. R. Forrest, *J. Appl. Phys.* **2001**, *90*, 5048.
[15]   Y. Kawamura, K. Goushi, J. Brooks, J. J. Brown, H. Sasabe, C. Adachi, *Appl. Phys. Lett.* **2005**, *86*, 071104.
[16]   Z. Li, H. Meng, *Organic light-emitting materials and devices*, CRC Press, **2006**.
[17]   http://chemwiki.ucdavis.edu/, *Förster and Dexter energy transfer.*
[18]   J. Guillet, *Polymer photophysics and photochemistry: an introduction to the study of photoprocesses in macromolecules*, Cambridge University Press, New York, NY, **1987**.
[19]   N. Karl, *Synth. Met.* **2003**, *133*, 649.
[20]   B. Maennig, M. Pfeiffer, A. Nollau, X. Zhou, K. Leo, P. Simon, *Physical Review B* **2001**, *64*, 195208.
[21]   H. Bässler, *physica status solidi (b)* **1993**, *175*, 15.
[22]   P. Peumans, A. Yakimov, S. R. Forrest, *J. Appl. Phys.* **2003**, *93*, 3693.
[23]   http://nanohub.org/topics/CarrierStatisticsPage, *Carrier-statistics in semiconductors.*
[24]   M. A. Green, *Solar cells: operating principles, technology, and system applications*, **1982**.
[25]   W. Shockley, W. Read Jr, *Physical Review* **1952**, *87*, 835.
[26]   W. Shockley, *Bell Syst. Tech. J* **1949**, *28*, 435.
[27]   B. A. Gregg, S. G. Chen, R. A. Cormier, *Chem. Mater.* **2004**, *16*, 4586.
[28]   J. L. Brédas, J. Cornil, A. J. Heeger, *Adv. Mater.* **2004**, *8*, 447.
[29]   C. Tang, *Appl. Phys. Lett.* **1986**, *48*, 183.
[30]   G. Yu, J. Gao, J. Hummelen, F. Wudl, A. Heeger, *Science* **1995**, *270*, 1789.
[31]   G. Chamberlain, *Solar Cells* **1983**, *8*, 47.
[32]   D. Wöhrle, D. Meissner, *Adv. Mater.* **2004**, *3*, 129.

[33]   D. Morel, A. Ghosh, T. Feng, E. Stogryn, P. Purwin, R. Shaw, C. Fishman, *Appl. Phys. Lett.* **1978**, *32*, 495.

[34]   A. K. Ghosh, T. Feng, *J. Appl. Phys.* **1978**, *49*, 5982.

[35]   J. D. Servaites, M. A. Ratner, T. J. Marks, *Energy & Environmental Science* **2011**, *4*, 4410.

[36]   C. Deibel, V. Dyakonov, *Reports on Progress in Physics* **2010**, *73*, 096401.

[37]   C. Tang, S. VanSlyke, *Appl. Phys. Lett.* **1987**, *51*, 913.

[38]   K. Walzer, B. Maennig, M. Pfeiffer, K. Leo, *Chemical Reviews* **2007**, *107*, 1233.

[39]   R. Meerheim, B. Lussem, K. Leo, *Proceedings of the IEEE* **2009**, *97*, 1606.

[40]   M. Baldo, D. O'brien, Y. You, A. Shoustikov, S. Sibley, M. Thompson, S. Forrest, *Nature* **1998**, *395*, 151.

[41]   D. Bradley, *Synth. Met.* **1993**, *54*, 401.

[42]   M. Baldo, D. O'brien, M. Thompson, S. Forrest, *Physical Review B* **1999**, *60*, 14422.

[43]   M. Segal, M. Baldo, R. Holmes, S. Forrest, Z. Soos, *Physical Review B* **2003**, *68*, 075211.

[44]   N. C. Greenham, R. H. Friend, D. D. C. Bradley, *Adv. Mater.* **2004**, *6*, 491.

[45]   B. E. A. Saleh, M. C. Teich, B. E. Saleh, *Fundamentals of photonics*, Vol. 22, Wiley New York, **1991**.

[46]   M. H. Lu, J. Sturm, *J. Appl. Phys.* **2002**, *91*, 595.

[47]   S. Möller, S. Forrest, *J. Appl. Phys.* **2002**, *91*, 3324.

[48]   M. Thomschke, S. Reineke, B. Lüssem, K. Leo, *Nano Lett.* **2012**, *12*, 424.

[49]   K. Hong, H. K. Yu, I. Lee, K. Kim, S. Kim, J. L. Lee, *Adv. Mater.* **2010**, *22*, 4890.

[50]   T. Nakamura, H. Fujii, N. Juni, N. Tsutsumi, *Optical review* **2006**, *13*, 104.

[51]   T. Yamasaki, K. Sumioka, T. Tsutsui, *Appl. Phys. Lett.* **2000**, *76*, 1243.

[52]   Y. Sun, S. R. Forrest, *Nat. Photonics* **2008**, *2*, 483.

[53]   S. Mladenovski, K. Neyts, D. Pavicic, A. Werner, C. Rothe, *Optics Express* **2009**, *17*, 7562.

[54]   S. Reineke, F. Lindner, G. Schwartz, N. Seidler, K. Walzer, B. Lüssem, K. Leo, *Nature* **2009**, *459*, 234.

[55]   B. Maennig, J. Drechsel, D. Gebeyehu, P. Simon, F. Kozlowski, A. Werner, F. Li, S. Grundmann, S. Sonntag, M. Koch, *Appl. Phys. A: Mater. Sci. Process.* **2004**, *79*, 1.

[56]   M. Pfeiffer, T. Fritz, J. Blochwitz, A. Nollau, B. Plönnigs, A. Beyer, K. Leo, *Advances in Solid State Physics 39* **1999**, 77.

[57]   M. Pfeiffer, A. Beyer, T. Fritz, K. Leo, *Appl. Phys. Lett.* **1998**, *73*, 3202.

[58]   G. He, M. Pfeiffer, K. Leo, M. Hofmann, J. Birnstock, R. Pudzich, J. Salbeck, *Appl. Phys. Lett.* **2004**, *85*, 3911.

[59]   K. Fehse, R. Meerheim, K. Walzer, K. Leo, W. Lövenich, A. Elschner, *Appl. Phys. Lett.* **2008**, *93*, 083303.

[60]   T. Minami, *Semicond. Sci. Technol.* **2005**, *20*, S35.

[61]   G. J. Exarhos, X. D. Zhou, *Thin Solid Films* **2007**, *515*, 7025.

[62]   T. Minami, *Thin Solid Films* **2008**, *516*, 5822.

[63]   T. Minami, *Mrs Bulletin* **2000**, *25*, 38.

[64]   S. Pearton, D. Norton, K. Ip, Y. Heo, T. Steiner, *Progress in Materials Science* **2005**, *50*, 293.

[65]   K. Ellmer, *J. Phys. D: Appl. Phys.* **2001**, *34*, 3097.

[66]   K. Ellmer, R. Mientus, *Thin Solid Films* **2008**, *516*, 4620.

[67]   K. Ellmer, G. Vollweiler, *Thin Solid Films* **2006**, *496*, 104.

[68]   M. Jørgensen, K. Norrman, F. C. Krebs, *Sol. Energy Mater. Sol. Cells* **2008**, *92*, 686.

[69]   J. H. Park, S. J. Kang, S. I. Na, H. H. Lee, S. W. Kim, H. Hosono, H. K. Kim, *Sol. Energy Mater. Sol. Cells* **2011**, *95*, 2178.

[70]   J. Bernède, L. Cattin, M. Morsli, Y. Berredjem, *Sol. Energy Mater. Sol. Cells* **2008**, *92*, 1508.

[71]   V. Bhosle, J. Prater, F. Yang, D. Burk, S. Forrest, J. Narayan, *J. Appl. Phys.* **2007**, *102*, 023501.

[72]   P. K. Nayak, J. Kim, S. Chung, J. Jeong, C. Lee, Y. Hong, *J. Phys. D: Appl. Phys.* **2009**, *42*, 139801.

[73]   H. Kim, C. Gilmore, J. Horwitz, A. Pique, H. Murata, G. Kushto, R. Schlaf, Z. Kafafi, D. Chrisey, *Appl. Phys. Lett.* **2000**, *76*, 259.

[74]   Y. Tomita, C. May, M. Toerker, J. Amelung, M. Eritt, F. Loeffler, C. Luber, K. Leo, K. Walzer, K. Fehse, *Appl. Phys. Lett.* **2007**, *91*, 063510.

[75]   J. Owen, M. Son, K. H. Yoo, B. Ahn, S. Lee, *Appl. Phys. Lett.* **2007**, *90*, 033512.

[76]   C. Chiang, C. Fincher Jr, Y. Park, A. Heeger, H. Shirakawa, E. Louis, S. Gau, A. G. MacDiarmid, *Phys. Rev. Lett.* **1977**, *39*, 1098.

[77]   H. Shirakawa, E. J. Louis, A. G. MacDiarmid, C. K. Chiang, A. J. Heeger, *J. Chem. Soc., Chem. Commun.* **1977**, 578.

[78]   T. A. Skotheim, *Handbook of conducting polymers*, Marcel Dekker, **1998**.

[79]   D. Trivedi, H. Nalwa, *Handbook of organic conductive molecules and polymers* **1997**, *2*.

[80]   F. Jonas, L. Schrader, *Synth. Met.* **1991**, *41*, 831.

[81]   F. Jonas, G. Heywang, W. Schmidtberg, J. Heinze, M. Dietrich, **1988**, Eur. Patent 339 340.

[82]   L. Groenendaal, F. Jonas, D. Freitag, H. Pielartzik, J. R. Reynolds, *Adv. Mater.* **2000**, *12*, 481.

[83]   S. Kirchmeyer, K. Reuter, *J. Mater. Chem.* **2005**, *15*, 2077.

[84]   A. M. Nardes, M. Kemerink, R. A. J. Janssen, J. A. M. Bastiaansen, N. M. M. Kiggen, B. M. W. Langeveld, A. J. J. M. van Breemen, M. M. de Kok, *Adv. Mater.* **2007**, *19*, 1196.

[85]   J. Ouyang, C. W. Chu, F. C. Chen, Q. Xu, Y. Yang, *Adv. Funct. Mater.* **2005**, *15*, 203.

[86]   X. Crispin, F. Jakobsson, A. Crispin, P. Grim, P. Andersson, A. Volodin, C. Van Haesendonck, M. Van der Auweraer, W. Salaneck, M. Berggren, *Chem. Mater* **2006**, *18*, 4354.

[87]   J. Huang, P. F. Miller, J. S. Wilson, A. J. de Mello, J. C. de Mello, D. D. C. Bradley, *Adv. Funct. Mater.* **2005**, *15*, 290.

[88]   P. A. Levermore, L. Chen, X. Wang, R. Das, D. D. C. Bradley, *Adv. Mater.* **2007**, *19*, 2379.

[89]   Y. H. Ha, N. Nikolov, S. K. Pollack, J. Mastrangelo, B. D. Martin, R. Shashidhar, *Adv. Funct. Mater.* **2004**, *14*, 615.

[90]   S. I. Na, S. S. Kim, J. Jo, D. Y. Kim, *Adv. Mater.* **2008**, *20*, 4061.

[91]   H. Do, M. Reinhard, H. Vogeler, A. Puetz, M. F. G. Klein, W. Schabel, A. Colsmann, U. Lemmer, *Thin Solid Films* **2009**, *517*, 5900.

[92]   Y. H. Kim, C. Sachse, M. L. Machala, C. May, L. Müller‐Meskamp, K. Leo, *Adv. Funct. Mater.* **2011**, *21*, 1076.

[93]   Y. Xia, K. Sun, J. Ouyang, *Adv. Mater.* **2012**, *24*, 2436.

[94]   J. Kim, J. Jung, D. Lee, J. Joo, *Synth. Met.* **2002**, *126*, 311.

[95]   J. Ouyang, Q. Xu, C. W. Chu, Y. Yang, G. Li, J. Shinar, *Polymer* **2004**, *45*, 8443.

[96]   F. Zhang, M. Johansson, M. R. Andersson, J. C. Hummelen, O. Inganäs, *Adv. Mater.* **2002**, *14*, 662.

[97]   K. Fehse, K. Walzer, K. Leo, W. Lövenich, A. Elschner, *Adv. Mater.* **2007**, *19*, 441.

[98]   D. J. Lipomi, B. C. K. Tee, M. Vosgueritchian, Z. Bao, *Adv. Mater.* **2011**, *23*, 1771.

[99]   Y. H. Kim, C. Sachse, M. Hermenau, K. Fehse, M. Riede, L. Muller-Meskamp, K. Leo, *Appl. Phys. Lett.* **2011**, *99*, 113305.

[100]   T. Dürkop, S. Getty, E. Cobas, M. Fuhrer, *Nano Lett.* **2004**, *4*, 35.

[101] J. Y. Park, S. Rosenblatt, Y. Yaish, V. Sazonova, H. Üstünel, S. Braig, T. Arias, P. W. Brouwer, P. L. McEuen, *Nano Lett.* **2004**, *4*, 517.

[102] S. Li, Z. Yu, C. Rutherglen, P. J. Burke, *Nano Lett.* **2004**, *4*, 2003.

[103] S. Iijima, *Nature* **1991**, *354*, 56.

[104] S. Iijima, T. Ichihashi, *Nature* **1993**, *363*, 603.

[105] D. Bethune, C. Klang, M. De Vries, G. Gorman, R. Savoy, J. Vazquez, R. Beyers, *Nature* **1993**, *363*, 605.

[106] Y. Zhang, Y. Bai, B. Yan, Drug Discovery Today **2010**, *15*, 428.

[107] J. Li, L. Hu, L. Wang, Y. Zhou, G. Grüner, T. J. Marks, *Nano Lett.* **2006**, *6*, 2472.

[108] Z. Wu, Z. Chen, X. Du, J. M. Logan, J. Sippel, M. Nikolou, K. Kamaras, J. R. Reynolds, D. B. Tanner, A. F. Hebard, *Science* **2004**, *305*, 1273.

[109] M. Zhang, S. Fang, A. A. Zakhidov, S. B. Lee, A. E. Aliev, C. D. Williams, K. R. Atkinson, R. H. Baughman, *Science* **2005**, *309*, 1215.

[110] T. M. Barnes, J. D. Bergeson, R. C. Tenent, B. A. Larsen, G. Teeter, K. M. Jones, J. L. Blackburn, J. van de Lagemaat, *Appl. Phys. Lett.* **2010**, *96*, 243309.

[111] A. Du Pasquier, H. E. Unalan, A. Kanwal, S. Miller, M. Chhowalla, *Appl. Phys. Lett.* **2005**, *87*, 203511.

[112] L. Hu, J. Li, J. Liu, G. Grüner, T. Marks, *Nanotechnology* **2010**, *21*, 155202.

[113] M. W. Rowell, M. A. Topinka, M. D. McGehee, H. J. Prall, G. Dennler, N. S. Sariciftci, L. Hu, G. Gruner, *Appl. Phys. Lett.* **2006**, *88*, 233506.

[114] J. van de Lagemaat, T. M. Barnes, G. Rumbles, S. E. Shaheen, T. J. Coutts, C. Weeks, I. Levitsky, J. Peltola, P. Glatkowski, *Appl. Phys. Lett.* **2006**, *88*, 233503.

[115] D. Zhang, K. Ryu, X. Liu, E. Polikarpov, J. Ly, M. E. Tompson, C. Zhou, *Nano Lett.* **2006**, *6*, 1880.

[116] R. Ulbricht, S. B. Lee, X. Jiang, K. Inoue, M. Zhang, S. Fang, R. H. Baughman, A. A. Zakhidov, *Sol. Energy Mater. Sol. Cells* **2007**, *91*, 416.

[117] C. D. Williams, R. O. Robles, M. Zhang, S. Li, R. H. Baughman, A. A. Zakhidov, *Appl. Phys. Lett.* **2008**, *93*, 183506.

[118] S. Tanaka, K. Mielczarek, R. Ovalle-Robles, B. Wang, D. Hsu, A. Zakhidov, *Appl. Phys. Lett.* **2009**, *94*, 113506.

[119] T. Ameri, G. Dennler, C. Lungenschmied, C. J. Brabec, *Energy & Environmental Science* **2009**, *2*, 347.

[120] A. Hadipour, B. de Boer, P. W. M. Blom, *J. Appl. Phys.* **2007**, *102*, 074506.

[121] D. S. Hecht, A. M. Heintz, R. Lee, L. Hu, B. Moore, C. Cucksey, S. Risser, *Nanotechnology* **2011**, *22*, 075201.

[122] J. Y. Lee, S. T. Connor, Y. Cui, P. Peumans, *Nano Lett.* **2008**, *8*, 689.

[123] J. Y. Lee, S. T. Connor, Y. Cui, P. Peumans, *Nano Lett.* **2010**, *10*, 1276.

[124] X. Y. Zeng, Q. K. Zhang, R. M. Yu, C. Z. Lu, *Adv. Mater.* **2010**, *22*, 4484.

[125] L. Li, Z. Yu, W. Hu, C. Chang, Q. Chen, Q. Pei, *Adv. Mater.* **2011**, *23*, 5563.

[126] W. Gaynor, G. F. Burkhard, M. D. McGehee, P. Peumans, *Adv. Mater.* **2011**, *23*, 2905.

[127] T. Dobbertin, M. Kroeger, D. Heithecker, D. Schneider, D. Metzdorf, H. Neuner, E. Becker, H. H. Johannes, W. Kowalsky, *Appl. Phys. Lett.* **2003**, *82*, 284.

[128] H. Schmidt, H. Flugge, T. Winkler, T. Bulow, T. Riedl, W. Kowalsky, *Appl. Phys. Lett.* **2009**, *94*, 243302.

[129] D. Han, H. Kim, S. Lee, M. Seo, S. Yoo, *Optics Express* **2010**, *18*, A513.

[130] J. Meiss, M. Furno, S. Pfuetzner, K. Leo, M. Riede, *J. Appl. Phys.* **2010**, *107*, 053117.

[131] J. Meiss, K. Leo, M. Riede, C. Uhrich, W. M. Gnehr, S. Sonntag, M. Pfeiffer, *Appl. Phys. Lett.* **2009**, *95*, 213306.

[132] J. Meiss, T. Menke, K. Leo, C. Uhrich, W. M. Gnehr, S. Sonntag, M. Pfeiffer, M. Riede, *Appl. Phys. Lett.* **2011**, *99*, 043301.

[133] J. Meiss, M. Riede, K. Leo, *Appl. Phys. Lett.* **2009**, *94*, 013303.

[134] J. Meiss, M. Riede, K. Leo, *J. Appl. Phys.* **2009**, *105*, 063108.

[135] J. Meiss, N. Allinger, M. Riede, K. Leo, *Appl. Phys. Lett.* **2008**, *93*, 103311.

[136] H. W. Lin, S. W. Chiu, L. Y. Lin, Z. Y. Hung, Y. H. Chen, F. Lin, K. T. Wong, *Adv. Mater.* **2012**, *24*, 2269.

[137] Z. Wang, M. Helander, J. Qiu, D. Puzzo, M. Greiner, Z. Hudson, S. Wang, Z. Liu, Z. Lu, *Nat. Photonics* **2011**, *5*, 753.

[138] S. Schubert, M. Hermenau, J. Meiss, L. Müller-Meskamp, K. Leo, *Adv. Funct. Mater.* **2012**, *22*, 4993.

[139] N. P. Sergeant, A. Hadipour, B. Niesen, D. Cheyns, P. Heremans, P. Peumans, B. P. Rand, *Adv. Mater.* **2012**, *24*, 728.

[140] X. Wan, G. Long, L. Huang, Y. Chen, *Adv. Mater.* **2011**, *23*, 5342.

[141] S. Pang, Y. Hernandez, X. Feng, K. Müllen, *Adv. Mater.* **2011**, *23*, 2779.

[142] X. Huang, Z. Zeng, Z. Fan, J. Liu, H. Zhang, *Adv. Mater.* **2012**, *24*, 5979.

[143] J. Wu, H. A. Becerril, Z. Bao, Z. Liu, Y. Chen, P. Peumans, *Appl. Phys. Lett.* **2008**, *92*, 263302.

[144] Z. Yin, S. Sun, T. Salim, S. Wu, X. Huang, Q. He, Y. M. Lam, H. Zhang, *ACS Nano* **2010**, *4*, 5263.

[145] L. Gomez De Arco, Y. Zhang, C. W. Schlenker, K. Ryu, M. E. Thompson, C. Zhou, *ACS Nano* **2010**, *4*, 2865.

[146] Y. Wang, S. W. Tong, X. F. Xu, B. Özyilmaz, K. P. Loh, *Adv. Mater.* **2011**, *23*, 1514.

[147] M. Choe, B. H. Lee, G. Jo, J. Park, W. Park, S. Lee, W. K. Hong, M. J. Seong, Y. H. Kahng, K. Lee, *Organic Electronics* **2010**, *11*, 1864.

[148] J. Wu, M. Agrawal, H. A. Becerril, Z. Bao, Z. Liu, Y. Chen, P. Peumans, *ACS Nano* **2009**, *4*, 43.

[149] A. K. Geim, K. S. Novoselov, *Nat. Mater.* **2007**, *6*, 183.

[150] H. Li, B. C. K. Tee, J. J. Cha, Y. Cui, J. W. Chung, S. Y. Lee, Z. Bao, *J. Am. Chem. Soc.* **2012**, *134*, 2760.

[151] T. Menke, D. Ray, J. Meiss, K. Leo, M. Riede, *Appl. Phys. Lett.* **2012**, *100*, 093304.

[152] W. Gao, A. Kahn, *Appl. Phys. Lett.* **2001**, *79*, 4040.

[153] J. Meiss, A. Merten, M. Hein, C. Schuenemann, S. Schäfer, M. Tietze, C. Uhrich, M. Pfeiffer, K. Leo, M. Riede, *Adv. Funct. Mater.* **2012**, *22*, 405.

[154] S. Olthof, W. Tress, R. Meerheim, B. Lussem, K. Leo, *J. Appl. Phys.* **2009**, *106*, 103711.

[155] J. Meiss, N. Allinger, C. Falkenberg, K. Leo, M. Riede, *Proc. SPIE* **2009**, *7416*, 741603.

[156] M. Furno, R. Meerheim, M. Thomschke, S. Hofmann, B. Lüssem, K. Leo, *Proc. of SPIE* **2010**, *7617*, 761716.

[157] X. Crispin, F. L. E. Jakobsson, A. Crispin, P. C. M. Grim, P. Andersson, A. Volodin, C. Van Haesendonck, M. Van der Auweraer, W. R. Salaneck, M. Berggren, *Chemical Materials* **2006**, *18*, 4354.

[158] Y. S. Hsiao, W. T. Whang, C. P. Chen, Y. C. Chen, *J. Mater. Chem.* **2008**, *18*, 5948.

[159] U. Lang, E. Müller, N. Naujoks, J. Dual, *Adv. Funct. Mater.* **2009**, *19*, 1215.

[160] J. Sun, W. W. Gerberich, L. F. Francis, *Prog. Org. Coat.* **2007**, *59*, 115.

[161] M. P. De Jong, L. J. Van Ijzendoorn, M. J. A. De Voigt, *Appl. Phys. Lett.* **2000**, *77*, 2255.

[162] A. M. Nardes, M. Kemerink, M. M. de Kok, E. Vinken, K. Maturova, R. A. J. Janssen, *Org. Electron.* **2008**, *9*, 727.

[163] J. Cho, K. Char, J. D. Hong, K. B. Lee, *Adv. Mater.* **2001**, *13*, 1076.

[164] R. R. Smith, A. P. Smith, J. T. Stricker, B. E. Taylor, M. F. Durstock, *Macromolecules* **2006**, *39*, 6071.

[165] P. Vacca, M. Petrosino, R. Miscioscia, G. Nenna, C. Minarini, D. Della Sala, A. Rubino, *Thin Solid Films* **2008**, *516*, 4232.

[166] D. Wakizaka, T. Fushimi, H. Ohkita, S. Ito, *Polymer* **2004**, *45*, 8561.

[167] D. M. DeLongchamp, B. D. Vogt, C. M. Brooks, K. Kano, J. Obrzut, C. A. Richter, O. A. Kirillov, E. K. Lin, *Langmuir* **2005**, *21*, 11480.

[168] V. Scardaci, R. Coull, J. N. Coleman, *Appl. Phys. Lett.* **2010**, *97*, 023114.

[169] S. Pfuetzner, J. Meiss, A. Petrich, M. Riede, K. Leo, *Appl. Phys. Lett.* **2009**, *94*, 3303.

[170] X. Xi, Q. Meng, F. Li, Y. Ding, J. Ji, Z. Shi, G. Li, *Sol. Energy Mater. Sol. Cells* **2010**, *94*, 623.

[171] K. Fehse, K. Walzer, K. Leo, W. Lövenich, A. Elschner, *Adv. Mater.* **2007**, *19*, 441.

[172] W. Tress, S. Pfützner, K. Leo, M. Riede, *Journal of Photonics for Energy* **2011**, *1*, 011114.

[173] V. Scardaci, R. Coull, J. N. Coleman, *Appl. Phys. Lett.* **2010**, *97*, 023114.

[174] K. Fehse, K. Walzer, K. Leo, W. Lövenich, A. Elschner, *Adv. Mater.* **2007**, *19*, 441.

[175] Y. H. Kim, C. Sachse, M. L. Machala, C. May, L. Müller-Meskamp, K. Leo, *Adv. Funct. Mater.* **2011**, *21*, 1076.

[176] R. Meerheim, M. Furno, S. Hofmann, B. Lüssem, K. Leo, *Appl. Phys. Lett.* **2010**, *97*, 253305.

[177] S. Hofmann, M. Thomschke, P. Freitag, M. Furno, B. Lüssem, K. Leo, *Appl. Phys. Lett.* **2010**, *97*, 253308.

[178] J. Lee, S. Hofmann, M. Furno, M. Thomschke, Y. H. Kim, B. LÜSSEM, K. Leo, *Organic electronics* **2011**, *12*, 1383.

[179] M. Cai, Z. Ye, T. Xiao, R. Liu, Y. Chen, R. W. Mayer, R. Biswas, K. M. Ho, R. Shinar, J. Shinar, *Adv. Mater.* **2012**, *24*, 4337.

[180] Y. H. Kim, C. Sachse, M. Hermenau, K. Fehse, M. Riede, L. Müller-Meskamp, K. Leo, *Appl. Phys. Lett.* **2011**, *99*, 113305.

[181] A. Nardes, M. Kemerink, M. De Kok, E. Vinken, K. Maturova, R. Janssen, *Organic electronics* **2008**, *9*, 727.

[182] T. C. Rosenow, M. Furno, S. Reineke, S. Olthof, B. Lussem, K. Leo, *J. Appl. Phys.* **2010**, *108*, 113113.

[183] W. H. Koo, S. M. Jeong, F. Araoka, K. Ishikawa, S. Nishimura, T. Toyooka, H. Takezoe, *Nat. Photonics* **2010**, *4*, 222.

[184] M. Fujita, T. Ueno, K. Ishihara, T. Asano, S. Noda, H. Ohata, T. Tsuji, H. Nakada, N. Shimoji, *Appl. Phys. Lett.* **2004**, *85*, 5769.

[185] R. G. Gordon, *MRS Bulletin* **2000**, *25*, 52.

[186] J. Hu, R. G. Gordon, *MRS Proceedings* **1990**, *202*, 457.

[187] I. Kim, K. S. Lee, T. S. Lee, J. Jeong, B. Cheong, Y. J. Baik, W. M. Kim, *J. Appl. Phys.* **2006**, *100*, 063701.

[188] C. G. Van de Walle, *Phys. Rev. Lett.* **2000**, *85*, 1012.

[189] C. G. Van de Walle, J. Neugebauer, *Nature* **2003**, *423*, 626.

[190] W. M. Kim, Y. H. Kim, J. S. Kim, J. Jeong, Y. J. Baik, J. K. Park, K. S. Lee, T.-Y. Seong, *J. Phys. D: Appl. Phys.* **2010**, *43*, 365406.

[191] Y. H. Kim, J. Jeong, K. S. Lee, J. K. Park, Y. J. Baik, T.-Y. Seong, W. M. Kim, *Appl. Surf. Sci.* **2010**, *256*, 5102.

[192] S. Lee, T. Lee, K. Lee, B. Cheong, Y. Kim, W. Kim, *Journal of Physics D: Applied Physics* **2008**, *41*, 095303.

[193] P. Erhart, K. Albe, *Appl. Phys. Lett.* **2006**, *88*, 201918.

[194] A. Janotti, C. G. Van de Walle, *Physical Review B* **2007**, *76*, 165202.

[195] L. Vlasenko, G. Watkins, *Physical Review B* **2005**, *71*, 125210.

[196] Y. H. Kim, C. Sachse, M. L. Machala, C. May, L. Müller-Meskamp, K. Leo, *Adv. Funct. Mater.* **2011**, *21*, 1076.

[197] S. Karan, B. Mallik, *The Journal of Physical Chemistry C* **2007**, *111*, 7352.

[198] P. Sullivan, T. S. Jones, A. Ferguson, S. Heutz, *Appl. Phys. Lett.* **2007**, *91*, 233114.

[199] Z. Tang, L. M. Andersson, Z. George, K. Vandewal, K. Tvingstedt, P. Heriksson, R. Kroon, M. R. Andersson, O. Inganäs, *Adv. Mater.* **2012**, *24*, 554.

[200] B. Yu, L. Huang, H. Wang, D. Yan, *Adv. Mater.* **2010**, *22*, 1017.

[201] P. Wellmann, M. Hofmann, O. Zeika, A. Werner, J. Birnstock, R. Meerheim, G. He, K. Walzer, M. Pfeiffer, K. Leo, *J. Soc. Inf. Disp* **2005**, *13*, 393.

[202] V. Shrotriya, G. Li, Y. Yao, T. Moriarty, K. Emery, Y. Yang, *Adv. Funct. Mater.* **2006**, *16*, 2016.

[203] H. W. Lin, S. W. Chiu, L. Y. Lin, Z. Y. Hung, Y. H. Chen, F. Lin, K. T. Wong, *Adv. Mater.* **2012**, *24*, 2269.

[204] S. G. Ihn, K. S. Shin, M. J. Jin, X. Bulliard, S. Yun, Y. Suk Choi, Y. Kim, J. H. Park, M. Sim, M. Kim, *Sol. Energy Mater. Sol. Cells* **2011**, *95*, 1610.

[205] J. Owen, M. Son, K. H. Yoo, B. Ahn, S. Lee, *Appl. Phys. Lett.* **2007**, *90*, 033512.

[206] S. W. Cho, Y. T. Kim, W. H. Shim, S. Y. Park, K. D. Kim, H. O. Seo, N. K. Dey, J. H. Lim, Y. Jeong, K. H. Lee, *Appl. Phys. Lett.* **2011**, *98*, 023102.

[207] Z. Hu, J. Zhang, Y. Zhao, *Appl. Phys. Lett.* **2012**, *100*, 103303.

[208] L. Müller-Meskamp, Y. H. Kim, T. Roch, S. Hofmann, R. Scholz, S. Eckardt, K. Leo, A. F. Lasagni, *Adv. Mater.* **2012**, *24*, 906.

[209] K. S. Nalwa, J. M. Park, K. M. Ho, S. Chaudhary, *Adv. Mater.* **2011**, *23*, 112.

[210] X. Zhu, W. C. H. Choy, F. Xie, C. Duan, C. Wang, W. He, F. Huang, Y. Cao, *Sol. Energy Mater. Sol. Cells* **2012**, *99*, 327.

[211] C. Gong, H. B. Yang, Q. L. Song, C. M. Li, *Org. Electron.* **2012**, *13*, 7.

[212] J. Hu, Z. Wu, H. Wei, T. Song, B. Sun, *Org. Electron.* **2012**, *13*, 1171.

[213] D. C. Lim, W. H. Shim, K. D. Kim, H. O. Seo, J. H. Lim, Y. Jeong, Y. D. Kim, K. H. Lee, *Sol. Energy Mater. Sol. Cells* **2011**, *95*, 3036.

[214] W. H. Shim, S. Y. Park, M. Y. Park, H. O. Seo, K. D. Kim, Y. T. Kim, Y. D. Kim, J. W. Kang, K. H. Lee, Y. Jeong, *Adv. Mater.* **2011**, *23*, 519.

[215] H. K. Yu, W. J. Dong, G. H. Jung, J. L. Lee, *ACS Nano* **2011**, *5*, 8026.

[216] L. Chen, P. Wang, F. Li, S. Yu, Y. Chen, *Sol. Energy Mater. Sol. Cells* **2012**, *102*, 66.

[217] V. Shrotriya, G. Li, Y. Yao, C. W. Chu, Y. Yang, *Appl. Phys. Lett.* **2006**, *88*, 073508.

[218] A. A. Zakhidov, J. K. Lee, H. H. Fong, J. A. DeFranco, M. Chatzichristidi, P. G. Taylor, C. K. Ober, G. G. Malliaras, *Adv. Mater.* **2008**, *20*, 3481.

[219] J. Meiss, K. Leo, M. K. Riede, C. Uhrich, W. M. Gnehr, S. Sonntag, M. Pfeiffer, *Appl. Phys. Lett.* **2009**, *95*, 213306.

[220] S. Pfuetzner, J. Meiss, A. Petrich, M. Riede, K. Leo, *Appl. Phys. Lett.* **2009**, *94*, 253303.

[221] R. Schueppel, R. Timmreck, N. Allinger, T. Mueller, M. Furno, C. Uhrich, K. Leo, M. Riede, *J. Appl. Phys.* **2010**, *107*, 044503.

[222] E. Voroshazi, B. Verreet, A. Buri, R. Muller, D. Di Nuzzo, P. Heremans, *Org. Electron.* **2011**.

[223] C. Sachse, L. Müller-Meskamp, L. Bormann, Y. H. Kim, F. Lehnert, A. Philipp, B. Beyer, K. Leo, *Org. Electron.* **2013**, *14*, 143.

[224] J. van de Lagemaat, T. M. Barnes, G. Rumbles, S. E. Shaheen, T. J. Coutts, C. Weeks, I. Levitsky, J. Peltola, P. Glatkowski, *Appl. Phys. Lett.* **2006**, *88*, 233503.

[225] L. J. A. Koster, V. D. Mihailetchi, H. Xie, P. W. M. Blom, *Appl. Phys. Lett.* **2005**, *87*, 203502.

[226] V. D. Mihailetchi, H. Xie, B. de Boer, L. J. A. Koster, P. W. M. Blom, *Adv. Funct. Mater.* **2006**, *16*, 699.

[227] I. Riedel, J. Parisi, V. Dyakonov, L. Lutsen, D. Vanderzande, J. C. Hummelen, *Adv. Funct. Mater.* **2004**, *14*, 38.

Acknowledgements

his students in University of Texas at Dallas for cowork for CNT electrodes. I thank Dr. Dongchan Lim in KIMS for his great advice and cowork for corrugated OLEDs. I also thank all guys and alumni in my office, Sven Kunze, Paul Pahner, Merve Anderson, Dr. Rico Meerheim, and Carsten Wolf.

I am very thankful for Korean members in IAPP, Prof. Seunghyup Yoo in KAIST for his kind advice and guidance, Dr. Changhun Yun for his advice and huge effort for vapor jet PEDOT experiment, Prof. Jaehyun Lee in Hanbat Univ. for his advice and nice Korean food, and Dr. Jonghee Lee for his advice and introducing me OLEDs from basic to advanced research. I also thank Dr. Tae Hyun Gil in Fraunhofer COMEDD for his support and great Korean soup for my wife during pregnancy.

I would like to thank Dr. Won Mok Kim in KIST for his great guidance since when I started a research in 2007 and collaboration on ZnO work. I also thank my colleagues in KIST. I would like to thank Prof. Tae-Yeon Seong in Korea Univ. for great guidance and support. I thank my colleagues in Korea Univ.

I must thank my best high school friends, Bumsin, Raeroo, Jinhee, Wangsimni, Woomin, and Yongbum (in alphabetical order).

Last but not least, I want to thank my family for their constant encouragement. I want to thank my Grandma, my father, my mother, my brother, and my puppy Moong. I also thank my relatives. Finally, Bandi, my lovely little cute baby, will thank me. I would like to thank Seulki, my great love. This thesis is dedicated to her with my perpetual love. "You're the one who completes me"

Yong Hyun
Dresden Jan. 2013

Erklärung

Diese Dissertation wurde am Institut für Angewandte Physik/Photophysik der Fakultät Mathematik und Naturwissenschaften an der Technischen Universität Dresden unter wissenschaftlicher Betreuung von Prof. Dr. Karl Leo angefertigt.

Hiermit versichere ich, dass ich die vorliegende Arbeit ohne unzulässige Hilfe Dritter und ohne Benutzung anderer als der angegebenen Hilfsmittel angefertigt habe. Die aus fremden Quellen direkt oder indirekt übernommenen Gedanken sind als solche kenntlich gemacht. Die Arbeit wurde bisher weder im Inland noch im Ausland in gleicher oder ähnlicher Form einer anderen Prüfungsbehörde vorgelegt.

Yong Hyun Kim